Technische Universität München
Institut für Energietechnik

Lehrstuhl für Thermodynamik

Numerical Simulation of NO_2 Formation in Dual-Fuel Engines with Lean Premixed Methane-Air Charge

Ehsan Arabian

Vollständiger Abdruck der von der TUM School of Engineering and Design der Technischen Universität München zur Erlangung des akademischen Grades eines

DOKTORS der Ingenieurwissenschaften

genehmigten Dissertation.

Vorsitzender:

Prof. Dr.-Ing. Georg Wachtmeister

Prüfer der Dissertation:

1. Prof. Dr.-Ing. Thomas Sattelmayer
2. Prof. Dr. Friedrich Dinkelacker

Die Dissertation wurde am 16.06.2021 bei der Technischen Universität München eingereicht und durch die TUM School of Engineering and Design am 30.09.2021 angenommen.

Acknowledgment

This work has been conducted during my stay at the Thermodynamics Institute at the Technical University of Munich. The work was conducted in the framework of EU-project HERCULES-2 in close cooperation with MAN Energy Solutions.
I would like to thank my supervisor Prof. Dr.-Ing. Thomas Sattelmayer most gratefully for giving me the opportunity to work at his Institute and for all his supports during the different phases of last 6 years. My sincere gratitude to Prof. Dr. Dinkelacker from the Institute of Technical Combustion at the Leibniz Universität Hannover for reviewing my thesis. I am thankful to Prof. Dr.-Ing. Georg Wachtmeister for chairing the PhD examination.
My special thanks to Christian Kunkel and Marcus Becher from MAN Energy Solutions for the great collaboration and sharing their expertise with me.
I thank all the colleagues and staffs of the Thermodynamics Institute for their help and support. My special thanks to Helga Basset, for her helpfulness in diverse issues. My thanks also to Michael Schiffner for his great help during his stay at the Thermodynamics Institute. I would like to thank Noah Klarmann, Alireza Javareshkian and Payam Mohammadzadeh Keleshtery as colleagues and friends for their support. Further thanks to my friends Baback Sadeghi Aghdam, Arvin Izadpanah and Pedram Arabschahi, who supported me through the writing phase of the thesis.
At last but not least I am very thankful to my loving father, caring mother and supportive sister, who have accompanied me through different phases of my life, and have filled my heart with love. My very special thanks also to Mahmoud, who has guided me through the hard times and has encouraged me not to give up. I would like to devote this work to my beloved Aida, who stays forever in my heart.

Abstract

In this thesis, the mechanism of NO_2 formation in dual-fuel (DF) engines with lean premixed methane-air charge, ignited with small amounts of diesel, is studied numerically. The conditions under which NO_2 formation is augmented are discussed in detail by using the homogeneous reactor model. In the present work, a computationally efficient approach based on a priori constructed look-up tables is proposed for predicting the in-cylinder NO_2 formation in 3D computational fluid dynamics (CFD) calculations. This approach is also applied for predicting unburned CH_4 post-oxidation and the consequently CO formation and conversion.
A reliable prediction of the in-cylinder pollutant formation and conversion requires correct modeling of combustion. The so-called 3-Zones Extended Coherent Flame model (ECFM3Z) was used for modeling DF combustion in the CFD software AVL-Fire. Auto-ignition was predicted by using an a priori look up table that considered n-heptane (as diesel surrogate)-methane mixture ratios among other things. In addition, the effect of fuel mixture ratios on the laminar flame speed was taken into account in CFD calculations by the linear interpolation of the tabulated flame speeds of both species. The results of the combustion simulations were compared with the experimental results for two operation points. In-cylinder pollutant formation and conversion were evaluated directly at the engine exit in CFD. The closest measuring point in the exhaust duct was placed further downstream of the engine exit, so that the species evolutions in the exhaust duct were calculated by using homogeneous reactors and compared with the experiments. Another measuring point even further downstream allowed studying the effect of much higher residence times on NO_2 formation for a few other operation points. For predicting NO_2 formation three different kinetic mechanisms were employed in this thesis and compared with each other.

Kurzfassung

Im Rahmen dieser Arbeit wurde die NO_2 Bildung in Dual-Fuel (DF) Motoren mit magerem Methan-Luft Gemisch, gezündet mithilfe von Diesel Pilotstrahlen, numerisch untersucht. Die Bedingungen, unter denen eine hohe NO_2 Bildung auftritt, wurden mithilfe von Reaktor Berechnungen ermittelt. Ein effizientes, auf tabellierten Bildungsraten basiertes Model zur Vorhersage innermotorischer NO_2 Bildung in 3D CFD Rechnungen wurde vorgeschlagen. Dieses Konzept wurde zusätzlich zur Modellierung der Nachoxidation von unverbranntem Methan und CO Bildung in CFD Rechnungen angewandt. Eine zuverlässige Vorhersage von innermotorischen Schadstofferzeugung setzt eine akkurate Verbrennungsmodellierung voraus. Das sogenannte ECFM3Z Modell wurde zur Modellierung von DF Verbrennung in CFD Software AVL-Fire verwendet. Selbstzündung wurde anhand einer Lookup-Tabelle vorhergesagt, die unter anderem die Mischungsverhältnisse von n-Heptan (als Surrogat für Diesel)-Methan Gemisch, mitberücksichtigt. Außerdem, wurde der Einfluss des n-Heptan/Methan Mischungsverhältnisses auf die laminare Flammengeschwindigkeit durch lineare Interpolation von den jeweilig tabellierten Flammengeschwindigkeiten mitberücksichtigt. Die Resultate der Verbrennungssimulationen wurden mit den Experimenten für zwei Betriebspunkte verglichen. Die innermotorische Schadstofferzeugung für 2 Betriebspunkte wurde direkt am Motoraustritt mittels CFD evaluiert. Die erste Messstelle war weiter stromab im Abgaskanal des Versuchsmotors platziert, sodass die potentiellen Spezies Umwandlungen im Abgaskanal mithilfe homogenen Reaktoren modelliert und mit Experiment verglichen wurden. Eine zusätzliche Messstelle noch weiter stromab ermöglichte die Untersuchung der NO_2 Bildung für längere Aufenthaltszeiten. Drei verschiedene Reaktionsmechanismen wurden zur Vorhersage der NO_2 Bildung eingesetzt und deren Vorhersagen sind miteinander verglichen worden.

.

Contents

List of Figures

List of Tables

Nomenclature

Latin Letters

A_{corr}	[-]	Correction factor
b	[-]	Temperature exponent
c	[-]	Combustion progress variable
c_k	[$\mathrm{mol/m^3}$]	k-th species concentration
c_p	[$\mathrm{J/(kgK)}$]	Specific isobar heat capacity
c_v	[$\mathrm{J/(kgK)}$]	Specific isochoric heat capacity
C_{AI}	[-]	Auto-ignition correction factor
D	[$\mathrm{m^2/s^2}$]	Molecular diffusion coefficient
D	[$\mathrm{m^2/(m^3s)}$]	Flame surface annihilation
E_a	[J/mol]	Activation energy
f	[-]	Elliptic relaxation factor
FF	$[-]$	Fuel fraction
h	[J/kg]	Specific enthalpy
h_s	[J/kg]	Sensible enthalpy
h_{evap}	[$\mathrm{J/(m^3s)}$]	Evaporation heat loss
Δh_f^o	[J/kg]	Enthalpy of formation
H_u	[J/kg]	Lower heating value
k	[$\mathrm{m^2/s^2}$]	Turbulent kinetic energy
$k_{f,b}$	[$(\mathrm{molm^{-3}})^{1-\mathrm{n}}\mathrm{s^{-1}}$]	Forward/backward reaction rate coefficient
k_0	[same as $k_{f,b}$]	Arrhenius pre-exponential factor
K_{eq}	[-]	Equilibrium coefficient
L	[m]	Turbulence length scale
l_t	[m]	Integral length scale
l_η	[m]	Kolmogorov length scale
m	[kg]	Mass
M	[kg/kmol]	Molar mass
p	[Pa]	Pressure
P	[-]	Probability density function
P_k	[$\mathrm{kg/(ms^3)}$]	Source term for turbulent kinetic energy

PV	$[-]$	Progress variable
$\dot{q}$	$[\mathrm{J}/(\mathrm{m}^2\mathrm{s})]$	Heat flux
$\dot{q}_\Sigma$	$[\mathrm{J}/(\mathrm{m}^2\mathrm{s})]$	Flame power
R	$[\mathrm{J}/(\mathrm{molK})]$	Molar gas constant
s	$[-]$	Stoichiometric coefficient
S	$[1/\mathrm{s}]$	Magnitude of stain rate
s_L	$[\mathrm{m}/\mathrm{s}]$	Laminar flame speed
s_c	$[\mathrm{m}/\mathrm{s}]$	Fuel consumption speed
T	[K]	Temperature
T	[s]	Turbulence time scale
t	[s]	Time
U	[kgm/s]	Momentum
u	[J/kg]	Specific internal energy
$\underline{u}$	$[\mathrm{m}/\mathrm{s}]$	Velocity
$\overline{v^2}$	$[\mathrm{m}^2/\mathrm{s}^2]$	Mean square velocity fluctuation
V	$[\mathrm{m}^3]$	Volume
X	[-]	Mole fraction
Y	[-]	Mass fraction
Y_I	[-]	Ignition indicator scalar
x, y, z	[m]	Spatial coordinates

Greek Letters

β	[-]	Beta function
δ_{ij}	[-]	Kronecker-Delta
δ_Q	[m]	Quench distance
δ_L	[m]	Laminar flame thickness
δ_r	[m]	Reaction zone thickness
ϵ	$[\mathrm{m}^2/\mathrm{s}^3]$	Eddy dissipation rate
Γ_K	[-]	Efficiency factor
κ_m	$[1/\mathrm{s}]$	Mean flow induced flame stretch
κ_t	$[1/\mathrm{s}]$	Turbulence induced flame stretch
λ	$[\mathrm{W}/(\mathrm{mk})]$	Thermal conductivity
λ	[-]	Air-fuel equivalence ratio
μ	$[\mathrm{kg}/(\mathrm{ms})]$	Dynamic viscosity
μ_t	$[\mathrm{kg}/(\mathrm{ms})]$	Turbulent dynamic viscosity

ν	$[m^2/s]$	Kinematic viscosity
ν_t	$[m^2/s]$	Turbulent kinematic viscosity
$\nu_{k,i}$	[-]	Stoichiometric coefficient
$\dot{\omega}_{s,k}$	$[mol/(m^3s)]$	Net molar production rate of species k
$\dot{\omega}_{r,i}$	$[mol/(m^3s)]$	Net reaction rate of reaction step i
$\dot{\omega}_k$	$[kg/(m^3s)]$	Mass source term of species k
$\dot{\omega}_{Fu}$	$[kg/(m^3s)]$	Fuel consumption rate
$\dot{\omega}_T$	$[J/(m^3s)]$	Heat source term
$\dot{\omega}_I$	[1/s]	Source term of the ignition indicator
$\dot{\omega}_{PV}$	[1/s]	Conversion rate of the progress variable
$\dot{\omega}_{NO}$	$[kg/(m^3s)]$	Production rate of NO
ϕ	[-]	Fuel-air equivalence ratio
φ	[-]	Fuel mixture ratio
ρ	$[kg/m^3]$	Density
Σ	$[m^2/m^3]$	Flame surface density
$\overline{\sigma^2}$	$[K^2]$	Mean square temperature variance
τ_{ij}	$[N/m^2]$	Viscous stress tensor
τ_{AI}	[s]	Auto-ignition delay time
τ_{HT}	[s]	Main ignition delay time
τ_{LT}	[s]	Cold flame ignition delay time
τ_η	[s]	Kolmogorov time scale
τ_t	[s]	Integral time scale
τ_c	[s]	Chemical time scale
ζ	[-]	Velocity scale ratio

Dimensionless Numbers

Da	Damköhler number
Ka	Karlovitz number
Pr	Prandtl number
Pr_t	Turbulent Prandtl number
Re_t	Turbulent Reynolds number
Sc	Schmidt number
Sc_t	Turbulent Schmidt number
φ_Q	Dimensionless wall heat flux

Subscripts/Superscripts

A	Zone containing methane-air
ad	Adiabatic
b	Burned
CH_4	Methane
C_7H_{16}	N-heptane
CO	Carbon monoxide
CO_2	Carbon dioxide
CH_2O	Formaldehyde
CO_{pro}	Production of carbon dioxide
CO_{cons}	Consumption of carbon dioxide
F	Flame
F	Zone containing n-heptane
Fu	Fuel
H_2O	Water
i, j	Indices
in	Inlet
ini	Initial
M	Mixed zone
max	Maximum
min	Minimum
N_2	Nitrogen
NO	nitrogen monoxide
NO_2	nitrogen dioxide
$NO2 \rightarrow NO$	nitrogen dioxide conversion to nitrogen monoxide
$NO \rightarrow NO2$	nitrogen monoxide conversion to nitrogen dioxide
O_2	Oxygen
OH	Hydroxyl radical
Q	Quenched
T	Tracer
TFu	Tracer fuel
TNO	Tracer nitrogen monoxide
$TO2$	Tracer oxygen
u	Unburned
w	Wall

Mathematical Operators

$\overline{\square}$	Reynolds-average
$\widetilde{\square}$	Favre-average
$\square'$	Reynolds-fluctuating term
$\square''$	Favre-fluctuating term
$\dot{\square}$	Time derivative
$\langle\rangle_s$	Surface averaging
$\square\|_{\square}$	Conditional averaging
∇	Gradient
Δ	Difference

Acronyms

CA	Crank Angle
CFD	Computational Fluid Dynamics
CN	Cetane-Number
DF	Dual-Fuel
DNS	Direct Numerical Simulation
EBU	Eddy Break-Up
ECA	Emission Control Area
ECFM	Extended Coherent Flame Model
ECFM3Z	3-zones Extended Coherent Flame Model
EEDI	Energy Efficiency Design Index
EGR	Exhaust Gas Recirculation
FGM	Flamelet Generated Manifold
FPI	Flame Prolongation of ILDM
FL	Full Load
FTIR	Fourier-Transform Infrared Spectroscopy
FBN	Fuel-Bond Nitrogen
GRI	Gas Research Institute
GHG	Green House Gases
HCCI	Homogeneous Charge Compression Ignition
HP	High Pressure
IMO	International Maritime Organization
ILDM	Intrinsic Low-Dimensional Manifolds

ITNFS	Intermittent Turbulence Net Flame Stretch
LES	Large Eddy Simulation
LP	Low Pressure
MEP	Mean Effective Pressure
NASA	National Aeronautics and Space Adminstration
NG	Natural Gas
P	Product
PDF	Probability Density Function
PL	Partial Load
RCEM	Rapid Compression Expansion Machine
ROHR	Rate of Heat Release
RPM	Rounds Per Minute
SCR	Selective Catalytic Reduction
SOI	Start of Ignition
URANS	Unsteady Reynolds-Averaged Navier-Stokes
WSR	Well Stirred Reactor

1 Introduction

In order to limit pollutant emissions such as nitrogen oxides (NO_x) and sulfur oxides (SO_x) caused by marine engines, regulations specified by the International Maritime Organization (IMO) under MARPOL Annex VI, known as the Tier I regulations [1], entered into force in 2005. These regulations became much stricter when Tier II and Tier III entered into force in 2011 and 2016, respectively; the Tier III regulations applied to the so-called emission control areas (ECAs). Figure 1.1 shows the NO_x regulations depending on the maximum engine speed as well as the limitations on the sulfur content of the fuel as measure to control the SO_x emissions. In addition, the IMO introduced the Energy Efficiency Design Index (EEDI) for CO_2 emissions in 2013 to tackle the climate change problem, with a target of reducing CO_2 emissions by up to 70% by 2050 compared with 2008 levels.

The common technologies for fulfilling the required pollutant regulations in the conventional marine diesel engines include the installation of selective catalytic reduction (SCR), which is installed to reduce NO_x; a

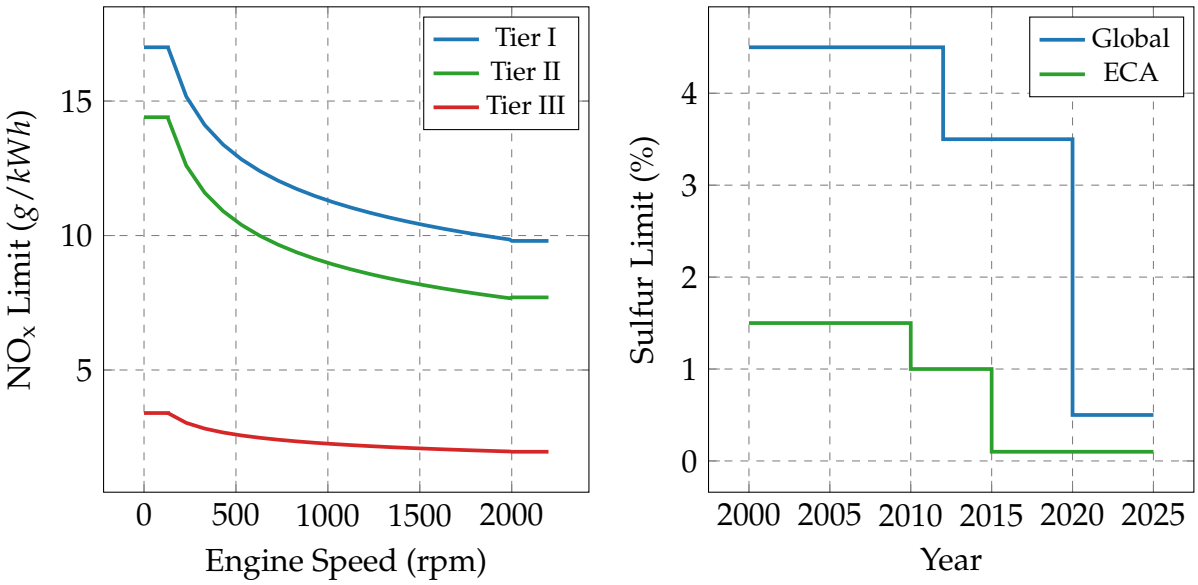

Figure 1.1: MARPOL Annex IV NO_x and SO_x Emission Limits

scrubber, which is installed to remove SO_x by see water washing from exhaust gas; and exhaust gas recirculation (EGR) and emulsion, which are used to reduce the combustion temperature. All of these common technologies introduce disadvantages in terms of system complexity, environmental side effects and cost.

The lean natural gas (NG)-diesel dual-fuel (DF) engine can be a promising technology for fulfilling pollutant regulations. This configuration consists of the port injection of NG to form a combustible air-NG mixture in the cylinder. Due to the high auto-ignition temperature of methane (the main component of NG), the mixture is ignited by the direct injection of a small amount of diesel. The lean NG-diesel DF engine exhibits the following advantages compared with conventional diesel engines: A small amount of diesel leads to less soot formation; the lower ratio of C/H atoms of CH_4 causes lower CO_2 emissions; and NO emissions are suppressed due to the lower peak temperature following lean combustion. However, one drawback of this combustion method is the methane slip from the crevices and due to quenching effects close to the cylinder walls [2,3]. Various experimental studies using plug flow reactors have proved augmented conversion of NO to NO_2 in the presence of small amounts of CH_4 when excess air is present [4,5].

NO_2 has a higher toxicity and different formation mechanism compared with NO. It is the precursor substance relevant to the formation of ground level ozone (O_3) and the cause of smog formation. Furthermore, mixing of NO_2 with moisture causes the formation of nitrous acids (HNO_2) or directly nitric acids (HNO_3), which is known as acid rain. The negative effects of NO_2 on human health are acute symptoms and lung function impairment [6,7]. Kerr et al. [8] indicated that exposure to 0.5 ppm NO_2 for 6 hours could result in significant reduction of in people's pulmonary function.

Rößler et. al. have studied the NO_2 emissions from a single cylinder diesel test engine experimentally [9,10]. In their study, it was evident that in the whole engine operations window, meaning different engine load and engine speed and without EGR, the level of NO_2 to NO_x (as the summation of NO and NO_2) remained less than 4%. Through the parameter variations performed at an engine load of 25 % and an engine speed of 1400 RPM, they demonstrated that earlier start of injection, higher injection pressure or lower EGR leads to higher NO as well as NO_2 emissions.

However the increase in NO_2 emissions was much more gradual compared with the NO rise, and thus, the ratio of NO_2 to NO_x fell. The highest NO_2 to NO_x ratio was recorded for the conditions leading to the lowest produced NO (for instance, by higher EGR), as the level of NO was low and most of produced NO converted to NO_2. They showed that, among different parameter variations, increasing the air-fuel equivalence ratio λ (higher O_2 concentration) had the greatest effect on increasing in-cylinder NO_2 formation.

The direct influence of λ on NO_2 emissions from Diesel engines was also reported by Hilliard et. al. [11], who measured a NO_2 to NO_x ratio of approximately 30% under very lean conditions (λ=4.55) and a low engine speed of 1000 RPM. The increasing NO_2 formation under lean conditions might, according to the authors, be due to the in-flame NO_2 production, that escapes from the flame into cooler areas such as in quench zones, which are widespread in diesel engines operated under lean conditions.

In gas engines, a significant NO_2 to NO_x ratio was recorded by Olsen et. al. [12], when the engine was operated under ultra-lean conditions. Thus, both NO and NO_2 concentrations were reduced with increasing λ, and the NO concentration fell faster than NO_2, leading to a higher NO_2 to NO_x ratio.

The experimental study of Lieu et. al [13] investigated NO_2 emissions from heavy duty diesel engines operated in DF H_2-diesel mode. Their investigation revealed higher NO_2 emissions, namely three (at 70% load) to five (at 10% load) times those of the diesel operation mode.

From the aforementioned experimental investigations, it is evident that the NO_2 formation is actually driven by the conversion of NO. This conversion is augmented under certain thermodynamic conditions and mixture compositions, which are discussed in detail later in this thesis. The governing reaction paths of NO-NO_2 conversion have been the subject of several experimental and numerical studies. The performance of the few available kinetic mechanisms is also discussed in this thesis.

1.1 Objectives

The objective of this study was to model the in-cylinder NO_2 formation in a one-cylinder lean NG-diesel test engine of MAN, followed by the fur-

ther NO_2 formation in its exhaust duct numerically. The model localizes the in-cylinder NO_2 formation and the extent of NO_2 produced during combustion in the engine and in the exhaust duct of a test engine.

To the author's knowledge, no simplified model exists for capturing in-cylinder NO_2 formation. Prior numerical investigations utilized detailed kinetic mechanisms in computational fluid dynamics (CFD) to capture combustion and NO_2 formation in a DF engine [14]. In this study, a low-order model for predicting NO_2 formation/conversion as well as CH_4 post-oxidation and CO formation/conversion, based on look-up tables, was developed.

To accurately predict NO_2 formation, correct combustion modeling and a correct prediction of the unburned CH_4 from crevices and caused by flame-wall quenching were necessary. The 3-Zones Extended Coherent Flame (ECFM3Z) combustion model was used in the simulation package AVL-Fire, for which auto-ignition delay times and laminar flame speeds were modeled based on the a priori generated look-up tables.

1.2 Outline of the thesis

The remainder of this thesis is organized as follows. Chapter 2 presents the fundamental investigation of NO_2 formation in reactive flow by using batch as well as well-stirred reactors in Cantera, employing different kinetic mechanisms. The aim of this investigation was to find out under which engine-related stage (ignition, combustion or post-oxidation) and mixture composition the NO_2 formation was augmented. The findings in this chapter have used to efficiently model the NO_2 formation and conversion in CFD calculations.

Chapter 3 describes the 3D CFD modeling of turbulent combustion. The employed ECFM3Z combustion model as well as auto-ignition and laminar flame speeds modeling in the context of DF combustion are described. The simulations were carried out in AVL-Fire. The results of the combustion simulations were compared with the experimental results. Precise capturing of combustion was necessary for correctly predicting of in-cylinder pollutant formation and conversion.

Chapter 4 concerns the modeling of the pollutant formation and conversion, which includes the modeling of NO, unburned CH_4, CO and

NO_2 species mass fractions. For predicting the unburned CH_4 a quenching model based on the quenching distance was implemented in AVL Fire with the crevice regions also taken into account.

For predicting the post-oxidation of modeled unburned CH_4, the CO formation/conversion, and particularly the NO_2 formation/conversion in the engine, a method based on look-up tables is then proposed. In this approach, the conversion rates of the so-called progress variables, corresponding to the CH_4, NO_2 and CO, mass fractions were computed through 0D homogeneous reactor simulations by employing different kinetic mechanisms in Cantera and stored in look-up tables. During the CFD calculations, the conversion rates were retrieved from the look-up tables for each computational cell. The advantage of this approach is that it avoids the time-consuming detailed kinetics calculation in CFD. The implementation was performed in the CFD simulation tool AVL-Fire by introducing transport equations with the source terms interpolated from the look-up tables entries.

In Chapter 5, pollutant formation and conversion in the engine as well as in the exhaust duct are presented. The latter ones are compared with experimental results. Finally, the findings are summarized in Chapter 6.

2 Prestudy of NO_2 Formation

This chapter aims to provide insights regarding the mechanism of NO_2 formation in homogeneous reactive mixtures. The findings presented in this chapter served as the basis for CFD modeling of NO_2 formation in the investigated (DF) engine. The first section includes the theoretical background of modeling zero-dimensional reactive mixtures. The second section concerns the prestudy of NO_2 formation under the conditions expected in DF engines by batch as well as well-stirred reactors. Thereby, the effect of mixture temperature, pressure and compositions on NO_2 were studied, in order to determine the variables that affect NO_2 formation for CFD modeling later on.

2.1 Theory and Modeling of Reactive Chemical Systems

The chemical equilibrium of a reactive mixture is a state of a gas, for which the Gibbs energy level has reached its minimum. On the basis of chemical equilibrium it is possible to describe the final state of a gas phase regarding its temperature, concentrations, etc. depending on the initial state of the gas phase. The chemical equilibrium does not describe the time evolution until the final state is reached. This implies that the finite residence time of the gas in real applications is not taken into account. By contrast, the reaction mechanism models the species evolution over time by employing several coupled elementary reactions. The open source software Cantera [15] has been used to model the state of the reactive mixture by employing different reaction mechanisms. A batch reactor is an appropriate model for investigating the non-steady state of a closed reactive system over time with uniform composition and temperature. A set of ordinary differential equations for the species and temperature changes are solved. The temporal change of the k-th species is calculated using

$$\frac{dY_k}{dt} = \frac{M_k \dot{\omega}_{s,k}}{\rho} \tag{2.1}$$

where M_k and ρ are the molar mass of the k-th species and gas mixture density, respectively. $\dot{\omega}_{s,k}$ corresponds to the net production rate of the k-th species:

$$\dot{\omega}_{s,k} = \sum_i \nu_{k,i} \dot{\omega}_{r,i} \tag{2.2}$$

where $\dot{\omega}_{r,i}$ is the net progress rate of the i-th reaction step and $\nu_{k,i}$ as the stoichiometric coefficient of the k-th species in the i-th reaction step of the reaction mechanism consisting of several reaction steps. Considering the i-th reversible elementary reaction step in a complex mechanism:

$$\nu_A \mathrm{A} + \nu_B \mathrm{B} \underset{k_b}{\overset{k_f}{\rightleftharpoons}} \nu_C \mathrm{C} + \nu_D \mathrm{D}, \tag{2.3}$$

the net progress rate $\dot{\omega}_{r,i}$ can be expressed in terms of the law of mass action as follows:

$$\dot{\omega}_{r,i} = k_f [c_A]^{\nu_A} [c_B]^{\nu_B} - k_b [c_C]^{\nu_C} [c_D]^{\nu_D}. \tag{2.4}$$

k_f and k_b are the forward/reversed reaction rate coefficients, respectively, and c_k denotes the concentration of the k-th species. The forward reaction rate coefficient k_f is calculated using the Arrhenius equation:

$$k_f(T) = k_0 T^b \exp(\frac{-E_a}{RT}), \tag{2.5}$$

where E_a is the activation energy, k_0 is the pre-exponential factor, b is the temperature exponent, T is temperature and R ≈ 8.314 $[j/(molK)]$ is the molar gas constant. The backward reaction rate coefficient can be related to the equilibrium constant K_{eq} as follows:

$$k_b = \frac{K_{eq}}{k_f}, \tag{2.6}$$

for which the equilibrium constant K_{eq} depends on the thermodynamic properties of the species determined through the NASA polynomials. The temporal change of temperature due to reaction under isochoric conditions can be written as:

$$\rho c_v \frac{dT}{dt} = -\sum_k \dot{\omega}_{s,k} u_k \tag{2.7}$$

where c_v is the specific isochoric heat capacity and u_k is the partial specific internal energy of species k, which can be related to the partial specific enthalpy h_k through

$$u_k(T) = h_k(T) - \frac{RT}{M_k}. \tag{2.8}$$

In contrast to the batch reactor, the well-stirred reactor is an open system that enables mass exchange. The model is based on the assumption of a uniform composition and very fast mixing of the reactants and products. Considering an inlet mass flow of $\dot{m}_{in}$ with mixture compositions $Y_{k,in}$, the species conversion equation can be written as follows:

$$\frac{dY_k}{dt} = \frac{\dot{m}_{in}}{m}(Y_{k,in} - Y_k) + \dot{\omega}_{s,k} \tag{2.9}$$

and the energy equation is as follows:

$$c_v \frac{dT}{dt} = \frac{\dot{m}_{in}}{m}(h_{in} - \sum_k u_k Y_{k,in}) - \sum_k \dot{\omega}_{s,k} u_k \tag{2.10}$$

The left-hand side of equations 2.9 and 2.10 tend toward zero as the steady state is approached. In the following section both the batch reactor and well-stirred reactor model are used for developing an understanding of the mechanism of NO_2 formation.

2.2 Investigation of the NO_2 Formation Mechanism Using the Homogeneous Reactor

In this section the NO_2 formation during the different stages of ignition, combustion and post-oxidation of methane-air charge is investigated via homogeneous reactors. The aim of this investigation is to understand under which engine-related conditions, or rather at which time or stage the NO_2 formation is augmented by employing different reaction mechanisms. Methane is taken as the substitute for NG. In the scope of this work, only the effect of CH_4 on NO_2 formation was taken into account. The potential effect of the low amounts of C_2-C_3 hydrocarbons present in NG as well as diesel pilot, as the ignition source in DF engine, on the NO_2 formation was neglected.

In literature there are a few reaction mechanisms which have been validated under different conditions to predict the C_1-C_2 hydrocarbons oxidation as well as NO and NO_2 formation.

Rasmussen et. al. [16–18] proposed a reaction mechanism for the effect of NO and NO_2 on C_1-C_2 hydrocarbons oxidation. The mechanism comprises chemistry submechanisms for H_2/O_2, CO/CO_2, NO/NO_2 and C_1-C_2 hydrocarbons and their interactions. The reaction mechanism has been validated for high pressures ranging from 20 to 100 bar, medium temperatures ranging form 600 K to 900 K and fuel air equivalence ratios ϕ ranging from 100 (very rich) to 0.045 (very lean) in methane-air mixtures. These sets of reactions are partly adapted from the previous investigations of Glarborg et. al. [19], modeling NO reduction by C_1 and C_2 hydrocarbons and validated for the temperature range of 800 K-1500 K at atmospheric pressure.

In another work, Sivaramakrishnan et. al [20] introduced a mechanism for the oxidation of a NG blend (CH_4-C_2H_6) and the interaction of the hydrocarbons with NO and NO_2, consisting of 130 chemical species and 818 reversible elementary reactions. The rate coefficients were validated against high pressure/temperature conditions . The Gri 3.0 [21] mechanism, consisting of 325 reactions and 53 species is the widespread reaction mechanism used for calculating the ignition and combustion of NG. This mechanism also includes paths for NO andNO_2 formation.

This section presents an investigation of the performance of the reaction mechanisms of Rasmussen, Sivaramakrishnan and Gri 3.0 in predicting the NO_2 formation has been studied. First, the steady state of methane-air combustion with the initial fuel-air equivalence ratio ϕ=1 under an engine relevant initial conditions of T_{ini}=700K and p_{ini}=50 bar and for different mixture residence times was calculated using the well-stirred reactor (WSR) model in Cantera. The WSR model exhibits the feature of infinite fast mixing of reactants and products and it models the steady state of the reactive system. The induction time of the radical formation during the ignition is not taken into account; for this purpose, batch reactor model were employed, as described later in this section. In Figure 2.1, the final temperature, and CH_4, NO, and NO_2 mass fractions are plotted for a range of mixture residence times employing different reaction mechanisms. Combustion occurs as the minimum residence time is exceeded, resulting in CH_4 oxidation and temperature rise. The NO mass

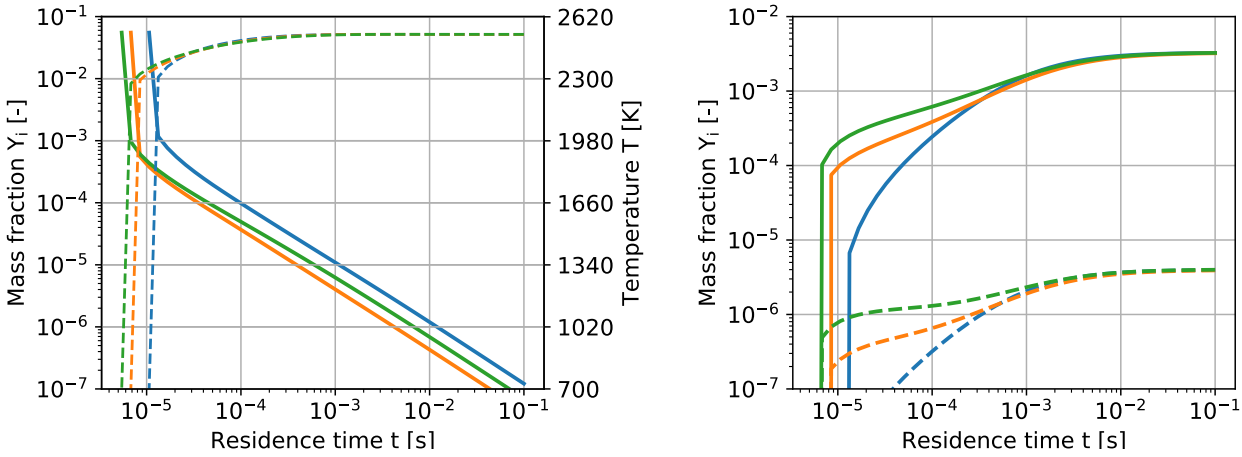

Figure 2.1: Prediction of Rasmussen (——), Sivaramakrishnan (——) and Gri 3.0 (——) of: Y_{CH4} (——) and temperature (- - - - -) (left) and Y_{NO} (——) and Y_{NO2} (- - - - -) (right) during different residence times; T_{ini}=700K, p_{ini}=50 bar, ϕ=1

fraction increases as the burned gas remains at a high temperature over a longer residence time (thermal NO formation predicted by Zeldovic [22]). The NO_2 mass fraction rises as well; however it remains three orders of magnitude lower than that of NO. It can be concluded that the amount of NO_2 in the hot flue gas following the combustion remains very low. All the mechanisms capture the same tendency.

The following calculations were conducted by using the homogeneous batch reactor model and by employing different reaction mechanisms. The produced hot flue gas containing NO might be mixed locally with the unburned fresh methane-air mixture. In Figure 2.2, the composition and temperature evolution over time are plotted for a mixture of a low amount of NO in the fresh methane-air mixture of ϕ=0.5 at T_{ini}=1200 K and p_{ini}=60 bar. It can be seen that following an induction time that differs by each reaction mechanism, combustion occurs, leading to temperature rise and consumption of CH_4. During the induction time and the radical formation NO_2 concentration rises, accompanied by NO consumption. This implies that the NO_2 formation is coupled with partial CH_4 oxidation. As the temperature rises, the produced NO_2 converts back to NO quickly, as predicted by all three reaction mechanisms. It can be concluded that NO_2 formation is augmented in NO-methane-air mixture during the induction time. However as combustion occurs and the temperature rises the NO_2

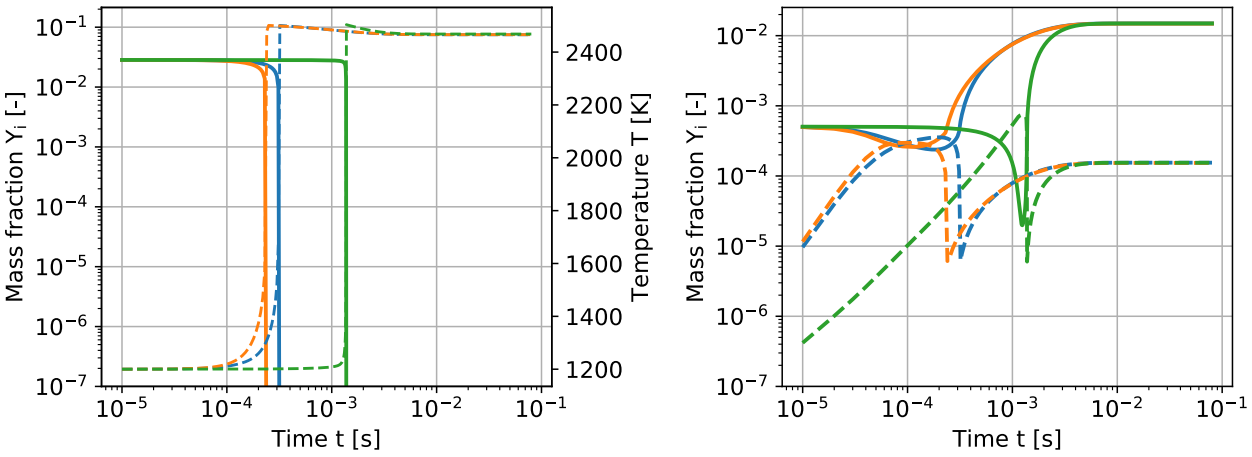

Figure 2.2: Prediction of Rasmussen (——), Sivaramakrishnan (——) and Gri 3.0 (——) of: Y_{CH_4} (——) and temperature (- - - - -) evolution (left); Y_{NO} (——) and Y_{NO_2} (- - - - -) (right) ; Initial conditions: Mixing of NO with Y_{NO}=0.0005 in fresh methane-air mixture ϕ=0.5, T=1200 K, p=60 bar

produced during the induction time converts back to NO, implying that NO_2 is not problematic at high temperatures. The strong temperature rise due to CH_4 oxidation can be avoided by using very lean mixtures of CH_4-air. In Figure 2.3 the species evolution in a mixture with low amounts of CH_4 and NO in air at low temperature and pressure levels as expected during the expansion stroke in the engine can be seen. It can be seen that the temperature rise is low, and as a result, the produced NO_2 remains at a high level over a long residence time, followed by NO and NO_2 evolution towards their equilibrium state by longer residence times. It can be concluded that the high level of NO_2 is the result of low amounts of CH_4 mixing with NO in the presence of O_2 as an oxidizer at low temperature levels. As can be seen in Figure 2.4, the NO_2 formation is frozen in the absence of NO or O_2. For the mixture of O_2 and NO in the absence of CH_4, the level of NO_2 remains low, compared with the NO concentration as shown in Figure 2.4.

Based on the aforementioned simulations, the strong susceptibility of NO_2 formation in DF engines with a lean methane-air mixture can be explained as follows: The NO formation is the strongest in the zones with the highest equivalence ratio, namely in the zone of diesel spray combustion. The temperature in this zone is the highest, and thus, the formation of thermal NO over time is enhanced [22, 23]. Figures 2.1 and 2.2 indicate

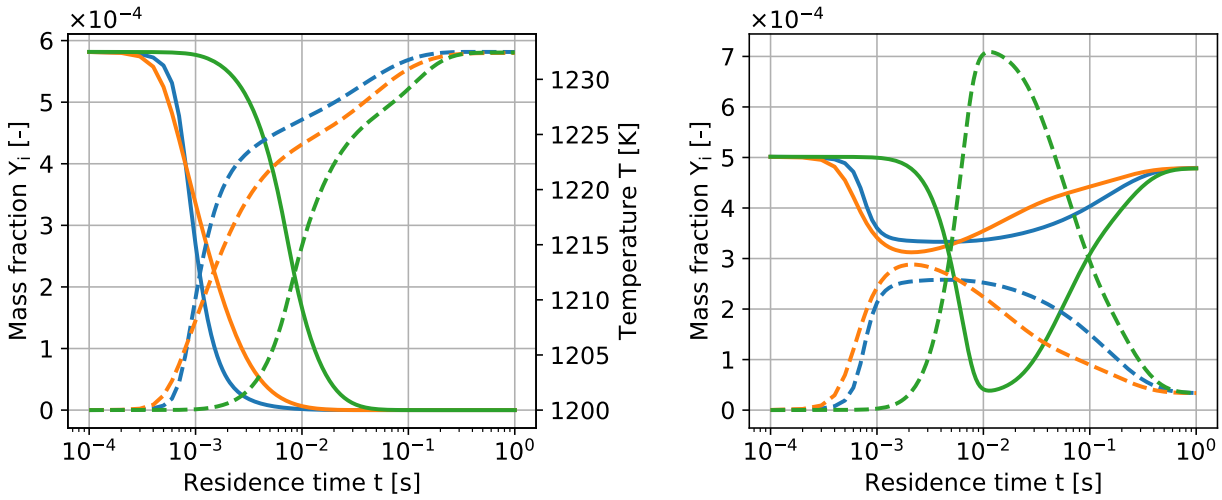

Figure 2.3: Prediction of Rasmussen (——), Sivaramakrishnan (——) and Gri 3.0 (——) of: Y_{CH_4} (——) and T (- - - - -) evolution (left) ; Y_{NO} (——) and Y_{NO_2} (- - - - -) evolution (right); Initial conditions: ϕ=0.01 (Y_{CH_4}=0.00058, Y_{O_2}=0.23,Y_{N_2}=0.766), Y_{NO}=0.0005, T=1200 K, p=10 bar

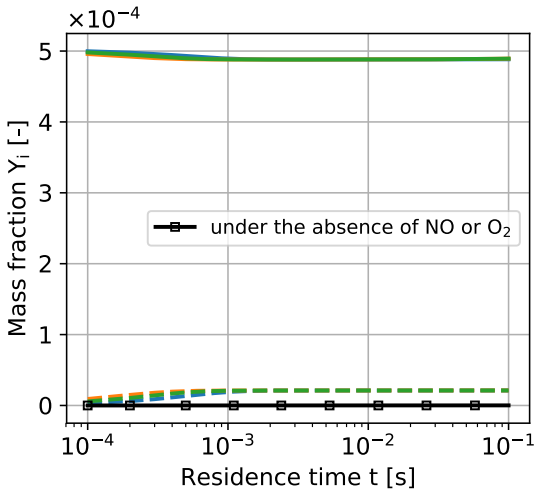

Figure 2.4: Prediction of Rasmussen (——), Sivaramakrishnan (——) and Gri 3.0 (——) for Y_{NO} (——) and Y_{NO_2} (- - - - -) evolution under the absence of CH_4 (in NO-O_2-N_2 mixture); And prediction of all the mechanisms for Y_{NO_2} under the absence of NO or O_2 (⊓⊔) at T=1200 K and p=10 bar

that the NO_2 concentration related to this state of combustion is very low. High levels of NO_2 are reached when unburned CH_4, which has survived bulk combustion, is mixed and diluted with the product gas following combustion containing NO and post-oxidized in the presence of O_2 at

low temperatures. O_2 always present in the flue gas from lean methane-air combustion.

The NO_2 formation rate varies depending on the mixture temperature. This is depicted in Figure 2.5 for low amounts of CH_4 (Y_{CH_4}=0.00058) and NO (Y_{NO}=0.0005) in the flue gas, which represents the main gas products following the lean methane-air combustion with ϕ=0.5 (Y_{O_2} =0.1127, Y_{N_2} =0.745, Y_{CO_2} =0.0778, Y_{H_2O} =0.0636). NO_x as a summation of NO and NO_2 remains constant. For high temperatures and higher reactivity of CH_4,

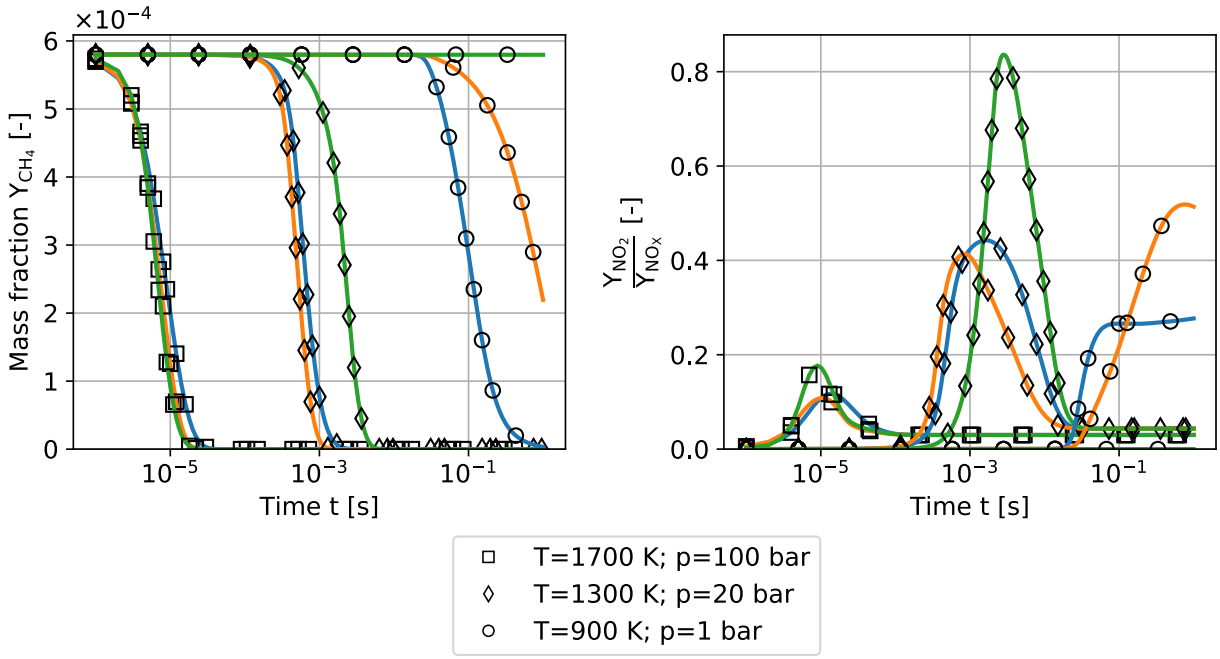

Figure 2.5: Prediction of Rasmussen (——), Sivaramakrishnan (——) and Gri 3.0 mechanisms (——) for Y_{CH_4} and Y_{NO_2} for different initial temperatures/pressures. Initial conditions: Y_{CH_4}=0.00058,Y_{O_2}=0.1127,Y_{N_2}=0.745,Y_{CO_2}=0.0778,Y_{H_2O}=0.0636, Y_{NO}=0.0005

NO_2 formation is faster, whereas at lower temperatures the formation rates are lower. The high mixing temperature, however, results in fast conversion of NO_2 back to NO during low residence times as seen by T=1700 K. At lower temperatures NO_2 still remains high for a longer residence time as depicted for T=1300 K. At very low temperature level (T=900 K) the oxidation of CH_4 and thus NO_2 formation are shifted to much later times. Gri 3.0 even predicts no reactivity at this low temperature. Thus the mixing temperature together with the mixture residence time plays a key roll in the final amount of NO_2. The different performance of the re-

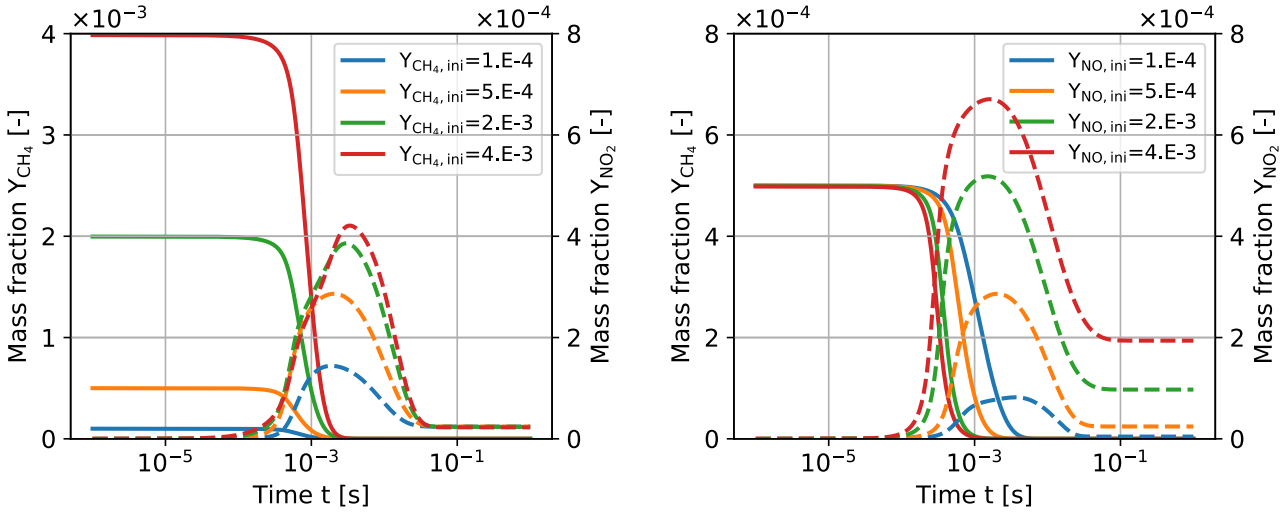

Figure 2.6: Effect of varying CH_4 (left) and varying NO initial mass fractions (right) on Y_{CH_4} (——) and Y_{NO_2} (- - - - -) evolution predicted by Rasmussen reaction mechanism; Initial conditions: $Y_{NO,ini}$=5.E-4 (left), $Y_{CH_4,ini}$=5.E-4 (right) and main products following combustion of methane-air ϕ=0.5; T=1300 K, p=20 bar

action mechanisms, as depicted in Figure 2.5, is the reason why the three mechanisms are taken into account for the CFD calculations later on.

As for temperature/pressure, the mixture composition also affects the extent of NO_2 formation. During the expansion stage, the CH_4 that survived combustion is mixed and diluted in the flue gas containing O_2 and NO. Figure 2.6 shows the effect of varying CH_4 initial mass fractions (with a constant NO initial mass fraction) and varying NO initial mass fractions (with constant CH_4 initial mass fraction) on NO_2 formation rate predicted using the Rasmussen mechanism. Higher initial CH_4 mass fractions lead to a higher oxidation rate of CH_4 and thus to a higher NO_2 formation rate. Depending on the available NO amount however, the NO_2 is limited despite the increasing CH_4, which can be expected due to the direct conversion of NO to NO_2. On the other hand, a higher NO mass fraction leads to faster CH_4 oxidation and thus faster NO_2 formation and higher NO_2 level, as depicted in the right part of Figure 2.6. Besides the main products, the flue gas from combustion also contains radicals that could affect the NO_2 formation. The radicals' mass fractions in an equilibrium state for an initial mixture of CH_4-air with ϕ=0.5, an initial temperature of 700 K, and an initial pressure of 50 bar are as follows: Y_{OH}=0.00013, Y_O=3.6E-6, Y_H=2.E-9 and Y_{HO_2}= 2.03E-6. It can be seen that the OH mass

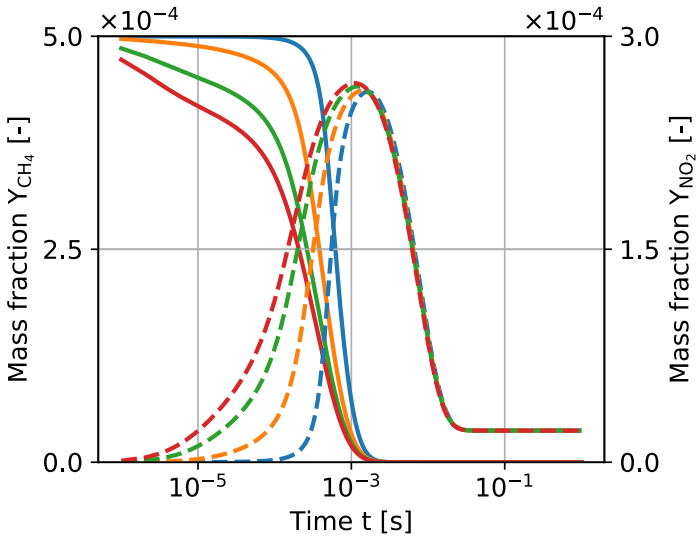

Figure 2.7: Effect of OH radicals on Y_{CH_4} (——) and Y_{NO_2} (- - - - -) predicted by Rasmussen reaction mechanism; Initial conditions: Y_{OH}=0.0 (——), Y_{OH}=10.e-6 (——), Y_{OH}=50.e-6 (——) and Y_{OH}=100.e-6 (——),Y_{CH_4}=0.0005, Y_{NO}=0.0005, main products following combustion of methane-air ϕ=0.5, T=1300 K, p=20 bar

fraction is higher than the mass fraction of the O radical by two orders of magnitude, and the mass fractions of HO_2 and H radicals are negligible. Hence, the effect of OH radicals on NO_2 formation is taken into account. As depicted in Figure 2.7, even a small amount of OH radicals accelerates the CH_4 reactivity, and thus its oxidation. As a result NO to NO_2 conversion is faster.

According to previous investigations the mechanism of NO_2 formation was determined. The dimensions that affect the NO_2 formation rate were also discussed. For further modeling of NO_2 formation in CFD, which is discussed in Section 4.3, it was necessary to consider the mixture temperature, pressure and CH_4, NO, and OH mass fractions. Since the present study was aimed at NO_2 prediction in a DF engine with a lean premixed methane-air charge of $\phi \approx 0.5$, the O_2 mass fraction in the flue gas was set constant to Y_{O_2}=0.1127 for modeling purposes in CFD. Slightly lower or higher values of Y_{O_2} would not affect the NO_2 formation that much due to different orders of magnitude of the CH_4 and O_2 mass fractions.

3 CFD Modeling of DF Engine Combustion

The investigated DF engine in this thesis is a so-called diesel-ignited NG engine, also referred to as a diesel-gas engine [24]. Port injected NG and air enter the combustion chamber during the open inlet valves and form a lean premixed NG-air charge in the cylinder. During the compression phase, a small amount of diesel pilot is injected into the chamber. This leads to the formation of a mixture of diesel-NG-air and the onset of ignition. Following the ignition the flame front propagates in the premixed background mixture.

A few challenges exist in the numerical simulations of such DF engines. The first step is a cold flow simulation during charging through the intake manifolds. This is a prerequisite for accurately predicting the mixture fraction of NG and air as well as the flow field and the turbulence field in the chamber [25]. The next step is modeling the diesel injection to capture its penetration length and its mixing with the background mixture. Accurate spray modeling is important for determining the ignition location(s) [26, 27]. An appropriate kinetic mechanism of a diesel-NG mixture also plays a key roll in predicting ignition [28–30] and depicts another challenge for modeling DF engines.

The 3D CFD calculation in the framework of unsteady Reynolds-averaged Navier-Stokes (URANS) equations was used in the present study. The simulation was conducted using the CFD software package AVL-FIRE (version 2018.2). The charge exchange during the open inlet valves was not simulated, and thus, the initial turbulence field in engine was assumed to be homogeneous. In addition, the validation of the spray model was not in the scope of this work. The spray modeling and the corresponding model parameters are based on validation cases conducted by MAN.

In Sections 3.1 and 3.2 the theoretical background for modeling the reactive turbulent flow is described. Sections 3.3 and 3.4 concern the physical analysis and numerical approaches for modeling the turbulent pre-

mixed combustion that is expected to be the relevant combustion regime for the investigated DF engine. For modeling turbulent combustion, the ECFM3Z model was employed, which can model auto-ignition, diffusion combustion and premixed flame propagation. The ECFM3Z combustion model is described in Section 3.5. Since the ECFM3Z model was originally developed for modeling diesel combustion, it was necessary to adapt its sub-models for predicting auto-ignition and laminar flame speeds for modeling DF combustion. The adapted auto-ignition model, described in Section 3.6, had already been implemented in AVL-Fire in previous work conducted at the Thermodynamics Institute and was used in the present work. The adaption with respect to the modeling of laminar flame speeds was implemented in the present work and is described in Section 3.7. Two operation points were calculated. In section 3.8 the simulations setups are described, followed by the results of combustion simulations, presented in Section 3.9.

3.1 Theoretical Background of Modeling 3D Reactive Flows

To quantify the in-cylinder spatial distribution and temporal evolution of quantities such as temperature and mass fractions, 3D CFD is used, which solves a set of coupled non-linear partial differential equations. The temporal and spatial change of ρ, U, h_s, and Y_k, meaning the density, momentum, sensible enthalpy and species mass fractions in their differential form, respectively, are as follows [31]:

- Mass:

$$\frac{\partial \rho}{\partial t} + \frac{\partial}{\partial x_i}\left(\rho u_i\right) = 0 \tag{3.1}$$

where ρ is the density and u is the velocity.

- Momentum:

$$\frac{\partial \rho u_j}{\partial t} + \frac{\partial}{\partial x_i}\left(\rho u_i u_j\right) = -\frac{\partial p}{\partial x_j} + F_i + \frac{\partial \tau_{ij}}{\partial x_i} \tag{3.2}$$

where u_i and u_j denote the velocities in the i and j directions, respectively. The first and the second terms in equation 3.2 represent the surface and the volume force on the fluid respectively. The change rate of momentum

due to the viscous stresses (third term) is considered by the viscous tensor known as the momentum flux τ_{ij}:

$$\tau_{ij} = -\frac{2}{3}\mu\frac{\partial u_k}{\partial x_k}\delta_{ij} + \mu\left(\frac{\partial u_i}{\partial x_j} + \frac{\partial u_j}{\partial x_i}\right) \tag{3.3}$$

with μ as the dynamic viscosity and δ_{ij} as the Kronecker delta function.

- Sensible enthalpy:

$$\frac{\partial \rho h_s}{\partial t} + \frac{\partial}{\partial x_i}\left(\rho u_i h_s\right) = \dot{\omega}_T + \frac{Dp}{Dt} + \frac{\partial}{\partial x_i}\left(\lambda\frac{\partial T}{\partial x_i}\right) + \frac{\partial u_i \tau_{ij}}{\partial x_j} \tag{3.4}$$

where the heat source term as the first term on the right-hand side of equation 3.4 is defined as follows:

$$\dot{\omega}_T = -\sum_{k=1}^{N} \Delta h^o_{f,k}\dot{\omega}_k \tag{3.5}$$

where $\dot{\omega}_{s,k}$ denotes the production/consumption rate of the k-th species and $\Delta h^o_{f,k}$ is the standard formation enthalpy of species k at T_0=298.15 K. The right-hand side of equation 3.4 also includes the source term for the pressure change (2nd term), the heat flux due to the conduction according to Fourier's law with λ as the heat diffusion coefficient (3rd term), and and the viscous heating source term (4th term).

In reacting flows, the species transport equation is solved in addition to the above-mentioned equations.

- Species mass fraction:

$$\frac{\partial \rho Y_k}{\partial t} + \frac{\partial \rho u_i Y_k}{\partial x_i} = \frac{\partial}{\partial x_i}\left(\rho D_k\frac{\partial Y_k}{\partial x_i}\right) + \dot{\omega}_k \tag{3.6}$$

where Y_k denotes the mass fraction of the k-th species. The first term on the right-hand side of equation 3.6 considers the change rate of the species mass fraction due to diffusive transport according to Fick's law, where D_k is the molecular diffusion of the k-th species. The second term represents the production/consumption rate of the k-th species. Since the equations 3.1 and 3.6 lead to an over determined equation system, equation 3.6 is

solved for N-1 species. The last species mass fraction, usually N_2, is determined as follows:

$$Y_N = 1 - \sum_{k=1}^{N-1} Y_k \tag{3.7}$$

In combustion engines the flow is generally turbulent. This leads to higher complexity in solving the above-mentioned equations than in laminar flows. Direct numerical simulation (DNS), large eddy simulation (LES), and (Unsteady) Reynolds-averaged Navier-Stokes (URANS and RANS) methods represent the approaches used to model the turbulent flows. The extent of turbulent scale resolution is the highest in DNS followed by LES. The RANS and URANS methods, based on the principle of Reynolds decomposition, take the effect of turbulence on the mean flow field into account by using a turbulence model. These approaches are computationally much more efficient and appropriate for engineering purposes. Hereafter the variable ϕ is splitted into the Reynolds-averaged ($\overline{\phi}$) and Reynolds-fluctuation (ϕ') components:

$$\phi = \overline{\phi} + \phi' \quad \text{with} \quad \overline{\phi'} = 0 \tag{3.8}$$

In the context of turbulent flows with variable density due to combustion/compression, the mass-weighted averaging known as Favre averaging is preferred [32–34]:

$$\widetilde{\phi} = \frac{\overline{\rho\phi}}{\overline{\rho}} \tag{3.9}$$

The variable ϕ is splitted into the Favre-averaged $\widetilde{\phi}$ and Favre-fluctuation term ϕ'':

$$\phi = \widetilde{\phi} + \phi'' \quad \text{with} \quad \widetilde{\phi''} = 0 \tag{3.10}$$

Using the mathematical convention above, the Favre-averaged balance equations are as follows:

- Mass:

$$\frac{\partial \overline{\rho}}{\partial t} + \frac{\partial}{\partial x_i}\left(\overline{\rho}\widetilde{u}_i\right) = 0 \tag{3.11}$$

- Momentum:

$$\frac{\partial \overline{\rho}\widetilde{u}_i}{\partial t} + \frac{\partial}{\partial x_i}\left(\overline{\rho}\widetilde{u}_i\widetilde{u}_j\right) + \frac{\partial \overline{p}}{\partial x_j} = \frac{\partial}{\partial x_i}\left(\overline{\tau}_{ij} - \widetilde{\overline{\rho}u_i''u_j''}\right) \tag{3.12}$$

- Sensible enthalpy:

$$\frac{\partial \overline{\rho}\widetilde{h}_s}{\partial t} + \frac{\partial}{\partial x_i}\left(\overline{\rho}\widetilde{u}_i\widetilde{h}_s\right) = \overline{\dot{\omega}}_T + \frac{\overline{Dp}}{Dt} + \frac{\partial}{\partial x_i}\left(\overline{\lambda\frac{\partial T}{\partial x_i}} - \overline{\rho}\widetilde{u_i''h_s''}\right) + \overline{\frac{\partial u_i \tau_{ij}}{\partial x_j}} \tag{3.13}$$

- Species mass fraction:

$$\frac{\partial\left(\overline{\rho}\widetilde{Y}_k\right)}{\partial t} + \frac{\partial}{\partial x_i}\left(\overline{\rho}\widetilde{u}_i\widetilde{Y}_k\right) = -\frac{\partial}{\partial x_i}\left(\overline{\rho}D_k\frac{\partial \widetilde{Y}_k}{\partial x_i} + \overline{\rho}\widetilde{u_i''Y_k''}\right) + \overline{\dot{\omega}}_k \tag{3.14}$$

From Favre averaging of the equations, new terms appear that need to be modeled. These unclosed terms include the Reynolds stresses $\widetilde{u_i''u_j''}$ as well as the enthalpy and species turbulent fluxes $\widetilde{u_i''h_s''}$ and $\widetilde{u_i''Y_k''}$, respectively. In addition, the source term $\overline{\dot{\omega}}_k$ due to combustion has to be modeled, which is described in Section 3.4. According to Boussinesq [35, 36], the Reynolds stresses can be expressed in terms of mean strain rate in the same way as the viscous stress for Newtonian isotropic fluid:

$$\overline{\rho}\widetilde{u_i''u_j''} = -\mu_t\left(\frac{\partial \widetilde{u}_i}{\partial x_j} + \frac{\partial \widetilde{u}_j}{\partial x_i} - \frac{2}{3}\delta_{ij}\frac{\partial \widetilde{u}_k}{\partial x_k}\right) + \frac{2}{3}\overline{\rho}k \tag{3.15}$$

The difference hereby is that the molecular viscosity is replaced by the so-called eddy viscosity μ_t, which is computed by applying a turbulence model. Following the classical gradient assumption, the enthalpy and species turbulent fluxes are closed through

$$\overline{\rho}\widetilde{u_i''h_s''} = -\frac{\mu_t}{Pr_t}\frac{\partial \widetilde{h}_s}{\partial x_i} \tag{3.16}$$

$$\overline{\rho}\widetilde{u_i''Y_k''} = -\frac{\mu_t}{Sc_t}\frac{\partial \widetilde{Y}_k}{\partial x_i} \tag{3.17}$$

Here, Pr_t and Sc_t refer to the turbulent Prandtl and Schmidt number, which consider enthalpy and species transport due to turbulence. In turbulent flows the molecular transport is much smaller than the turbulence induced transport and can therefore be neglected. The unclosed term μ_t is still to be modeled, which is described in the next section.

3.2 Turbulence Model

Most turbulence models are based on previously mentioned Boussinesq's assumption to model the eddy viscosity μ_t to close the Favre averaged equations. In the engineering applications the k-ϵ model as the two-equation model is widely used. Thereby, transport equations for the turbulent kinetic energy k and and its dissipation rate ϵ are solved. The turbulent kinetic energy is the mean kinetic energy per unit mass associated with the turbulent eddies, which gets dissipated by the viscous forces at the smallest turbulent scale, known as Kolmogorov scales. The transport equations for the turbulent kinetic energy k and its dissipation rate ϵ in the standard k-ϵ model are as follows [37]:

$$\frac{\partial}{\partial t}(\overline{\rho}k) + \frac{\partial}{\partial x_i}(\overline{\rho}\widetilde{u}_i k) = \frac{\partial}{\partial x_i}\left[\left(\mu + \frac{\mu_t}{\sigma_k}\right)\frac{\partial k}{\partial x_i}\right] + P_k - \overline{\rho}\varepsilon \tag{3.18}$$

$$\frac{\partial}{\partial t}(\overline{\rho}\varepsilon) + \frac{\partial}{\partial x_i}(\overline{\rho}\widetilde{u}_i \varepsilon) = \frac{\partial}{\partial x_i}\left[\left(\mu + \frac{\mu_t}{\sigma_\varepsilon}\right)\frac{\partial \varepsilon}{\partial x_i}\right] + C_{\varepsilon 1}\frac{\varepsilon}{k}P_k - C_{\varepsilon 2}\overline{\rho}\frac{\varepsilon^2}{k} \tag{3.19}$$

The source term P_k is defined as follows:

$$P_k = -\overline{\rho}\widetilde{u_i'' u_j''}\frac{\partial \widetilde{u}_i}{\partial x_j} \tag{3.20}$$

The model constants are as follows:

$$C_\mu = 0.09 \quad ; \quad \sigma_k = 1.0 \quad ; \quad \sigma_\varepsilon = 1.3 \quad ; \quad C_{\varepsilon 1} = 1.44 \quad ; \quad C_{\varepsilon 2} = 1.92 \tag{3.21}$$

The turbulent viscosity is then estimated as [37]

$$\mu_t = \overline{\rho} C_\mu \frac{k^2}{\varepsilon} \tag{3.22}$$

In the present work, the so-called k-ζ-f model developed by Hanjalic and Popovac [38,39], and based on Durbin's elliptic relaxation concept was employed. According to this turbulence model, two more equations are solved in addition to equations 3.18 and 3.19, leading to a 4-equation turbulence model. This model is based on the argument that the turbulent kinetic energy k is not the appropriate turbulent velocity scale, so that an

additional transport equation for the dimensionless velocity scale ratio ($\zeta = \overline{v^2}/k$) is solved:

$$\frac{\partial \rho\zeta}{\partial t} + \frac{\partial \left(\rho u_j \zeta\right)}{\partial x_j} = \frac{\partial}{\partial x_j}\left[\left(\mu + \frac{\mu_t}{\sigma_\zeta}\right)\frac{\partial \zeta}{\partial x_j}\right] + \rho f - \frac{\zeta}{k}P_k \tag{3.23}$$

The term ζ refers to the the velocity scale ratio and $\overline{v^2}$ to velocity fluctuations:

$$\overline{v^2} = \sum_{i=1}^{3} \overline{u_i'' u_i''} \tag{3.24}$$

The elliptical relaxation term f takes the near-wall turbulence anisotropy and nonlocal pressure effects into account, which is computed as follows: [40]:

$$L^2\nabla^2 f - f = L^2 \frac{\partial}{\partial x_j}\left(\frac{\partial f}{\partial x_j}\right) - f = \frac{1}{T}\left(C_1 - 1 + C_2'\frac{P}{\rho\varepsilon}\right)\left(\zeta - \frac{2}{3}\right) \tag{3.25}$$

T and L are the turbulent time and length scale defined as:

$$\begin{aligned} T &= \max\left[\min\left(\tfrac{k}{\varepsilon}, \tfrac{0.6}{\sqrt{6}C_\mu |S|\zeta}\right), C_T\left(\tfrac{\nu}{\varepsilon}\right)^{1/2}\right] \\ L &= C_L \max\left[\min\left(\tfrac{k^{3/2}}{\varepsilon}, \tfrac{k^{1/2}}{\sqrt{6}C_\mu |S|\zeta}\right), C_\eta\left(\tfrac{\nu^3}{\varepsilon}\right)^{1/4}\right] \end{aligned} \tag{3.26}$$

with S as mean strain rate:

$$S = \sqrt{2S_{ij}S_{ij}} \qquad S_{ij} = \frac{1}{2}\left(\frac{\partial u_i}{\partial x_j} + \frac{\partial u_j}{\partial x_i}\right) \tag{3.27}$$

The first terms in the formulation of T and L are known as the integral time and length scale associated with the largest eddies and the second terms correspond to the time and length scale of the smallest eddies known as the Kolmogorov scale. The "min" bound of the turbulence scales is introduced as the constraint of the model to suppress the overprediction of the eddy viscosity in stagnation point regions with high rates of normal strain [41]. The "max" bound considers that the turbulence scales can not be less than the corresponding Kolmogorov scales [42]. The turbulent viscosity μ_t is then calculated using:

$$\mu_t = \rho C_\mu \zeta k T \tag{3.28}$$

The corresponding coefficients are given as :

$$C_\mu = 0.22; \quad \sigma_k = 1.0; \quad \sigma_\varepsilon = 1.3; \quad \sigma_\varsigma = 1.2; \quad C_{\varepsilon 1} = 1.4[1 + 0.012/\zeta]$$
$$C_{\varepsilon 2} = 1.9; \quad C_1 = 1.4; \quad C_2' = 0.65; \quad C_T = 6\,; \quad C_L = 0.36; \quad C_\eta = 85$$

3.3 Regimes of Turbulent Premixed Combustion

The so-called combustion regime diagram (Figure 3.1) proposed by Borghi [43] and extended by Peters [44], characterizes the possible scenarios of turbulence-chemistry interaction in turbulent combustion. This enables the modeling of an appropriate closure term for $\overline{\dot{\omega}}_k$, which is described in the next section. The turbulence and chemistry interactions are evaluated by comparing their respective length and time scales and by introducing different dimensionless numbers as follows. The turbulent Reynolds number is defined as

$$Re_t = u' l_t / \nu \tag{3.29}$$

where l_t is the integral length scale, u' is the velocity fluctuations and ν is the kinematic viscosity. The Damköhler number Da corresponds to the ratio of integral time scale τ_t to chemical time scale τ_c as follows:

$$Da = \frac{\tau_t}{\tau_c} = \frac{l_t / u'}{\delta_L / s_L} \tag{3.30}$$

where δ_L and s_L are the laminar flame thickness and unstrained laminar flame velocity, respectively. The Karlovitz number Ka is defined as the ratio between the chemical time scale and Kolmogorov time scale τ_η:

$$Ka = \frac{\tau_c}{\tau_\eta} = \frac{\delta_L / s_L}{\sqrt{\nu/\epsilon}} = \left(\frac{\delta_L}{l_\eta}\right)^2 \tag{3.31}$$

Various combustion regimes can be categorized in terms of length ratios ($l_t\ /\delta_L$) and velocity ratio ($u'\ /s_L\ $) as shown in Figure 3.1

When $Da \ll 1$, the chemical time scales are larger than the turbulence ones, implying that combustion is entirely controlled by chemistry. High turbulence, namely high fluctuating velocity, results in intensive mixing of the combustion products with reactants like in perfectly stirred reactors. For $Da \gg 1$ the chemical time scale is shorter than the integral tur-

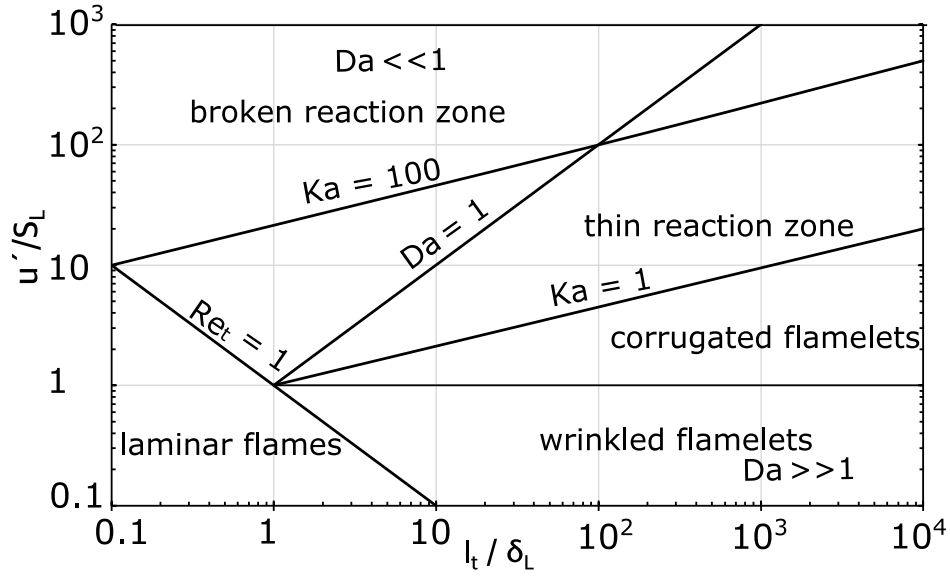

Figure 3.1: Turbulent combustion regimes proposed by Borghi and extended by Peters in terms of length scales ratios and velocity ratios [43, 44]

bulence time scale. This implies that the chemical reactions are faster than the speed of turbulence motions and the turbulence does not affect the flame inner structure. The flame can be modeled as ensemble of laminar flamelet surfaces, wrinkled by turbulence. The area with $Re_t < 1$ represents the laminar flame region. When $Ka < 1$, the chemical time scale is shorter than any turbulent time scales and the flame thickness is smaller than the Kolmogorov length scale. In the so-called wrinkled flamelet regime the flame front is thin and represents an ensemble of laminar flamelet wrinkled by turbulence. In the so-called corrugated flamelet region, the laminar flame thickness is still thinner than any turbulent length scales. However the turbulent velocity is higher than the flame speed ($u' > s_L$). As a result the turbulence motions wrinkle the flame front up to flame front interactions that leads to the formation of pockets of fresh and burned gases. The line $Ka = 1$ implies that the laminar flame thickness equals to the Kolmogorov length scale, which is known as the Klimov-Williams limit. This limit represents the transition between the flamelet combustion regime and distributed combustion regime, where the turbulence leads to the distortion of the flame front. However, Peters showed that for $Ka > 1$, the reaction zone might not necessarily change. As the reaction zone, where the heat is released, is smaller than the flame

thickness ($\delta_r \approx 0.1\delta_L$) the zone of $1 < Ka < 100$ represents the thickened flame regime, for which the smallest turbulent eddies can penetrate the preheat zone but not the inner reaction zone.
In the next section the numerical approaches for closing the source term $\overline{\dot{\omega}_k}$ are introduced.

3.4 Numerical Approaches for Modeling Turbulent Combustion

Simple turbulent combustion models usually aim to predict the consumption rate of the fuel by considering a single one-step irreversible reaction:

$$\mathrm{Fu} + \mathrm{sO_2} \longrightarrow (1 + \mathrm{s})\mathrm{P}$$

where s denotes the stoichiometric coefficient. The mean consumption rate of the fuel can be formulated by averaging the Arrhenius equation is as follows:

$$\overline{\dot{\omega}_{Fu}} = \dot{\omega}_{Fu}(\widetilde{Y}_{Fu}, \widetilde{Y}_{O_2}, \widetilde{T}) = -k_0 \overline{\rho^2} \widetilde{T}^b \widetilde{Y}_{Fu} \widetilde{Y}_{O_2} \exp\left(-\frac{E_a}{R\widetilde{T}}\right) \tag{3.32}$$

where Y_{Fu} and Y_{O_2} denote the mass fractions of fuel and oxygen, respectively; E_a is the activation energy, k_0 is the pre-exponential factor, b is the temperature exponent, T is temperature, and R ≈ 8.314 $[j/(molK)]$ is the molar gas constant. In this formulation the effect of turbulence-chemistry interactions is not considered. It is assumed that the mean reaction rate corresponds to the reaction rate obtained by using mean local values of temperature $\widetilde{T}$ and mass fractions $\widetilde{Y}$. However, the strong non-linearity of the Arrhenius equation with temperature makes this formulation inadequate in turbulent flows with high fluctuating temperatures. This formulation would be appropriate for the flows with a low Damköhler number as the chemical time scales are larger than the turbulent time scales. To tackle the problems encountered by averaging the Arrhenius equation, different combustion models based on the previously described physical analysis of turbulent combustion have been proposed. The eddy break up (EBU) model introduced by Spalding [34,45,46] for turbulent flows with Re $\gg 1$ and Da $\gg 1$ assumes that in contrast to the previous Arrhenius model, the chemistry does not play an explicit role in mean reaction

rate. Thereafter, the mean consumption rate is controlled by the turbulent time scale and the temperature fluctuations. This model is attractive due to its simple formulation, which does not require any transport equation. There are a few combustion models in the literature that consider both turbulence and chemical effects on the mean reaction rate, including the probability density function (PDF) model [47,48], the level set approach using the G-equation [49,50] and the flamelet generated manifold FGM model [51,52]. The flame surface density model valid under the flamelet assumptions is also a widely used combustion model for predicting turbulent premixed and partial premixed combustion. This model has been applied successfully in modeling combustion in reciprocating engines ([53–56]). The flamelet assumption is considered to be valid in technical combustion systems such as reciprocating internal combustion engines, regarding that quenching does not occur [57]. According to the flamelet assumption the reaction occurs in an infinitely thin flame front that separates the unburned and burned zones. In this combustion regime, the flame thickness is smaller than all the turbulent scales (Ka $<$ 1), so that the flame front is modeled as ensemble of small laminar flames (flamelets) wrinkled by turbulence. The concept of the flame surface density model and its implementation is illustrated in Figure 3.2. The mean fuel con-

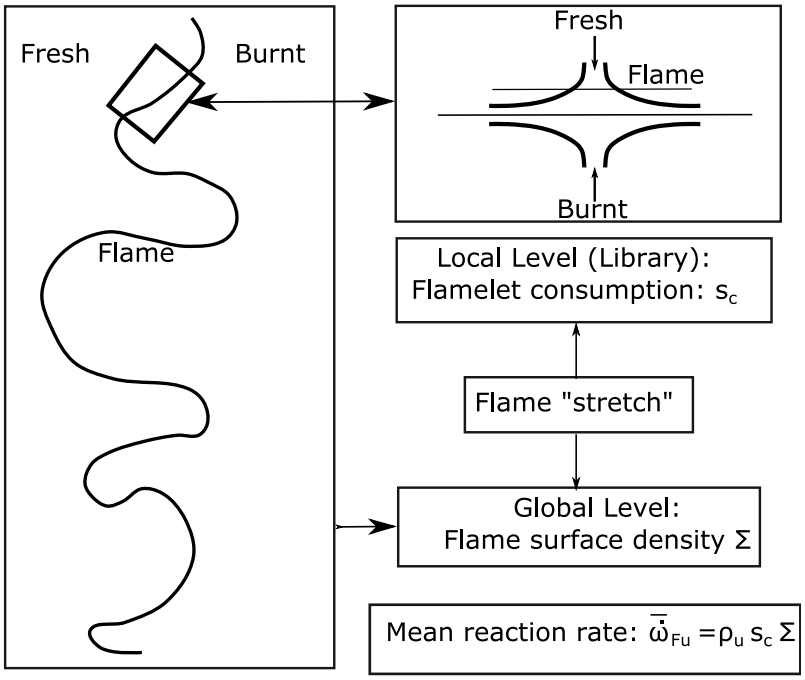

Figure 3.2: Concept of the flame surface density model [31]

sumption rate is expressed as the product of flame surface density Σ (i.e. the flame surface area per unit volume) by the local fuel consumption rate per unit of flame area $\rho_u \langle s_c \rangle_s$ [58, 59]

$$\overline{\dot{\omega}}_{Fu} = \rho_u \langle s_c \rangle_s \Sigma \tag{3.33}$$

where ρ_u is the fresh gas density and $\langle s_c \rangle_s$ as mean fuel consumption speed along the flame surface. The flame surface density Σ (m^2/m^3) considers the flame front wrinkling caused by the turbulence. The advantage of this model is the decoupled consideration of chemistry and turbulence. The effect of kinetics is considered by means of fuel consumption speed and the turbulence-chemistry interaction is taken into account by flame surface density. The consumption speed refers to the speed at which the flame burns the reactants. The DNS investigations of Harworth et. al. [60] revealed that, to the first order, the mean consumption speed can be substituted by the unstrained laminar flame speed s_L of freely propagating flame $s_c \approx s_L$. The laminar flame speed can be tabulated with respect to temperature, pressure, fuel-air equivalence ratio, and EGR if needed by employing detailed kinetics in Cantera or Chemkin.

The flame surface density Σ can be modeled either algebraically or by solving a transport equation for Σ. The transport equation for Σ in its closed form can be given as follows:

$$\frac{\partial \Sigma}{\partial t} + \frac{\partial \widetilde{u}_i \Sigma}{\partial x_i} = \frac{\partial}{\partial x_i}\left(\frac{\nu_t}{\sigma_\Sigma}\frac{\partial \Sigma}{\partial x_i}\right) + \kappa_m \Sigma + \kappa_t \Sigma - D \tag{3.34}$$

where κ_m and κ_t are strain rates contributions on flame surface production induced by mean flow field and turbulence motions, respectively. D considers the annihilation of the flame surface due to the reactant consumption; ν_t is the turbulent kinematic viscosity; and σ_Σ is the flame surface turbulent Schmidt number. Various closures formulations of the source terms in equation 3.34 exist. These source terms for the CFM model are given in Table 3.1 [61, 62]. The ECFM3Z model employed in this thesis and described in the following section uses the same closure terms: where α_0 and β_0 are model parameters, and ρ_{TFu} and ρ_{Fu} correspond to the density of tracer fuel (without consumption) and fuel being consumed due to combustion. The flame stretch generated by turbulence is estimated as $\kappa_t = \varepsilon/k$ corrected with the efficiency factor Γ_K, according to the Intermit-

Table 3.1: Source and sink terms of the flame surface density balance equation 3.34 according to CFM Model

$\kappa_m\Sigma$	$\kappa_t\Sigma$	D
$A_{ik}\frac{\partial \widetilde{u}_k}{\partial x_i}\Sigma$	$\alpha_0\Gamma_K\frac{\varepsilon}{k}\Sigma$	$\beta_0\frac{\overline{\rho}_{TFu}s_L}{\overline{\rho}_{Fu}}\Sigma^2$

tent Turbulent Net Flame Stretch (ITNFS) model [63–65]. This function accounts for the interaction of the eddies and the flame front depending on velocity and length ratios $\Gamma_K\left(\frac{u'}{s_L},\frac{l_t}{\delta_L}\right)$ and is determined in DNS simulations of flame vortex interaction [66]. κ_m is usually neglected compared to κ_t. Based on the described flame surface density model, the ECFM3Z model proposed by Colin [67] was used in thesis for modeling of DF combustion, which is described in the following section.

3.5 ECFM3Z Combustion Modeling of DF Engine

The Numerical investigation of combustion in a diesel-NG DF engine requires the modeling of ignition in the mixture of vaporized diesel and NG-air followed by flame propagation in the premixed lean mixture. URANS simulations coupled with detailed kinetics have been employed in various studies, to cover the ignition and combustion of both fuels [68–70]. The employed kinetics included both n-heptane (as a diesel substitute) and methane (as NG substitute) oxidation reaction paths. However, the turbulence-chemistry interaction as described in the previous section has not fully been taken into account. Turbulence has been considered merely by computing the reaction rates employing Arrhenius equations with the Favre averaged properties, namely $\widetilde{T}$ and $\widetilde{Y}_i$. In addition to this limitation the computational times are high. The 3-Zones Extended Coherent Flamelet (ECFM3Z) model proposed by Colin et. al. [67] is an approach that can consider all combustion regimes in a single model. This model is an improvement of the Extended Coherent Flamelet Model (ECFM) developed by the same author for modeling premixed/partially premixed combustion [71].

The ECFM model belongs to the family of flame surface density models described in the previous section, which enables the modeling of premixed and partially premixed combustion and has been tested suc-

cessfully in modeling gasoline engines reported by different authors [72,73]. Thereby, the turbulence-chemistry interaction is modeled under the flamelet assumption using the flame surface density model, which accounts for the effect of turbulence on flame front wrinkling. The key feature of the ECFM model is the conditional averaging technique. The local properties of the unburned gas (mixture composition, density, temperature) for computing the flame speed in fresh gas as well as the properties of the burned gas for modeling the pollutant formation are reconstructed accurately in a computational cell. The ECFM3Z model as the extension of the ECFM model can additionally account for auto-ignition and mixing controlled combustion. This has been achieved by adding an appropriate auto-ignition model [74], mixing model and diffusion combustion in addition to the features of ECFM model. The feasibility of this model in predicting DF combustion was demonstrated in [75], where a transition from auto-ignition to propagating flame was captured by modeling an initial flame surface density. The combustion modeling of the investigated diesel-NG DF engine in the framework of the ECFM3Z model is described as it follows: The computational cell is splitted into three subdomains: (1) an unmixed zone containing pure n-heptane (as a diesel surrogate), (2) a zone with methane (as a NG substitute)-air mixture, and (3) the mixed zone that is evolved through progressive mixing of n-heptane with the methane-air mixture in the computational cells. The conditional averaging technique is applied to each of these zones, characterized by the superscript u for the unburned and b for the burned state. The different subgrid zones in the ECFM3Z model and their evolution are sketched in Figure 3.3. Initially just the zone A^u exists, corresponding to the methane-air mixture and F^u, which represents the mass of the injected and evaporated n-heptane (Case A). The mixing model allows to progressively transfer the masses in zones A^u and F^u in the mixed zone M^u (Case B). The auto ignition delay time is computed in zone M^u. When the ignition criterion is fulfilled, auto-ignition occurs and the fresh gas in M^u is rapidly consumed. Following ignition, the fuel consumption due to premixed combustion also occurs in zone M^u (Case C). The combustion products form the region M^b, where the post-flame kinetics are computed using Arrhenius equations. The post-flame calculations include the oxidation of possibly remaining fuel in the case of rich mixtures or diffusion combustion as well as the prediction of pollutant emission such as NO (Case D). To

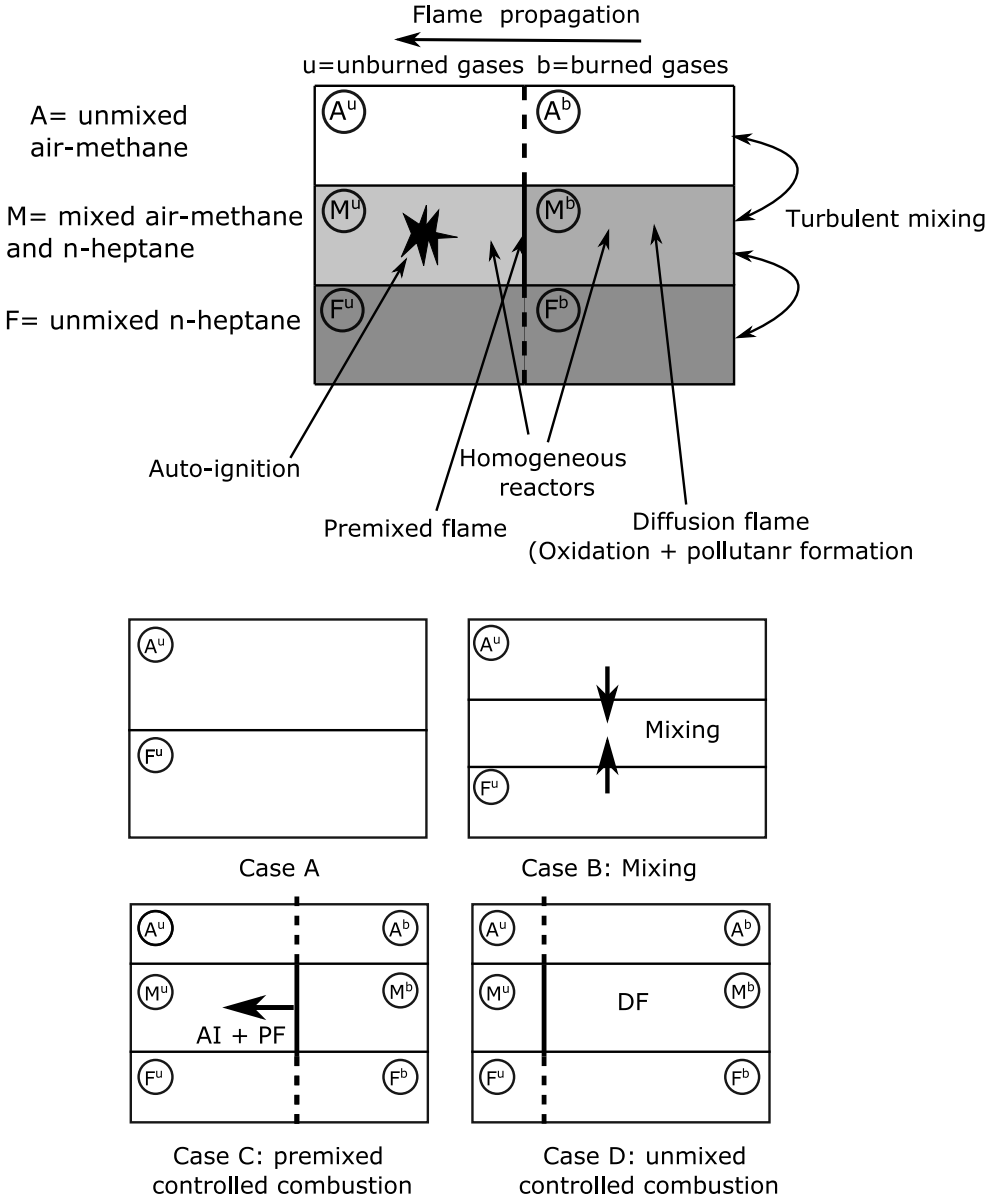

Figure 3.3: Subgrid zones according to the ECFM3Z model and their evolution [67]

predict auto-ignition and premixed combustion in the fresh gas zone M^u as well as post-flame reactions and pollutant formation in the burned gas zone M^b, the gas properties, namely species mass fractions and temperatures in these regions, must be reconstructed. This is achieved by solving a set of transport equations and employing a conditional averaging technique.

A brief description of the model implementation is given as follows. A much more detailed description can be found in [67]. The first set of transport equations are solved for the Favre averaged density of the global

species, namely fuels (n-heptane and methane), O_2, N_2, NO, CO_2 ,CO, H_2O, H, O, OH, and NO:

$$\frac{\partial \overline{\rho}\widetilde{Y}_k}{\partial t} + \frac{\partial \overline{\rho}\widetilde{u}_i\widetilde{Y}_k}{\partial x_i} = \frac{\partial}{\partial x_i}\left(\left(\frac{\mu}{Sc} + \frac{\mu_t}{Sc_t}\right)\frac{\partial \widetilde{Y}_k}{\partial x_i}\right) + \overline{\dot{\omega}}_k \tag{3.35}$$

The transport equations predict the evolution of the species mass fractions in the computational cell. Thereby μ and μ_t denote the laminar and turbulent viscosities, respectively, and Sc and Sc_t are the laminar and turbulent Schmidt numbers. The source term $\overline{\dot{\omega}}_k$ considers the consumption of n-heptane and methane starting with auto-ignition followed by premixed or diffusion combustion. The consumption/production rates of the other species are based on the stoichiometry balance equations and equilibrium assumptions. For each of the aforementioned species so-called tracers are transported according to equation 3.35, for which $\overline{\dot{\omega}}_{s,k}$ equals zero. These variables are required to predict the mixture composition in zone M^u. The state of combustion under the flamelet assumption can be tracked via the progress variable $\widetilde{c}$, which is proportional to the oxidized fuel mass fraction since the start of combustion:

$$\widetilde{c} = 1 - \frac{\overline{m}^u}{\overline{m}} = 1 - \frac{\widetilde{Y}^u_{Fu1} + \widetilde{Y}^u_{Fu2}}{\widetilde{Y}_{TFu1} + \widetilde{Y}_{TFu2}} \tag{3.36}$$

where $\widetilde{Y}^u_{Fu1}$ and $\widetilde{Y}^u_{Fu2}$ are the unburned n-heptane and methane species mass fractions and $\widetilde{Y}_{TFu1}$ and $\widetilde{Y}_{TFu2}$ are their tracer mass fractions. The mixing state of gaseous n-heptane in the background methane-air mixture in the zone M is described by solving transport equations for the so-called fictious unmixed quantities for n-heptane ($\widetilde{Y}^F_{Fu1}$), CH_4 ($\widetilde{Y}^A_{Fu2}$), O_2 ($\widetilde{Y}^A_{O2}$) and their tracers. The mixing rate as the source term for these transport equations is proportional to the volume fraction of the species and a characteristic mixing time scale proportional to the turbulent time scale k/ϵ. Knowing the global species mass fractions and the unmixed quantities, it is possible to reconstruct the mixed quantities by applying mass conservation of the species in the cell. For example the density of the fuel tracer of n-heptane in the mixed zone $\overline{\rho}^M_{TFu1}$ is

$$\overline{\rho}^M_{TFu1} = \overline{\rho}\widetilde{Y}^M_{TFu1} = \overline{\rho}_{TFu1} - \overline{\rho}^F_{Fu1} = \overline{\rho}\widetilde{Y}_{TFu1} - \overline{\rho}\widetilde{Y}^F_{Fu1} \tag{3.37}$$

where $\overline{\rho}^{F}_{Fu1}$ is the density of the unmixed Fu1 (n-heptane). For reconstructing the species mass fractions (global and their tracers) in each zone the conditioning technique is applied. With $\widetilde{Y}_k = \overline{\rho}_k/\overline{\rho}$ as the average mass fraction of species k, the average mass fraction of species k contained in zone Z is $\widetilde{Y}^Z_k = \overline{\rho}^Z_k/\overline{\rho}$. Following this, the mass fraction of species k in zone Z conditioned to this zone is given by:

$$\widetilde{Y}^Z_k\Big|_Z = \frac{\overline{\rho}^Z_k}{\overline{\rho}^Z} = \frac{\widetilde{Y}^Z_k}{\widetilde{Y}^Z} \tag{3.38}$$

The mass fractions in the fresh gas, such as for n-heptane, can be given as

$$\widetilde{Y}^{u,M}_{Fu1}\Big|_{u,M} = \frac{\overline{\rho}^M_{TFu1}}{\overline{\rho}^M} = \widetilde{Y}^M_{TFu1}\Big|_M \tag{3.39}$$

which states that the mixture composition in the unburned fresh gas equals the average composition if no combustion would have occurred, given by the fuel tracer in the mixed zone. To reconstruct the species mass fraction such as O, OH and NO in the burned gas the classical relationship between the mean value, the unburned one and progress variable c is used as follows:

$$\widetilde{Y}^{b,M}_x\Big|_{b,M} = \frac{\widetilde{Y}^M_x\Big|_M - (1-\widetilde{c})\widetilde{Y}^{u,M}_x\Big|_{u,M}}{\widetilde{c}} \tag{3.40}$$

In analogy to the reconstruction of the mass fractions in the burned gas, the burned gas enthalpy for predicting the correct burned gas temperature is calculated using

$$\widetilde{h} = (1-\widetilde{c}_{b,M})\,\widetilde{h}^u + \widetilde{c}_{b,M}\widetilde{h}^b \tag{3.41}$$

where $\widetilde{c}_{b,M}$ is the mass fraction of zone M^b and thus $1-\widetilde{c}_{b,M}$ is the mass fraction at the fresh gas temperature T^u. $\widetilde{h}^u$ refers to the fresh gas enthalpy calculated by the transport equation

$$\frac{\partial}{\partial t}\left(\overline{\rho}\widetilde{h}^u\right) + \frac{\partial}{\partial x_i}\left(\overline{\rho}\widetilde{u}_i\widetilde{h}^u\right) = \frac{\partial}{\partial x_i}\left((\frac{\mu}{Pr} + \frac{\mu_t}{Pr_t})\frac{\partial \widetilde{h}^u}{\partial x_i}\right) + \rho\varepsilon + \frac{\rho}{\rho_u}\frac{\partial p}{\partial t} + \overline{h}_{evap} \tag{3.42}$$

where h_{evap} is heat loss caused by evaporation of the liquid phase. Through the above-mentioned equations, the mixture composition and temperature relevant for predicting auto-ignition, premixed combustion, and pollutant formation can be computed.

In the following sections, appropriate models for predicting auto-ignition as well as computing the laminar flame speed in the fresh gas of n-heptane-methane-air are described.

3.6 Ignition Delay Time Model

Locally auto-ignition leads to a rapid consumption of the mixed fuel and air. The modeling challenge is to predict the location and the instance of this occurrence. Classical diesel auto-ignition models such as those proposed by Halstead et. al. [76] (shell model) and Pinchon [77] are based on an oversimplified consideration of the effect of chemistry on auto-ignition, which is not accurate enough for modeling auto-ignition in diesel or DF engines due to their complex chemistry. On the other side, capturing auto-ignition by employing detailed kinetics is not computationally efficient in 3D modeling of engine combustion. Another approach suitable for 3D modeling is the tabulation method proposed by Pires Da Cruz [78], which relies on the a priori generation of a look-up table from simulations in homogeneous reactors in Chemkin [79] or Cantera employing complex chemistry. The principle of this method is illustrated in figure 3.4 using the temperature evolution in n-heptane/air mixture in a constant volume reactor calculated in Cantera using the LLNL v3 mechanism [80]. N-heptane is used as a surrogate for diesel as its cetane-number (CN) is similar to that of diesel fuel, leading to similar auto-ignition delay times. In the case of high temperature ignition (T=1000K), the start of heat release is characterized by solely one time τ_{HT}. Following this time the total heat of the reaction is released in a small time interval. In the case of low temperature ignition, however the heat release (shown as the temperature rise) occurs in two stages. The first stage known as cold flame characterizes an ignition delay time τ_{LT}, after which only a low amount of the total heat gets released rapidly. Following the first heat release, the reactions slow down until the second delay time τ_{HT} is reached. At this time the main heat release occurs rapidly.

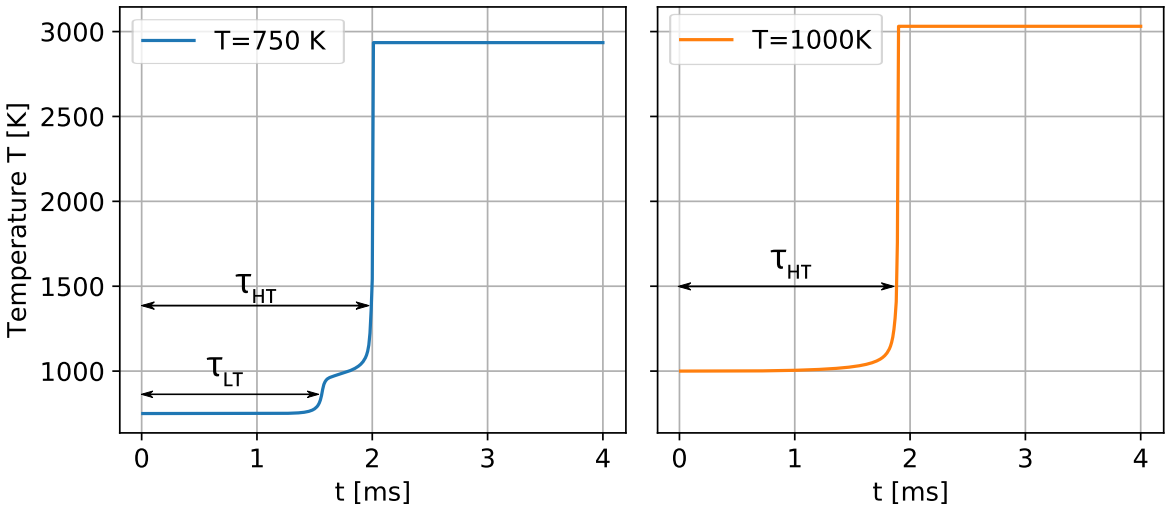

Figure 3.4: Cold flame ignition delay time τ_{LT} and main ignition delay time τ_{HT} for n-heptane air mixture with fuel-air equivalence ratio ϕ=1 under an initial pressure of 1.5 MPa and initial temperatures of T= 750 K (left) and T=1000 K (right) in a constant volume reactor

In the look-up table, the cool flame τ_{LT} (if present) and the main flame ignition delay times τ_{HT} are stored with respect to temperatures, pressures, fuel-air equivalence ratios and EGR (if applicable) through simulations using the homogeneous constant volume reactor. The tabulated times correspond to the instances of maximum temperature derivative versus time during the cool flame ignition and main ignition. In addition the heat releases at τ_{LT} and τ_{HT}, namely h_1 and h_{max} are tabulated, respectively. The fuel consumption during the cool flame is limited to the ratio $h_1 \ / h_{max}$.

To capture the ignition delay time in DF correctly, the interaction between the fuels n-heptane and methane must also be considered. The RCEM experimental investigation of Schlatter et. al. [29,30] showed prolonged ignition delay under the presence of methane compared with that of the pure diesel. Auto-ignition in DF engines is affected by the lower compression end temperatures. For accurate prediction of auto-ignition, a suitable reaction mechanism is required, particularly in the low-temperature regime.

In the literature, several kinetic mechanisms have been developed and validated for NG or n-heptane. To the authors knowledge, there is no validated mechanism for n-heptane/methane fuel blend. For this reason the

kinetic mechanisms employed in modeling DF combustion in different studies rely on the mechanisms validated for n-heptane, which also include the submechanisms for CH_4 oxidation. However, there are a few of them, which might be appropriate for modeling the ignition in DF combustion.

A comprehensive study was conducted by Jud [81] on the performance of the LLNL, Chalmers [82] and Rahimi [83] kinetic mechanisms in predicting the ignition delay times in n-heptane-methane-air mixtures. In his dissertation, these mechanisms were compared with the experimental results of a rapid compression expansion machine (RCEM), where diesel was injected into the background mixture of methane-air. He demonstrated that the Chalmers and Rahimi mechanisms can reproduce the ignition delay times fairly well for the temperature range of 750K-870K and an equivalence ratio of the methane-air mixture of ϕ=0.5.

Schiffner [84, 85] also investigated the performance of the LLNL and the Chalmers mechanism in predicting the ignition of n-heptane-methane-air mixture. He reported better performance of the Chalmers versus the LLNL mechanism when predicting ignition delay times at low temperature levels.

The look-up table used in the present work for modeling auto-ignition, had already been generated and incorporated successfully in AVL-Fire in the previous work conducted at the Thermodynamics Institute by Schiffner [84]. The cold flame and main flame ignition delay times as well as the corresponding heat releases were evaluated by using the temperature evolution, computed with the constant volume reactor model by employing the Chalmers mechanism. The reactor calculations were carried out for different temperatures, pressures, fuel-air equivalence ratios and fuel fractions as ratios of n-heptane to total fuel mass (n-heptane and methane). The evaluated ignition delay times and heat releases were stored in the look-up table with respect to the aforementioned parameters, leading to a 4D look-up table.

During the CFD calculation the ignition delay times in each computational cell are retrieved from the look-up table using the local mean unburned temperature $\widetilde{T}^u$, mean pressure p, mean equivalence ratio $\overline{\phi}$ and mean fuel fraction $\overline{FF}$:

$$\tau_{AI} = f(\widetilde{T}^u, p, \overline{\phi}^{u,M}\Big|_{u,M}, \overline{FF}^{u,M}\Big|_{u,M}) \tag{3.43}$$

The mean fuel fraction employing the conditioning technique of the ECFM3Z model is given as follows:

$$\overline{FF}^{u,M}\Big|_{u,M} = \frac{\widetilde{Y}^{u,M}_{Fu2}\Big|_{u,M}}{\widetilde{Y}^{u,M}_{Fu1}\Big|_{u,M} + \widetilde{Y}^{u,M}_{Fu2}\Big|_{u,M}} = \frac{\widetilde{Y}^{M}_{TFu2}\Big|_{M}}{\widetilde{Y}^{M}_{TFu1}\Big|_{M} + \widetilde{Y}^{M}_{TFu2}\Big|_{M}} \tag{3.44}$$

where $\widetilde{Y}_{TFu1}$, $\widetilde{Y}_{TFu2}$ are the tracer mass fractions of n-heptane and methane, respectively. For predicting the location and the instance of ignition in CFD a transport equation for an indicator species $\widetilde{Y}_I$ is solved:

$$\frac{\partial(\overline{\rho}\widetilde{Y}_I)}{\partial t} + \frac{\partial(\overline{\rho}\widetilde{u}_j\widetilde{Y}_I)}{\partial x_j} = \frac{\partial}{\partial x_j}((\frac{\mu_t}{Sc_t} + \frac{\mu}{Sc})\frac{\partial\widetilde{Y}_I}{\partial x_j}) + \overline{\rho}\widetilde{\dot{\omega}_I} \tag{3.45}$$

The source term $\dot{\omega}_I$ on the right-hand side of equation 3.45 is calculated using the tabulated ignition delay times scaled by the local fuel mass fractions:

$$\widetilde{\dot{\omega}}_I = C_{AI}(\widetilde{Y}_{TFu1} + \widetilde{Y}_{TFu2})F(\tau_{AI}) \tag{3.46}$$

where τ_{AI} is the ignition delay time retrieved from the look-up table. The model constant C_{AI} is introduced for adjusting the simulations results with the experimental ones. The function $F(\tau_{AI})$ must fulfill the criterion of

$$\int_0^{\tau_{AI}} F(t)dt = 1 \tag{3.47}$$

This can be achieved by, for example, setting $F(\tau_{AI}) = 1/\tau_{AI}$. An extension of this formulation proposed by da Cruz [78] is used and adapted to the investigated DF combustion:

$$F(\tau_{AI}) = \frac{\sqrt{\left(B^2\tau_{AI}^2 + 4(1 - B\tau_{AI})\frac{\widetilde{Y}_I}{\widetilde{Y}_{TFu1}+\widetilde{Y}_{TFu2}}\right)}}{\tau_{AI}} \tag{3.48}$$

If the indicator species Y_I in a computational cell fulfills the criterion of

$$\widetilde{Y}_I \geq (\widetilde{Y}_{TFu1} + \widetilde{Y}_{TFu2}) \tag{3.49}$$

then the main ignition delay time is reached and the fuel species are consumed according to $\overline{\omega}_{Fu,i} = -\overline{\rho}_u\frac{\widetilde{Y}_{Fu,i}}{\tau_c}$, where τ_c refers to the characteristic chemical time scale . For modeling the cold flame ignition a second indi-

cator species is transported according to equation 3.45, where the tabulated cold flame ignition delays are retrieved and used for computing the source term according to equation 3.46. In the case the cold flame ignition occurs, the fuel consumption is limited to $h_1/h_{\max}$. The corresponding enthalpies are taken from the look-up table.

3.7 Premixed Flame Propagation Modeling

Following ignition, a flame kernel develops and the flame front propagates in the mixture of n-heptane-methane-air or rather methane-air as the combustion proceeds. The turbulent reaction rate of the fuel is calculated using the flame surface density model as follows:

$$\begin{aligned} \overline{\dot{\omega}}_{Fu1} &= \overline{\rho}_u \widetilde{Y}_{TFu1} s_L \Sigma \\ \overline{\dot{\omega}}_{Fu2} &= \overline{\rho}_u \widetilde{Y}_{TFu2} s_L \Sigma \end{aligned} \tag{3.50}$$

where ρ_u is the unburned gas density, Σ is the flame surface density from equation 3.34, and Y_{TFu1} and Y_{TFu2} are n-heptane and methane tracer mass fractions. The ECFM3Z model requires a start value for the initial flame surface density following the onset of ignition. For setting the initial flame surface density the approach introduced by Colin et. al. [71] and adapted by Belaid Saleh [75] in context of DF applications is used:

$$\Sigma_{ini} = C \times |\nabla \widetilde{c}| \times \left(1 + \frac{\sqrt{k}}{\widetilde{u}}\right) \tag{3.51}$$

It is based on the gradient of the progress variable $\widetilde{c}$ and considers the influence of turbulence wrinkling using the ratio of turbulent kinetic energy k and the mean velocity $\widetilde{u}$ on the regime transition from auto-ignition to flame front propagation. The constant C can be seen as an adjustment for regime transition and can take values between 0 and 1.

The unstrained laminar flame velocity s_L is still to be evaluated. The mixture of n-heptane and methane must be considered in the zones, where both fuels exist. Experimental studies conducted by Li [86] re-

vealed a linear behavior of laminar flame speed with respect to the fuel mixture ratio φ defined as

$$\varphi = \frac{X_{C7H16}}{X_{C7H16} + X_{CH4}} \tag{3.52}$$

where X_i as the mole fractions of the fuels. Thus, the influence of the fuel mixture ratio on laminar flame speed during CFD calculation is considered by linear interpolation of the laminar flame speeds of n-heptane ($s_{L_{C7H16}}$) and methane ($s_{L_{CH4}}$) according to [87]:

$$s_{L_{DF}} = s_{L_{C7H16}} \varphi + s_{L_{CH4}} (1 - \varphi) \tag{3.53}$$

In the present work, the unstretched laminar flame speed of n-heptane was calculated by using the Chalmers mechanism and that of methane by using the Gri 3.0 mechanism in Cantera. The calculated flame speeds for n-heptane and methane were tabulated in two look-up tables with respect to temperature, pressure and fuel-air equivalence ratio, leading to two 3D look-up tables. During CFD calculation, each flame speed is retrieved from the corresponding table, depending on the local mean unburned temperature, pressure, and conditioned unburned equivalence ratio:

$$s_L = f\left(\widetilde{T}^u, p, \overline{\phi}^{u,M}\Big|_{u,M}\right) \tag{3.54}$$

The flame speed in each computational cell in CFD is then computed by using equation 3.53. The introduced look-up tables for auto-ignition delay times and laminar flame speeds are used for simulating two operation points in the context of the ECFM3Z model.

3.8 Setup of the Simulation

In this work, the DF test engine of MAN was simulated. The engine specifications are presented in Table 3.2. The intake stroke during opened inlet valves was not simulated. The simulations included the combustion and expansion stroke with closed valves as well as the exhaust stroke as the exhaust valves were open. The corresponding domains are illustrated in Figure 3.5. On the left upper side of the figure, the sketch of the engine during the closed valves is depicted, which was meshed and used

Table 3.2: Engine specifications of the MAN test engine

Parameter	Value
Bore x stroke	35 cm x 44 cm
Compression ratio	12
Exhaust valve opening/closing	499 °CA / 754 °CA
Injector Nozzle diameter	0.16 mm
Number of nozzle holes	5
Engine speed	750 r/min
Pilot injector offset from center (Δx,Δz)	(-3.9 cm,-3.9 cm)

for computations from 320 °CA up to 499 °CA. On the lower left side of the figure, the sketch of the engine with exhaust manifolds is shown, which was meshed and used during the exhaust stroke as the exhaust valves are open. It is to be noted that the crank angles are given in absolute values with 360 °CA referring to the top dead center with closed valves. The domains (with closed valves and with opened exhaust valves) were meshed using polyhedral cells in AVL-Fire, as shown in Figure 3.6 for the computed domain during the opened exhaust valves. The cell size on the walls (surface cells) was set to 1 mm and the volume cells were 2 mm wide. The grid cells in crevice regions as well as at exhaust valve seat were refined. The calculations were initialized at 320 °CA during the compression stroke. The initial methane-air mixture fraction as well as initial turbulence field in the chamber were assumed to be homogeneous. The corresponding initial turbulent kinetics energy k_{ini} and dissipation rate ϵ_{ini} were taken from MAN's cold flow simulations. Two operation points were simulated. The initial conditions are presented in Table 3.3. N-heptane was taken as the diesel surrogate. The onset of the ignition has been adjusted to the experimental results using the pre-factor introduced in equation 3.46. In addition, the model constant α_0 of the ECFM3Z model described in table 3.1 was adjusted to reproduce the experimental heat release rates.

For spray calculation the liquid phase was treated as a large number of discrete computational parcels, spread over the flow domain according to Dukowicz's Discrete Droplet Method (DDM) [88]. In this approach,

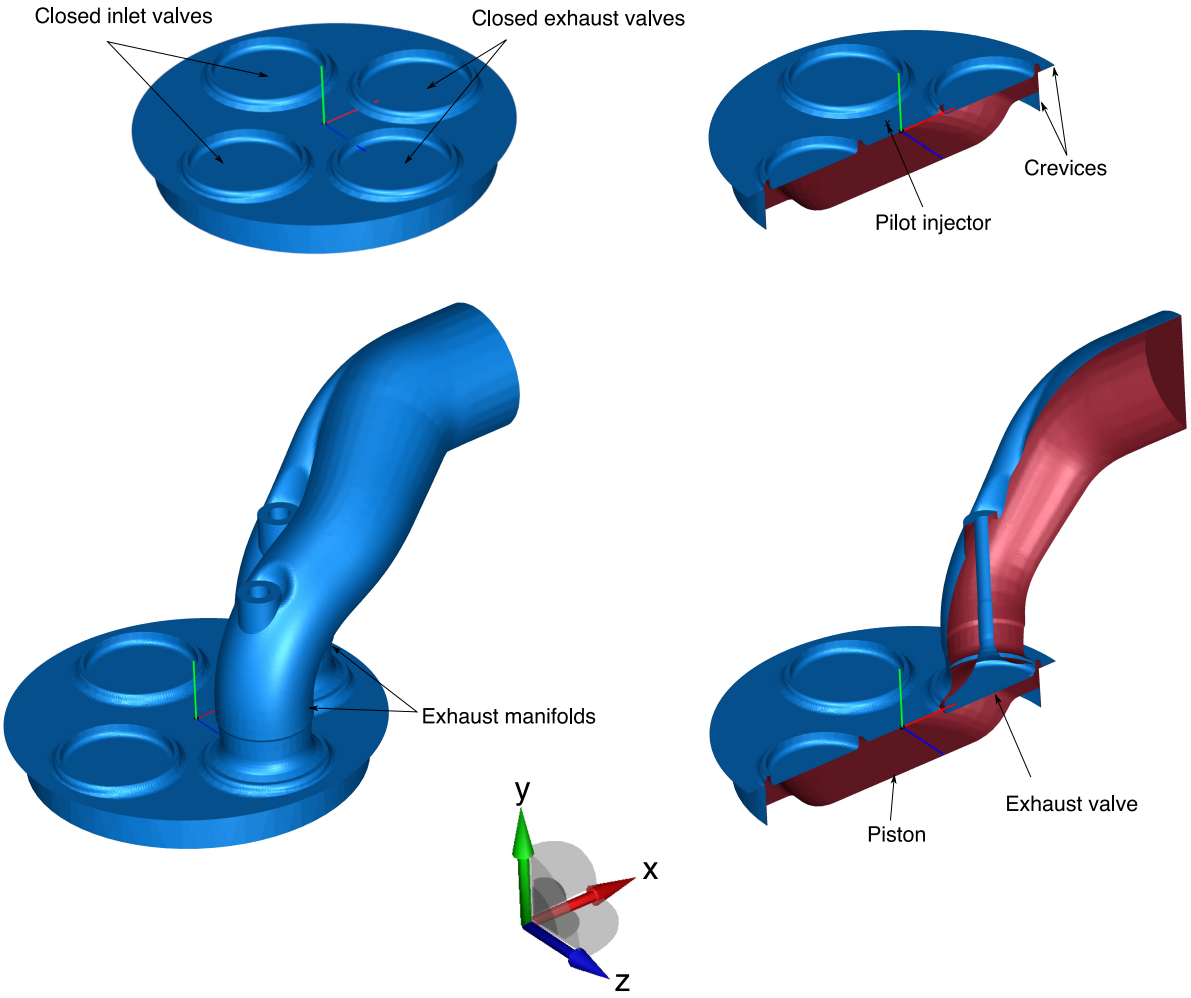

Figure 3.5: Simulated domain during the combustion and expansion stroke with closed valves up to 499 °CA (upper left) an that during the exhaust stroke (lower left); Cross sectional views in z direction (right)

each computational parcel represents a finite number of droplets of identical properties in terns of their location, diameter, velocity and temperature. The subsequent evolution of the properties of droplets are tracked through the continuous flow field by solving ordinary differential equations for their momentum as well as heat and mass transfer. The droplets are tracked in a Lagrangian way. The the two-way coupling between the statistical parcels with the continuous gas phase is taken into account in a Lagrange-Euler framework [89]. The amount of fuel injected and the corresponding injection rates were acquired from measurements. The at-

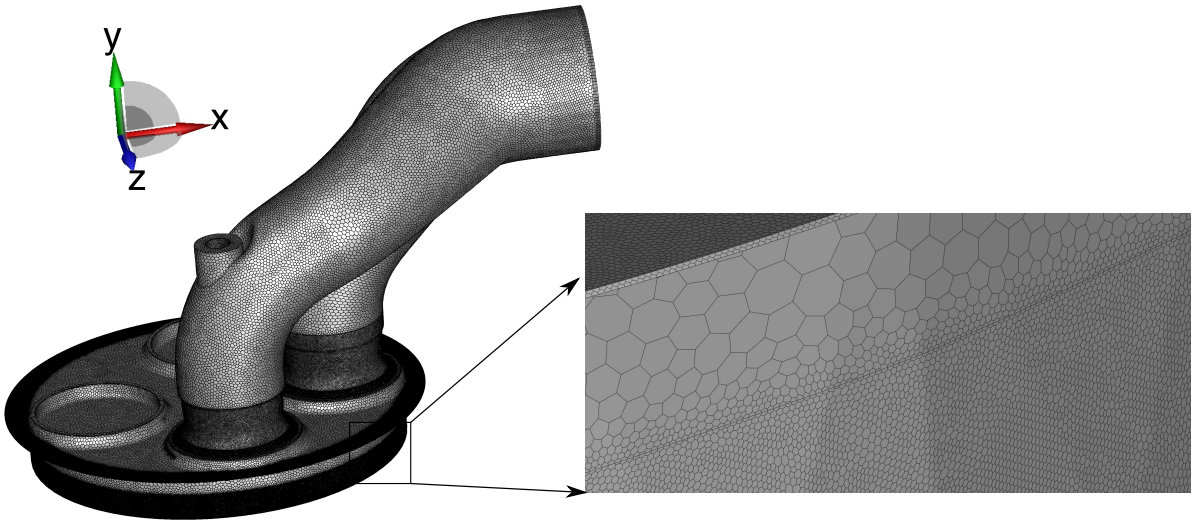

Figure 3.6: Computational mesh of the engine and exhaust manifolds during the exhaust stroke

Table 3.3: Simulation cases specifications

-	case FL	case PL
Mean effective pressure MEP (bar)	14.95	8.01
ϕ_{CH_4-air} (-)	0.5464	0.5184
Injected pilot diesel volume (mm^3)	38.5	52.5
start of injection SOI (°CA)	327	327
injection period (ms)	1.0	1.28
ratio of n-heptane to methane mass	0.01	0.0214
Temperature T_{ini} (K)	583	578
Pressure p_{ini} (bar)	18.58	12.138
Turbulent kinetics energy k_{ini} (m^2/s^2)	25	25
Turbulent dissipation rate ϵ_{ini}(m^2/s^3)	10000	10000

omization of the spray was modeled using the WAVE break up model of Reitz [90]. Further information can be found in [91]. The Dukowicz model [92] was chosen for evaporation and the corresponding heat and mass transfer.

3.9 Results of the Combustion Simulations

This section presents the simulation results for cases FL and PL. Figure 3.7 shows the spatial distribution of the equivalence ratio ϕ and combustion progress variable c at 355 °CA for case PL in different views. The asymmetrical distribution of injected fuel was due to the eccentrical position of the pilot injector. From the evolution of the progress variable it can be seen that the ignition and the flame front initiation started in the zones of high equivalence ratios where n-heptane existed. Figure 3.8 shows the mean temperature and mean heat release rate evolution over the crank angle for the two cases. The experimental results were determined indirectly through pressure measurements. The turbulent stretch factor α_0 in the combustion model was set to 1.6 for both cases. The ignition prefactors in equation 3.46 were set to 1.1 and 1.4 for case FL and case PL, respectively. The maximum heat release rate in case PL is accurately predicted. However, the center of heat release is slightly delayed with respect to the experiment. The predicted maximum mean temperature is around 70 K higher than the experiment. In case FL, the simulated maximum of heat release rate is underestimated compared to experiment.
Despite the slightly deviations with the experimental results, the adapted ECFM3Z model with the tabulated auto-ignition delay times and laminar flame speeds delivers satisfactory results, which can be used for the further calculation of the emissions described in chapter 5.

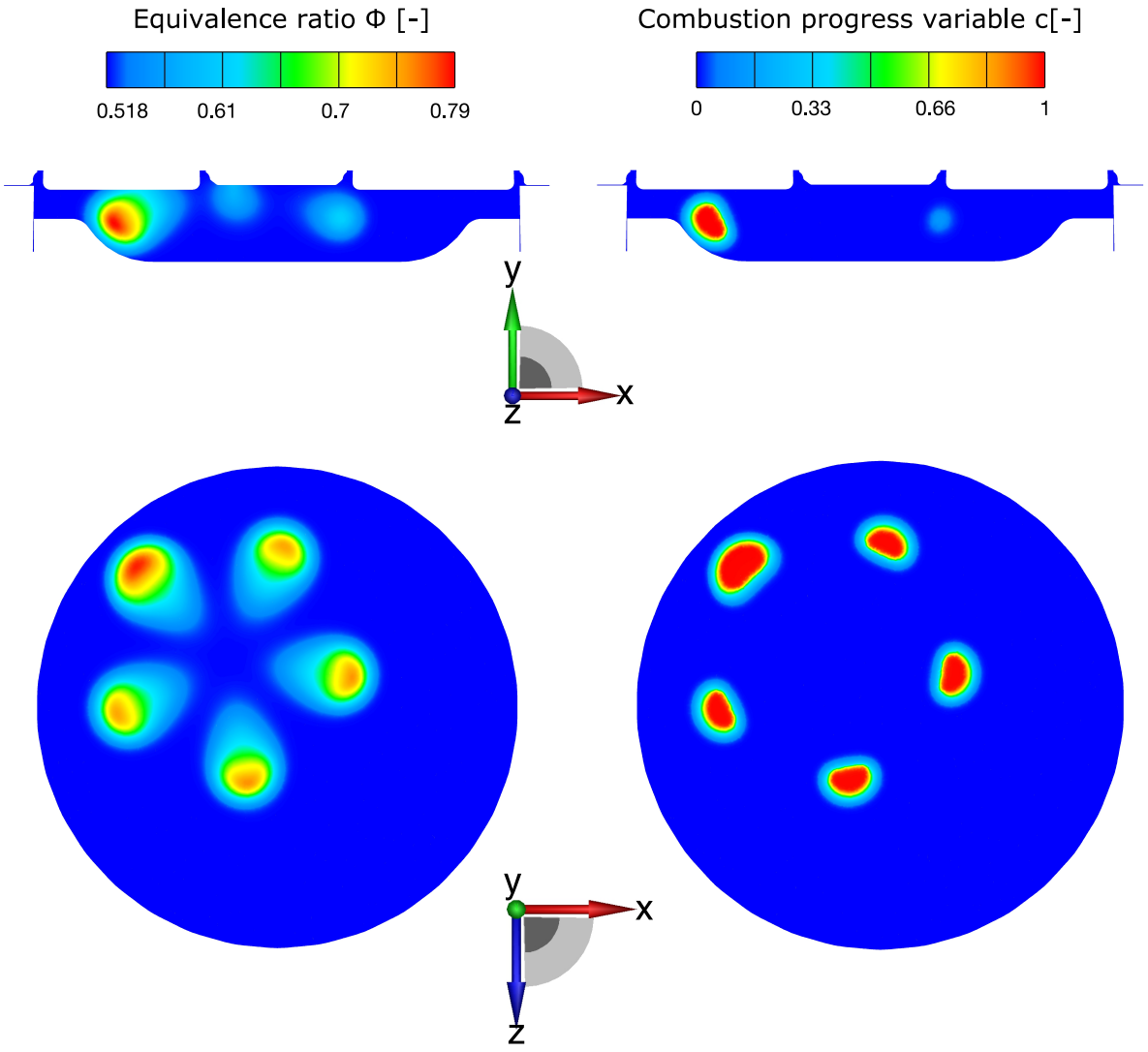

Figure 3.7: Spatial distribution of the equivalence ratio ϕ and combustion progress variable $\widetilde{c}$ at 355 °CA for case PL on the cut surfaces through the simulated domain with closed valves sketched in the upper left part of figure 3.5; upper part: cut surface perpendicular to the z axis through the center point (0, 0, 0); lower part: cut surface perpendicular to the y axis through the point (0, -0.02 m, 0)

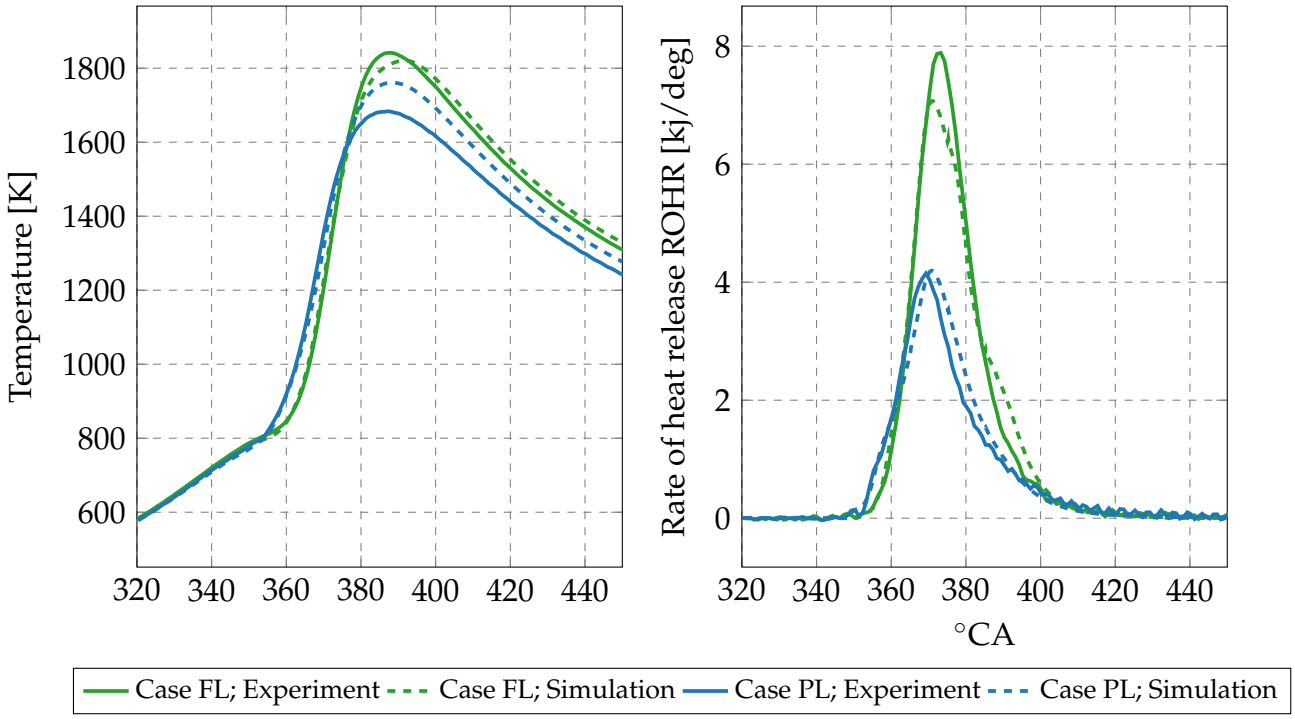

Figure 3.8: Measured and simulated mean temperature (left) and rate of heat release rate (right)

4 Modeling of Pollutant Formation and Conversion

The kinetics calculations conducted in Section 2.2 showed that high levels of NO_2 are reached when unburned CH_4, which has survived bulk combustion, is mixed and diluted with the product gas containing NO and excess O_2. Depending on the mixture composition and temperature, the remained unburned CH_4 can undergo further oxidation, which is termed as post-oxidation. It was shown that the post-oxidation of CH_4 is accompanied by NO_2 formation, which varies depending on temperature and mixture composition.

To predict the NO_2 formation in CFD, an accurate prediction of NO mass fractions as well as unburned CH_4, which survives bulk combustion are required. In Section 4.1 the mechanisms of NO formation and the employed approach for the NO modeling in CFD are described. Section 4.2 concerns the modeling of unburned CH_4, which survived bulk combustion. One approach for computing the post-oxidation of the unburned CH_4 in CFD, would be to couple a detailed kinetic mechanism with CFD calculations, which is not an efficient approach. To compute the post-oxidation efficiently, a low order model based on the tabulation method is proposed in this work, which is described in Section 4.3. Post-oxidation of CH_4 is accompanied by CO formation as well as NO to NO_2 conversion as depicted in Section 2.2. The proposed look-up table method is also utilized for predicting the conversion of NO to NO_2 and vice versa as well as CO formation and conversion, which are also described in Section 4.3. This approach is based on computing the conversion rates through simulations using the homogeneous reactor model in Cantera. The Rasmussen, Sivaramakrishnan and Gri 3.0 kinetic mechanisms were employed for reactor calculations. The calculated conversion rates were stored among others with respect to appropriate progress variables, which are described in Section 4.3. Three look-up tables corresponding to the aforementioned kinetic mechanisms were generated. The a priori generated look-up tables were then used in the CFD calculations.

4.1 Modeling NO Formation

In general, three main sources are responsible for NO formation:

- Thermal NO as a result of the dissociation of N_2 in the air [93,94];
- Prompt NO, also known as Fenimore NO, formed by the interaction between fuel and the N_2 component of air [93];
- NO formed from the nitrogen containing components available in the fuel.

The last NO source is negligible for the investigated lean diesel-NG DF engine, due to the low amounts of fuel-bond nitrogen (FBN) in diesel as well as small amounts of injected diesel. The mechanism of prompt NO formation, also known as the Fenimore mechanism [95], is important at low temperatures (below 1000 K), for fuel-rich mixtures and short residence times [95]. For the investigated DF engine with a small amount of diesel diluted in the lean background mixture of NG-air, the Fenimore mechanism is negligible. As reported by various authors, the proportion of produced Fenimore NO is smaller than < 5 %, and thus, it plays no dominant role compared with thermal NO formation [22,96]. In the considered engine application, NO formation is mainly driven in the burned gases by temperature levels of T >1800 K. The temperature of earlier burned gases rises due to the pressure rise during the progressing combustion. Higher residence times at higher temperature levels as well as excess oxygen augments the final NO concentration. This thermal NO formation is the dominant mechanism. The so-called extended Zeldovich mechanism models thermal NO formation through the following reaction paths:

$$\begin{aligned} N_2 + O &\underset{k_b}{\overset{k_f}{\rightleftharpoons}} NO + N \\ N + O_2 &\underset{k_b}{\overset{k_f}{\rightleftharpoons}} NO + O \\ N + OH &\underset{k_b}{\overset{k_f}{\rightleftharpoons}} NO + H \end{aligned} \tag{4.1}$$

The first reaction is the rate-limiting step, as the decomposition of the stable triple bond of molecular nitrogen requires a high activation energy. Accordingly, this reaction rate and thus NO formation is significant only

at high temperatures. Using the reactions in 4.1, the production rate of NO ($\dot{\omega}_{NO}$) can be formulated in terms of the law of mass action as follows:

$$\begin{aligned}\dot{\omega}_{NO} =& M_{NO}(k_{1f}c_O c_{N_2} + k_{2f}c_N c_{O_2} + k_{3f}c_N c_{OH} \\ & - k_{1b}c_{NO}c_N - k_{2b}c_{NO}c_O - k_{3b}c_{NO}c_H)\end{aligned} \tag{4.2}$$

where c_i is the concentration of the species and M_{NO} is the molar mass of NO. Equation 4.2 requires the radical concentrations of O, H, OH, and N in addition to O_2 and N_2. One strategy for their prediction is detailed kinetic calculations. However, employing the complex kinetic mechanisms for 3D turbulent engine flows is impractical. This problem can be overcome by calculating the radicals concentrations in their equilibrium states. The assumption can be justified, since the NO formation rate is much slower than the fuel oxidation rate, so that the thermal NO formation in the post-flame zone dominates.

In the context of the ECFM3Z model, the radical concentrations are calculated using the following equilibrium reactions [97]:

$$\begin{aligned}\mathrm{N_2} &\rightleftharpoons 2\mathrm{N} \\ \mathrm{O_2} &\rightleftharpoons 2\mathrm{O} \\ \mathrm{H_2} &\rightleftharpoons 2\mathrm{H} \\ \mathrm{O_2} + \mathrm{H_2} &\rightleftharpoons 2\mathrm{OH} \\ \mathrm{O_2} + 2\mathrm{H_2O} &\rightleftharpoons 4\mathrm{OH}\end{aligned} \tag{4.3}$$

The equilibrium constant for each reaction is calculated using

$$\mathrm{K}^{\mathrm{r}}_{eq} = \exp(\mathrm{A_r} \ln \mathrm{T_A} + \mathrm{B_r}/\mathrm{T_A} + \mathrm{C_r} + \mathrm{D_r}\mathrm{T_A} + \mathrm{E_r}\mathrm{T_A^2}) \tag{4.4}$$

where $\mathrm{T_A} = \mathrm{T}/1000[\mathrm{K}]$ and $\mathrm{A_r}$ to $\mathrm{E_r}$ are constants for each reaction r. An equation system is solved by employing the Newton-Raphson iteration method to predict eight species concentrations in equilibrium reaction steps 4.3. The equation system includes five equations from the equilibrium reaction steps 4.3. Additionally, three equations are required in order to calculate these eight concentrations. These equations are the element conversation relations of O, H, and N atoms. The equation system is solved for the burned gas temperature and burned gas mass fractions

according to the conditional averaged method in the ECFM3Z model as described in the previous chapter.

The NO formation rate's dependency on temperature is highly non-linear. Thus, using the time-averaged temperature for non-premixed/partially premixed diesel combustion leads to inaccurate predictions of the NO formation rate. The effect of turbulent fluctuations on the NO formation rate can be taken into account by employing the probability density function (PDF) technique [98]. The mean turbulent NO formation rate can be formulated as follows:

$$\overline{\dot{\omega}}_{\mathrm{NO}} = \int \dot{\omega}_{\mathrm{NO}}\left(T\right) P\left(T\right) dT \tag{4.5}$$

where $\overline{\dot{\omega}}_{\mathrm{NO}}$ is the mean turbulent rate of NO production, $\dot{\omega}_{NO}$ refers to the instantaneous NO formation rate from equation 4.2, and $P(T)$ refers to the PDF of the normalized temperature. It is assumed that a second-moment beta function is a suitable shape for the PDF, which is characterized by two parameters α and β. These values depend on the mean value of the temperature from combustion and its variance $\overline{\sigma^2}$ as the measure for the temperature fluctuations, which is determined by solving the transport equation:

$$\frac{\partial(\rho\overline{\sigma^2})}{\partial t} + \frac{\partial}{\partial x_j}\left(\rho u_j \overline{\sigma^2}\right) = \frac{\partial}{\partial x_j}\left(\frac{\mu_t}{\sigma_t}\frac{\partial\overline{\sigma^2}}{\partial x_j}\right) + C_g\mu_t\left(\frac{\partial\overline{T}}{\partial x_j}\right)^2 - C_d\rho\frac{\varepsilon}{k}\overline{\sigma^2} \tag{4.6}$$

where σ_t , C_g, and C are model constants with values of 0.85, 2.86 and 2.0, respectively. Further details regarding the implementation of the beta PDF model can be found in [99].

4.2 Modeling Unburned CH_4

There are several sources for the engine-out unburned hydrocarbon emissions [2]:

- Flame-wall quenching
- Combustion chamber crevice volumes
- Absorption and desorption of fuel in the oil film
- Exhaust leakage

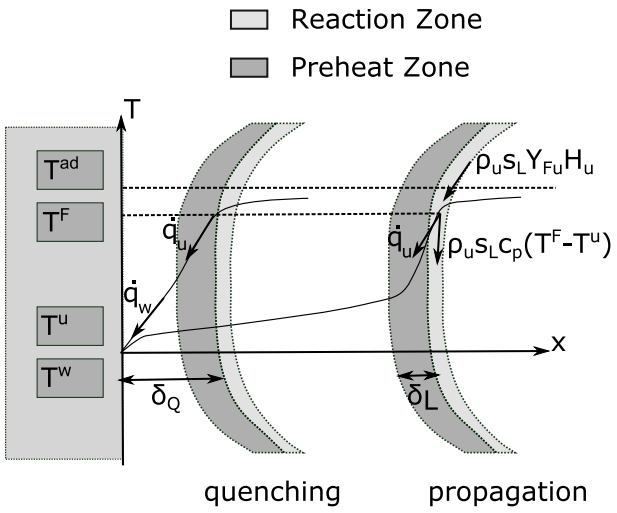

Figure 4.1: Concept of the head-on quenching model proposed by Boust et. al. [100]

In the present work, the first two sources were considered and are now discussed.

The flame-wall quenching is the result of flame heat loss as it approaches engine walls. Boust et al. [100] proposed the so-called thermal approach for the flame-wall interaction in the case of head-on quenching, meaning that the flame approaches the wall perpendicularly. The model depends strongly on the unburned mixture temperature profile normal to the wall. The concept of the thermal quenching is illustrated in Figure 4.1. Considering the control volume, which consists of the reaction zone and preheat zone, the heat release rate in stoichiometric or lean mixtures due to combustion $\dot{q}_\Sigma = \rho_u s_L Y_{Fu} H_U$ is distributed between the thermal energy in the reaction zone $\rho_u s_L c_p (T^F - T^u)$ and the thermal energy exchanged with the unburned mixture $\dot{q}_u$. ρ_u refers to the density of the unburned mixture, Y_{Fu} and H_U correspond to the fuel mass fraction and the fuel lower heating value, respectively. T^F and T^u refer to the flame temperature and the temperature of the unburned mixture, respectively. When the quenching occurs, the heat loss at the wall $\dot{q}_w$ equals the heat transfer from the reaction zone into the unburned mixture $\dot{q}_u$:

$$\dot{q}_w = \dot{q}_u \tag{4.7}$$

According to the thermal model, the temperature profile in the quenched mixture rises linearly from the wall temperature T^w upto the flame temperature T^F, implying that the heat flux inside the quenched zone remains constant, leading to:

$$\lambda \frac{\partial T}{\partial x}\bigg|_{x=0} = \lambda \frac{\partial T}{\partial x}\bigg|_{x=\delta_Q} \tag{4.8}$$

Thus $\dot{q}_w$, due to conductive heat flux in the unburned quenched mixture can be formulated as follows:

$$\dot{q}_w = \frac{\lambda_Q (T^F - T^W)}{\delta_Q} \tag{4.9}$$

where λ_Q refers to the thermal conductivity in the quenched mixture and δ_Q refers to the quench distance.

In order to predict the maximum $\dot{q}_W$ in the context of URANS simulations small time steps are required, which lead to high computational time. In order to overcome this problem, a dimensionless wall heat flux φ_Q is introduced:

$$\varphi_Q = \frac{\dot{q}_w}{\dot{q}_\Sigma} \tag{4.10}$$

which defines the maximum wall heat flux normalized to the flame power $\dot{q}_\Sigma = \rho_u s_L Y_{Fu} H_U$. Thus the equation 4.9 can be rewritten as

$$\delta_Q = \frac{\lambda_Q \left(T^F - T^W\right)}{\varphi_Q Y_{Fu} H_U s_L \rho_u} \tag{4.11}$$

The measurements of Labuda et al. [101] resulted in φ_Q=0.2 for pressures varied between 2 and 15 MPa. Sotten et al. [102] suggested φ_Q= 0.2 to 0.3 for pressures upto 1.7 MPa. Vosen et al. suggested φ_Q= 0.3 to 0.35 [103] and Lu et al. proposed φ_Q=0.3 to 0.4 [104] for atmospheric pressures.

In the present work, equation 4.11 was implemented in AVL-Fire. The implementation was conducted according to Kuppa's work concerning the numerical modeling of quenching in gas engines [57]. The dimensionless number φ_Q was set to 0.2 according to the measurements conducted by Labuda et al. [101]. It is assumed that the quenching can occur when the combustion progress variable $\widetilde{c}$ defined in equation 3.36 becomes higher than 0.1 in the wall boundary cell ($\widetilde{c} > 0.1$). As soon as the criterion $\widetilde{c} > 0.1$ in a wall boundary cell is fulfilled, equation 4.11 is eval-

uated for the respective cell. This assumption is corrected depending on the calculated quench distance, which is described in the following. The gas properties, namely λ_Q, ρ_u and s_L in the quenched layer are evaluated at the unburned fresh gas temperature T^u in the context of the ECFM3Z model described previously. T^F refers to the temperature in the cell center. Y_{Fu} and H_U refer to the mass fraction of CH_4 and it's lower heating value equals to 5.10^7 J/kg. It is assumed that the wall boundary cell contains only methane and air.

Following the calculation of the quench distance, the local mass fraction of the quenched mixture in each computational cell is evaluated by using

$$Y_Q = (\rho_u \cdot \delta_Q) / (\rho \cdot 2\Delta X) \tag{4.12}$$

where ΔX is the distance of the cell center to its wall boundary and ρ is the cell center density. In the next step, the unburned CH_4 mass fraction due to quenching is calculated using

$$Y_{CH_4,Q} = Y_Q \cdot Y_{TCH_4} \tag{4.13}$$

Y_{TCH_4} refers to the mass fraction of tracer fuel methane. By assuming only methane exists as fuel in the wall boundary cell, equation 4.13 can be related to the progress variable from equation 3.36:

$$Y_Q = 1 - c \tag{4.14}$$

If $Y_Q < (1 - c)$, the assumption for quenching is not fulfilled and thus the previous procedure is repeated for the next time step until the criterion $Y_Q \geq (1 - c)$ is achieved. Following this, the scalar variables $Y_{TCH_4,Q}$ and $Y_{CH_4,Q}$ are initialized with the unburned CH_4 mass fraction from equation 4.13 in each cell and transported by

$$\frac{\partial \overline{\rho}\widetilde{Y}}{\partial t} + \frac{\partial \overline{\rho}\widetilde{u}_i\widetilde{Y}}{\partial x_i} = \frac{\partial}{\partial x_i}\left(\left(\frac{\mu}{Sc} + \frac{\mu_t}{Sc_t}\right)\frac{\partial \widetilde{Y}}{\partial x_i}\right) + \overline{\rho}\widetilde{\dot{\omega}} \tag{4.15}$$

$Y_{TCH_4,Q}$ is defined as the tracer of the unburned CH_4 for which the source term $\dot{\omega}$ equals zero, whereas $Y_{CH_4,Q}$ can undergo post-oxidation. The source term $\dot{\omega}$, as the oxidation source term, is evaluated using the look-up tables discussed in Section 4.3.

The crevices are another source of unburned hydrocarbon emissions [3]. Crevices are narrow regions into which the flame can not propagate due to the high heat losses to the walls [105]. During combustion and pressure rise in the cylinder, the unburned mixture flows into the crevice volumes. During the expansion when the pressure in the cylinder drops, the compressed charge in the crevice volume flows back into the cylinder.

In this thesis, the crevice regions were included in the computational mesh. The transport scalars $Y_{TCH_4,Q}$ and $Y_{CH_4,Q}$ are initialized in these regions with the available CH_4 when the cylinder mean pressure starts falling. These are then transported according to equation 4.15 and can undergo post-oxidation, if the temperature is high enough.

4.3 Tabulation Method for Predicting CH_4 Post-oxidation, NO_2 and CO Formation and Conversion

The unburned CH_4 described in the previous section can undergo post-oxidation. The post-oxidation of CH_4 is accompanied by CO formation and the conversion of NO to NO_2. Employing detailed kinetic mechanisms for predicting post-oxidation of unburned CH_4, and CO, and NO_2 evolution in the 3D CFD calculations is highly time consuming. An efficient approach for modeling the aforementioned species evolution in CFD is proposed in this thesis based on the tabulation method. The idea of tabulated chemistry for predicting the combustion has been thoroughly developed and studied. For instance, the so-called intrinsic low-dimensional manifolds (ILDM) developed by Mass et. al. [106] parameterizes the composition of the reactive mixture along a small number of coordinates, which are stored in a look-up table for use in CFD calculations. Another approach for modeling combustion using look-up tables is the so-called FPI method (flame prolongation of ILDM) proposed in [107], which extends the feasibility of the ILDM method to the low temperature levels. In another study, Dulbecco [108] employed the tabulation method for modeling ignition and combustion in a diesel homogeneous charge compression ignition engine (HCCI). The species change rates were calculated using the 0D homogeneous constant volume reactor model and stored in a look-up table. According to the author's knowledge, however, the present tabulation method is a new approach, particularly for pre-

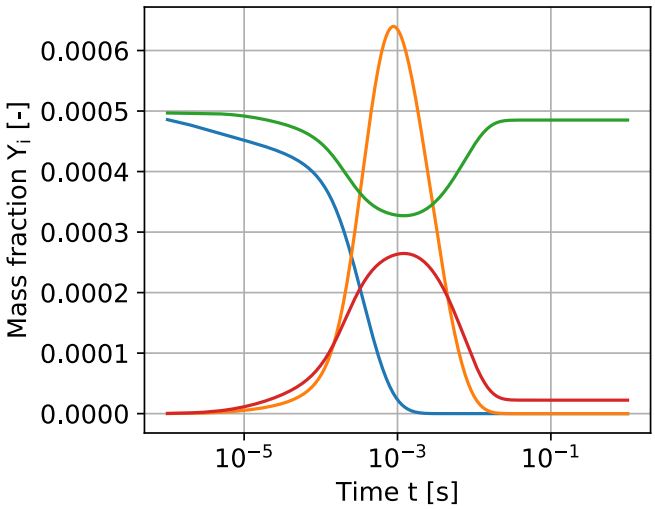

Figure 4.2: Evolution of CH_4 (——), CO (——), NO (——) and NO_2 (——) computed in homogeneous reactor employing the Rasmussen kinetic mechanism; Initial conditions: $Y_{TCH_4,Q}$=0.0005, Y_{TNO}=0.0005, Y_{OH}=5.e-6 in flue gas following methane-air combustion with ϕ=0.5, T=1300 K, p=20 bar

dicting NO_2 formation and conversion. In the present approach, the conversion rates of so-called progress variables, corresponding to CH_4, NO_2 and CO mass fractions were computed through simulations with the 0D homogeneous reactor model in Cantera. The Rasmussen, Sivaramakrishnan and Gri 3.0 kinetic mechanisms were employed for reactor calculations. The computed conversion rates were stored with respect to the corresponding progress variables among others. Three look-up tables corresponding to the aforementioned kinetic mechanisms were generated. During the CFD calculations, the conversion rates were retrieved from the look-up tables for each computational cell. Each computational cell was considered as the homogeneous reactor. The mass fractions of unburned CH_4 tracer ($Y_{TCH_4,Q}$) due to quenching and from crevices as well as NO tracer mass fraction (Y_{TNO}) varies in each computational cell. Y_{TNO} refers to mass fraction of tracer NO produced exclusively during combustion as described in Section 4.1 and does not include the possible NO to NO_2 conversion. $Y_{TCH_4,Q}$ and Y_{TNO} were used for defining appropriate progress variables. Using the homogeneous reactor model in Canter, referring to a single computational cell with the following arbitrary initial conditions, the proposed look-up table approach is described in the following. The initial mixture compositions are set to $Y_{TCH_4,Q}$=0.0005,

Y_{TNO}=0.0005, Y_{OH}=5.e-6. The burned gas mass fraction in the cell corresponds to the main products mass fractions following methane-air combustion with ϕ=0.5 (Y_{O_2}=0.1127). Initial temperature and pressure equal T=1300 K and p=20 bar. The species evolution of CH_4, CO, NO and NO_2 over time are calculated using the homogeneous reactor model in Cantera employing the kinetic mechanism of Rasmussen and plotted in Figure 4.2.

The species evolution can be expressed by defining appropriate progress variables. For CH_4 post-oxidation the dimensionless progress variable PV_{CH4} is defined as

$$PV_{CH4} = 1 - \frac{Y_{CH_4,Q}(t)}{Y_{TCH_4,Q}} \tag{4.16}$$

where $Y_{TCH_4,Q}$ is unburned CH_4 tracer and $Y_{CH_4,Q}$ is unburned CH_4 undergoing post-oxidation. $Y_{TCH_4,Q}$ can vary locally in CFD. The change rate of PV_{CH4} is coupled with that of CH_4 and given as:

$$\frac{dPV_{CH4}}{dt} = \dot{\omega}_{PV_{CH4}} = -\frac{1}{Y_{TCH_4,Q}} \frac{dY_{CH_4,Q}}{dt} \tag{4.17}$$

Like CH_4 post-oxidation, NO conversion to NO_2 can be tracked along an appropriate progress variable. $PV_{NO\rightarrow NO2}$ describes the time- dependent NO_2 mass fraction during NO_2 production normalized with the mass fraction Y_{TNO}:

$$PV_{NO\rightarrow NO2} = \frac{M_{NO}}{M_{NO_2}} \frac{Y_{NO_2}(t)}{Y_{TNO}} \tag{4.18}$$

where M_{NO} and M_{NO_2} are the molar masses of the species NO and NO_2, respectively. Y_{TNO} refers to the NO tracer mass fraction predicted exclusively during combustion described in Section 4.1 and can vary locally in CFD. This term does not include the NO to NO_2 conversion. The change rate is given as follows:

$$\frac{dPV_{NO\rightarrow NO2}}{dt} = \dot{\omega}_{PV_{NO\rightarrow NO2}} = \frac{M_{NO}}{M_{NO_2} Y_{TNO}} \frac{dY_{NO_2}}{dt} \tag{4.19}$$

In addition, the CO production can be traced along the progress variable $PV_{CO,pro}$ defined using

$$PV_{CO,pro} = \frac{M_{CH_4}}{M_{CO}} \frac{Y_{CO}(t)}{Y_{TCH_{4,Q}}} \tag{4.20}$$

with the change rate

$$\frac{dPV_{CO,pro}}{dt} = \dot{\omega}_{PV_{CO,pro}} = \frac{M_{CH_4}}{M_{CO} Y_{TCH_{4,Q}}} \frac{dY_{CO}}{dt} \tag{4.21}$$

where M_{CH_4} and M_{CO} refer to the molar masses of CH_4 and CO. As can be seen in Figure 4.2, depending on the mixture composition and the temperature/pressure, NO_2 reaches a certain maximum value $Y_{NO_{2,max}}$ at a certain time and starts converting back to NO as time progresses. The conversion of NO_2 back to NO can be tracked along the progress variable $PV_{NO2\rightarrow NO}$ defined as

$$PV_{NO2\rightarrow NO} = 1 - \frac{Y_{NO_2}(t)}{Y_{NO_{2,max}}} \tag{4.22}$$

with the change rate

$$\frac{dPV_{NO2\rightarrow NO}}{dt} = \dot{\omega}_{PV_{NO2\rightarrow NO}} = -\frac{1}{Y_{NO_{2,max}}} \frac{dY_{NO_2}}{dt} \tag{4.23}$$

where $Y_{NO_{2,max}}$ corresponds to the maximum NO_2 mass fraction. In analogy with NO_2, the CO mass fraction reaches its maximum value $Y_{CO_{max}}$ at a certain time and starts falling as time progresses. The CO mass fraction reduction can be tracked along the progress variable $PV_{CO,cons}$ defined by

$$PV_{CO,cons} = 1 - \frac{Y_{CO}(t)}{Y_{CO_{max}}} \tag{4.24}$$

with a change rate that equals to

$$\frac{dPV_{CO,cons}}{dt} = \dot{\omega}_{PV_{CO,cons}} = -\frac{1}{Y_{CO_{max}}} \frac{dY_{CO}}{dt} \tag{4.25}$$

where $Y_{CO_{max}}$ refers to the maximum CO mass fraction. The defined progress variables aim to define dimensionless variables, along which the species evolution can be tracked. Figure 4.3 shows the above-defined

progress variables together with their change rates for the case illustrated in Figure 4.2. The upper left part of the figure shows the time evolution

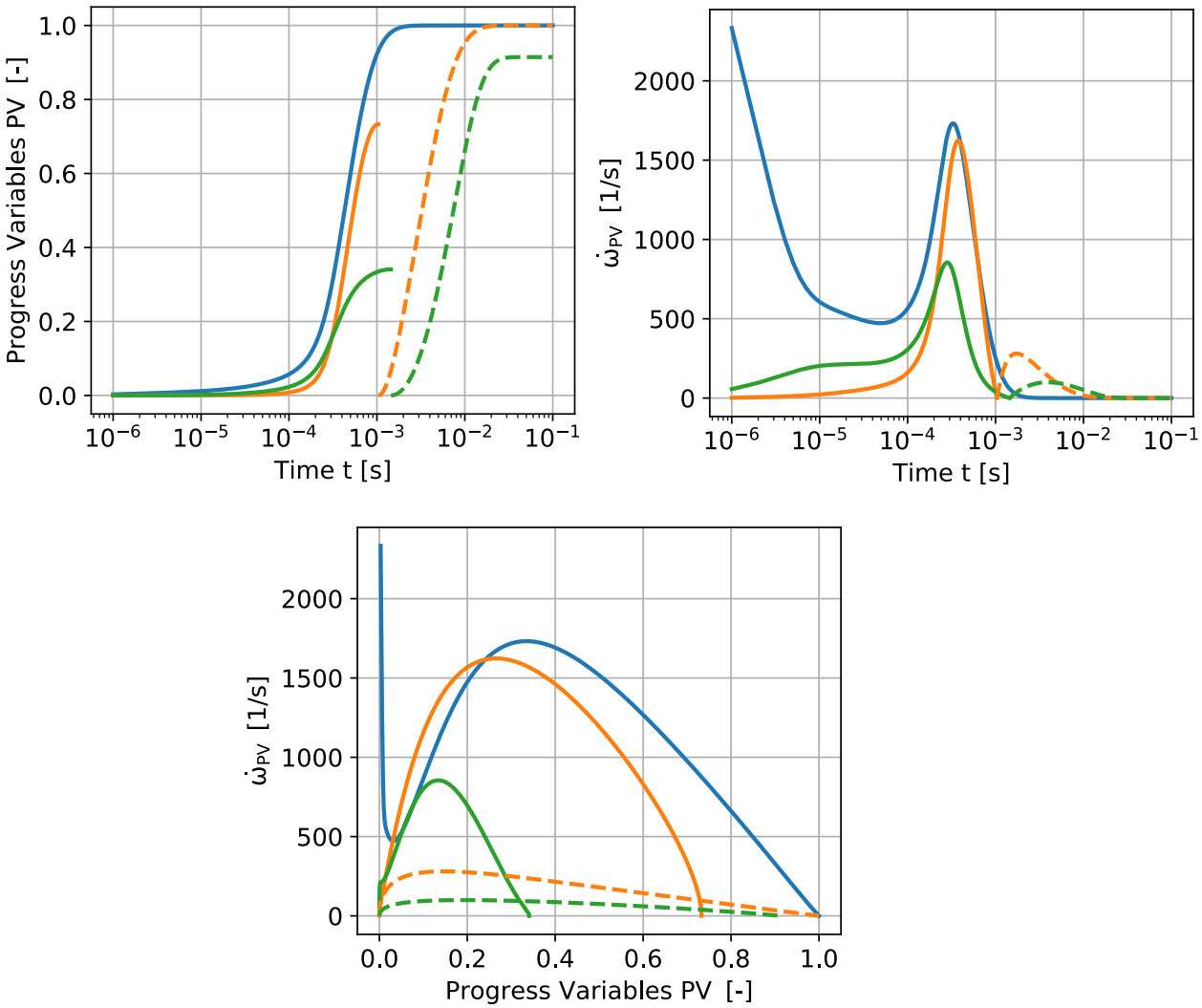

Figure 4.3: Evolution of progress variables and their change rates related to CH_4 oxidation (——), CO production (——), NO to NO_2 conversion (——), CO consumption(- - - -) and NO_2 to NO conversion (- - - -) over time; Initial conditions according to Figure 4.2

of the progress variables. PV_{CH4} reaches one as the CH_4 oxidation is completed. $PV_{CO,pro}$ as well as $PV_{NO\rightarrow NO2}$ rise with time. They track the CO production as well as NO to NO_2 conversion, respectively. When CO and NO_2 reach their maximum, $PV_{CO,cons}$ as well as $PV_{NO2\rightarrow NO}$ are initialized, which track the CO consumption and NO_2 to NO conversion, respectively. The change rates of the progress variables over time are plotted

in the upper right part of the figure. Finally, the lower part of the figure illustrates the change rates of the progress variables over the corresponding progress variables.

The basic idea behind the look-up table method is to compute the progress variables' change rates $\dot{\omega}_{PV_{CH4}}$, $\dot{\omega}_{PV_{NO\rightarrow NO2}}$, $\dot{\omega}_{PV_{CO,pro}}$, $\dot{\omega}_{PV_{NO2\rightarrow NO}}$ and $\dot{\omega}_{PV_{CO,cons}}$ in the homogeneous reactor in Cantera and to tabulate them among others with respect to the progress variables PV_{CH4}, $PV_{NO\rightarrow NO2}$, $PV_{CO,pro}$, $PV_{NO2\rightarrow NO}$, and $PV_{CO,cons}$, respectively. The discretizing of the progress variables (PVs) was performed with a step size of 0.01 for $0 \leq$ PV ≤ 0.1, followed by a step size of 0.05 for $0.1 <$ PV ≤ 1. The transitions of $PV_{NO\rightarrow NO2}$ to $PV_{NO2\rightarrow NO}$ and $PV_{CO,pro}$ to $PV_{CO,cons}$, where NO_2 /CO evolution starts to decrease, were determined by cut-off values $PV_{NO\rightarrow NO2}$ and $PV_{CO,pro}$. From Figure 4.2, for instance, it can be seen that the NO_2 mass fraction starts decreasing as $PV_{NO\rightarrow NO2}$ reaches 0.38, which can vary for different initial conditions. In the case of CO, oxidation occurs at $PV_{CO,pro}$ =0.72, which can also vary for different initial conditions.

The above-defined progress variables' change rates were computed in the homogeneous reactor in Cantera covering the occurring ranges of temperatures, pressures and initial compositions. The Rasmussen, Sivaramakrishnan and Gri 3.0 kinetic mechanisms were employed for the calculations. The initial CH_4 and NO mass fractions for reactor calculations spanned a range between 0.00 and 0.004 with a step size of 0.0002. Thus, the CH_4 oxidation in the absence of NO as well as NO to NO_2 conversion in the absence of CH_4 were also considered. The mass fractions of OH were set to 0, 10.E-6, and 100.0E-6. The mass fractions of O_2 and the other species were taken constant for all reactors calculations, namely Y_{O_2}=0.1127, Y_{CO_2}=0.0778, Y_{H_2O}=0.0636, and Y_{N_2}=0.745. These mass fractions correspond to the mass fractions of the main products following methane-air combustion with $\phi = 0.5$. The upper temperature limit of the table was set to T=1700 K, above which the NO_2 formation is suppressed. In addition the lower temperature limit was set to T=800 K, below which the CH_4 oxidation and thus the NO_2 formation are very low during the residence time relevant for the engines. The pressure as another dimension of the tables was set to p=1,5,10,20,40,60 and 100 bar.

The computed $\dot{\omega}_{PV_{CH4}}$, $\dot{\omega}_{PV_{NO\rightarrow NO2}}$, $\dot{\omega}_{PV_{CO,pro}}$, $\dot{\omega}_{PV_{NO2\rightarrow NO}}$, and $\dot{\omega}_{PV_{CO,cons}}$ were tabulated with respect to the above-mentioned temperatures, pressures, Y_{CH_4}, Y_{NO}, Y_{OH}, and the corresponding discretized PVs. Thus, three

6D look-up tables for conversion rates, corresponding to the Rasmussen, Sivaramkrishnan and Gri 3.0 kinetic mechanisms, were generated.

The transition point of $PV_{NO\rightarrow NO2}$ to $PV_{NO2\rightarrow NO}$ corresponding to the turning point of NO_2 evolution as well as $PV_{CO,pro}$ transition to $PV_{CO,cons}$ related to the turning point of CO evolution were defined by using cut-off values. These cut-off values correspond to $PV_{NO\rightarrow NO2}$ and $PV_{CO,pro}$, for which NO_2 or CO starts to fall. They were stored for the aforementioned temperatures, pressures, Y_{CH4}, Y_{NO}, and Y_{OH} for each aforementioned mechanism, leading to three 5D look-up tables of the cut-off values.

The feasibility of the tabulation method are studied as follows: In Figure 4.4 the species evolutions employing the detailed kinetic mechanism of Rasmussen are compared with those predicted using the look-up table generated with the kinetic mechanism of Rasmussen. The generic case is a reactor experiencing a temperature and pressure drop resembling the expansion stroke of an engine. The temperature and pressure evolution are given in the upper part of the figure. The mixture of CH_4-NO-OH and the main product gas following CH_4-air combustion with ϕ=0.5 is initialized at different times and thus under different temperatures and pressures during the expansion. Depending on the instance of initialization, the extent of NO_2 formation varies. Comparing the results of the detailed kinetics with those achieved using the look-up table, it can be seen that the tabulation method can reproduce the detailed kinetics calculations fairly well. The calculation of CH_4 post-oxidation, NO to NO_2 conversion, and CO production using the tabulation method is conducted through the explicit integration of the following equations:

$$\begin{aligned}
\frac{dY_{CH_4,Q}(t)}{dt} &= -\dot{\omega}_{PV_{CH4}} Y_{TCH_4,Q} \\
\frac{dY_{NO_2}(t)}{dt} &= \dot{\omega}_{PV_{NO\rightarrow NO2}} \frac{M_{NO_2} Y_{TNO}}{M_{NO}} \\
\frac{dY_{CO}(t)}{dt} &= \dot{\omega}_{PV_{CO,pro}} \frac{M_{CO} Y_{TCH_4,Q}}{M_{CH_4}} \\
\frac{dY_{NO}(t)}{dt} &= -\frac{dY_{NO_2}(t)}{dt} \frac{M_{NO}}{M_{NO_2}}
\end{aligned} \tag{4.26}$$

$\dot{\omega}_{PV_{CH4}}$, $\dot{\omega}_{PV_{NO\rightarrow NO2}}$, and $\dot{\omega}_{PV_{CO,pro}}$ are evaluated through the linear interpolation of conversion rates stored in the look-up table at the corresponding

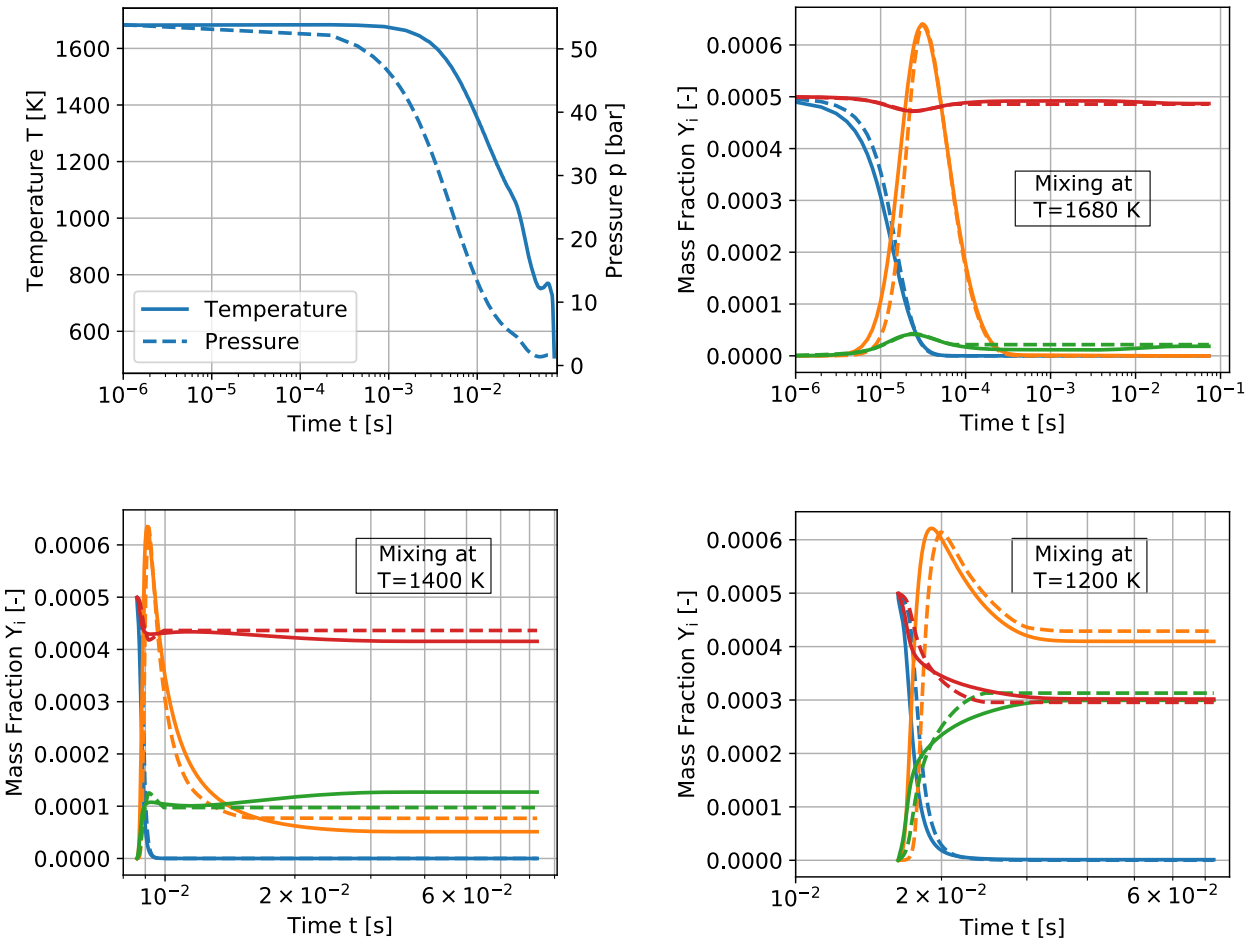

Figure 4.4: Effect of mixing temperature/pressure on CH_4 (——), CO (——), NO_2(——) and NO (——) evolution predicted using the detailed kinetic mechanism (——) and tabulation method (- - - - -); Initial mixture composition according to Figure 4.2

temperature, pressure, $Y_{TCH_4,Q}$, Y_{TNO}, Y_{OH} and PVs. At each time step, PV_{CH4}, $PV_{NO\rightarrow NO2}$, and $PV_{CO,pro}$ are updated according to equations 4.16, 4.18, and 4.20. In addition, at each time step, $PV_{NO\rightarrow NO2}$ and $PV_{CO,pro}$ cut-off values are retrieved from the 5D cut-off table through the linear interpolation of the table values at the corresponding temperature, pressure, $Y_{TCH_4,Q}$, Y_{TNO}, and Y_{OH}. When $PV_{NO\rightarrow NO2}$ or $PV_{CO,pro}$ evaluated from equations 4.18 and 4.20 exceeds the tabulated cut-off values, the corresponding species start falling. In this case, the change rates of NO_2 or CO are not longer calculated using equation 4.26. The NO_2 conversion back

to NO as well as CO oxidation to CO_2 are then calculated through the explicit integration of

$$\begin{aligned} \frac{dY_{NO_2}(t)}{dt} &= -\dot{\omega}_{PV_{NO2\rightarrow NO}} Y_{NO_{2,max}} \\ \frac{dY_{CO}(t)}{dt} &= -\dot{\omega}_{PV_{CO,cons}} Y_{CO_{max}} \end{aligned} \tag{4.27}$$

where $Y_{NO_{2,max}}$ and $Y_{CO_{max}}$ are the mass fractions of NO_2 and CO calculated from equations 4.26 at the instant of transition.

In the present study, for each kinetic mechanism, namely for the Rasmussen, Sivaramakrishnan and Gri 3.0 kinetic mechanisms, two look-up tables were generated, namely one for the conversion rates corresponding to CH_4 post-oxidation as well as CO and NO_2 formation/consumption rates and one table for the cut-off values, at which the produced NO_2 and CO species start converting to NO and CO_2, respectively.

The procedure for predicting CH_4 post-oxidation, NO_2, NO, and CO evolution in the context of the CFD simulation in each computational cell by using the look-up tables corresponding to each kinetic mechanism is the same as that described for the generic case. At each time step and for each computational cell, the tabulated conversion rates corresponding to each kinetic mechanism were retrieved from the corresponding look-up table depending on the cell's temperature, pressure, $Y_{TCH_4,Q}$, Y_{TNO}, and Y_{OH} and corresponding PVs. In addition, the tabulated cut-off values corresponding to each kinetic mechanism were retrieved with respect to the cell's temperature, pressure, $Y_{TCH_4,Q}$, Y_{TNO}, and Y_{OH}. Y_{TNO} and Y_{OH} are the mass fractions of NO and OH predicted in the framework of ECFM3Z model and described in Section 4.1.

The a priori generated look up tables are used in CFD calculations for predicting the pollutants formation and conversion for the two operation points FL and PL presented in Section 3.9. The results are discussed in the next section.

5 Results of the Pollutant Formation and Conversion Simulations

In this chapter the simulated unburned CH_4 mass fractions without and with post-oxidation and the CO, NO and NO_2 mass fractions in the engine and in the exhaust duct are presented. The left part of the Figure 5.1 presents a sketch of the simulated engine with the exhaust manifold and the location, where the time-dependent and area-averaged species mass fractions exiting the engine were evaluated in CFD. The right part of Figure 5.1 depicts the exhaust duct and the measurement points of the species mass fractions, namely FTIR-HP and further downstream in the exhaust duct FTIR-LP.

In Section 5.1, the spatial distribution and time evolution of unburned CH_4 with and without post-oxidation, CO, NO, and NO_2 mass fractions in the engine for FL and PL operation points, validated regarding combustion in Section 3.9, are presented. These mass fractions are computed by employing look-up tables generated with the kinetic mechanisms of Rasmussen, Sivaramakrishnan and Gri 3.0 described in Section 4.3.

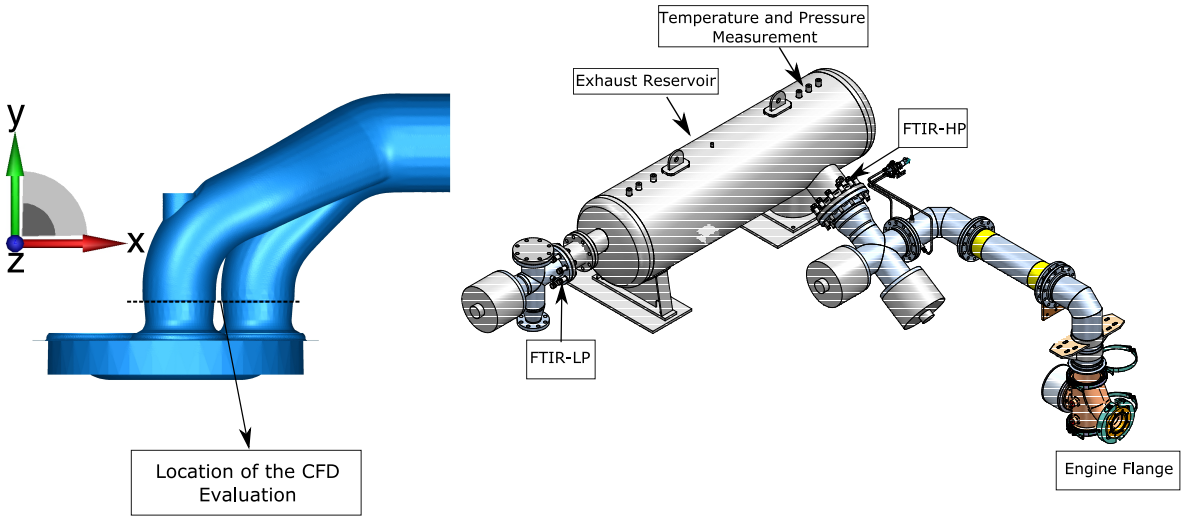

Figure 5.1: Sketch of the engine simulated in CFD (left) and the exhaust duct (right)

Using the time-dependent and area-averaged species mass fractions close to the engine exit, the evolution of the species up to FTIR-HP measuring point for the two cases FL and PL are evaluated and compared with the measurements in Section 5.2. This is achieved by using homogeneous reactor calculations in Cantera.

In Section 5.3, the species evolution from the FTIR-HP up to the FTIR-LP measuring point, are calculated for FL, PL and several other operation points by using homogeneous reactors in Cantera. Thus, the effect of high residence times in the exhaust duct on NO_2 formation and the performance of different kinetic mechanisms in reproducing the measurements are studied.

5.1 In-Cylinder Pollutant Formation and Conversion

In this section, the spatial distributions and time evolution of the unburned CH_4, CO, NO and NO_2 mass fractions in the engine for full load (FL) and partial load (PL) operation points are presented. Figure 5.2 shows the evolution of averaged $Y_{TCH_4,Q}$ as well as $Y_{CH_4,Q}$ for case FL over the crank angle. The crank angle axis spans the start of the simulation

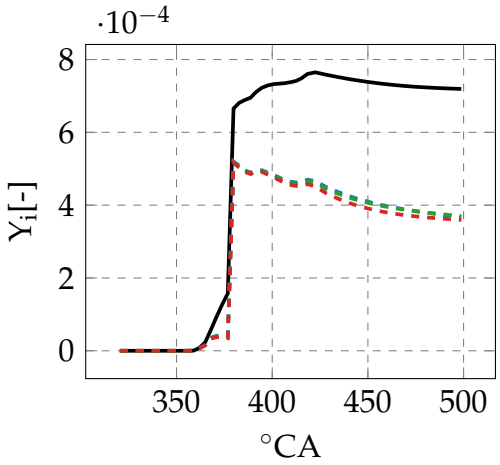

Figure 5.2: Evolution of the unburned CH_4 tracer $Y_{TCH_4,Q}$ (——) and $Y_{CH_4,Q}$ (- - - - -) undergoing post-oxidation for case FL computed by using the look-up tables generated with the kinetic mechanisms of Rasmussen (——), Sivaramakrishnan (——) and Gri 3.0 (——)

until the exhaust valves open at 499 °CA. $Y_{TCH_4,Q}$ refers to the quenched CH_4 on walls and CH_4 trapped in crevice regions without post-oxidation,

whereas $Y_{CH_4,Q}$ takes the post-oxidation of the unburned CH_4 by using the look-up tables into account as well. The post-oxidation was computed using the look-up tables generated by employing the Rasmussen, Sivaramakrishnan and Gri 3.0 kinetic mechanisms, described in Section 4.3. At

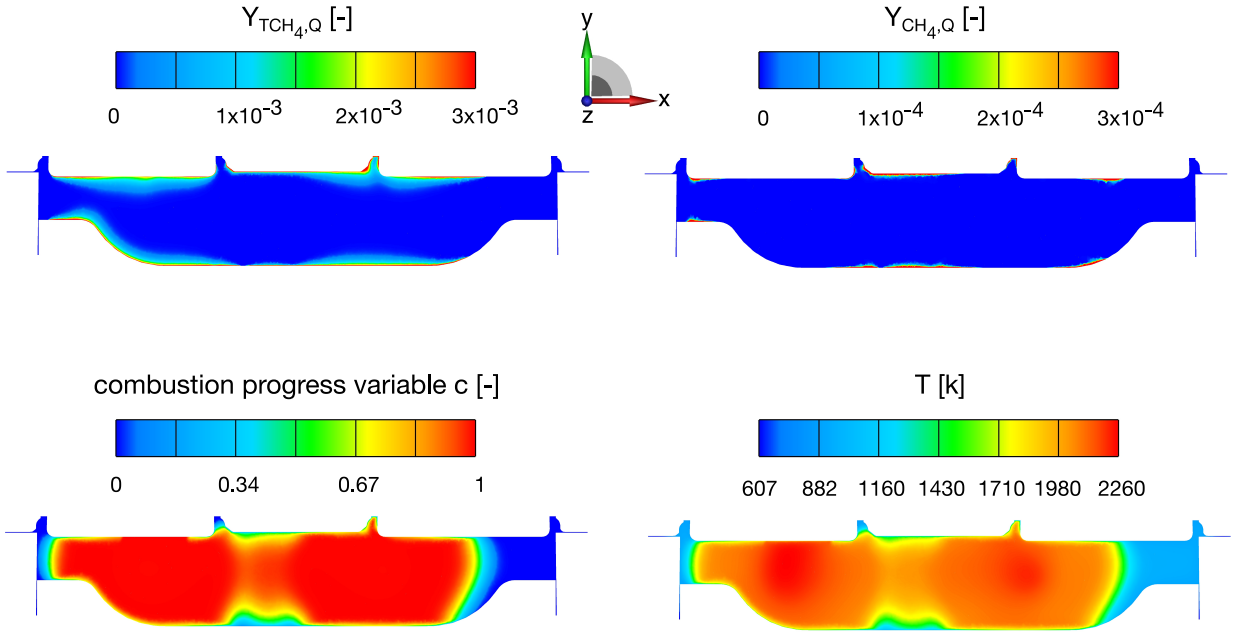

Figure 5.3: Distribution of $Y_{TCH_4,Q}$ and $Y_{CH_4,Q}$ computed by using the look-up table generated with the kinetic mechanism of Rasmussen (upper part); distribution of combustion progress variable $\widetilde{c}$ and temperature (lower part); at 375°CA for case FL on the cut surface perpendicular to the z axis through the center point (0, 0, 0) according to the upper part of figure 3.5

the earlier crank angles the scalars $Y_{TCH_4,Q}$ and $Y_{CH_4,Q}$ refer merely to the quenched CH_4 mass fractions according to flame-wall quenching as the flame front approaches the wall ($\widetilde{c} > 0.1$). Figure 5.3 shows the spatial distributions of $Y_{TCH_4,Q}$ and $Y_{CH_4,Q}$ together with the combustion progress variable and temperature field for case FL at 375 °CA, where $Y_{CH_4,Q}$ distribution corresponds to the result of post-oxidation, computed by using the look-up table generated with the Rasmussen kinetic mechanism. It can be seen that the quenched CH_4 decays fast due to post-oxidation at high temperatures. As soon as the in-cylinder pressure drops, $Y_{TCH_4,Q}$ and $Y_{CH_4,Q}$ are initialized in the crevice regions with the CH_4 mass fractions trapped in these zones. This can be observed as a steep rise in Figure 5.2. Figure 5.4 shows the distributions of both scalars for case FL at 430 °CA. The temperature for the post-oxidation is the one predicted by CFD with the ECFM3Z model. From the evolution of the scalars $Y_{TCH_4,Q}$ and $Y_{CH_4,Q}$,

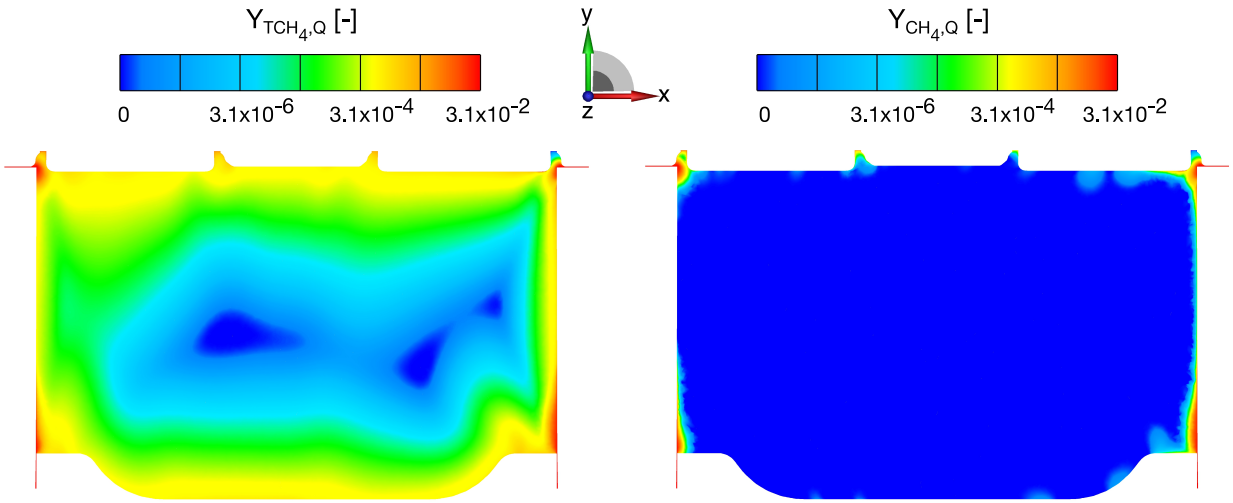

Figure 5.4: Distribution of $Y_{TCH_4,Q}$ and $Y_{CH_4,Q}$ computed by using the look-up table generated with the kinetic mechanism of Rasmussen, for case FL at 430°CA on the cut surface perpendicular to the z axis through the center point (0, 0, 0) according to the upper part of figure 3.5

it can be seen that flame-wall quenching at the earlier crank angle is accompanied by the fast post-oxidation of CH_4, whereas the post-oxidation of the unburned discharged CH_4 from crevice regions undergoes slower oxidation as temperature decreases for larger crank angles.

Figure 5.5 shows the mean evolution of NO_2, NO and CO mass fractions for case FL over the crank angle. For predicting Y_{NO_2}, it is differentiated between NO_2 formed in the presence of NO and O_2 ($Y_{NO_2,A}$) and NO_2 formed in the presence of CH_4, NO and O_2, namely $Y_{NO_2,B}$. The prediction of NO_2 mass fractions using look-up tables in the zones without any unburned CH_4 was possible, since the progress variable change rates corresponding to NO_2 formation rates ($\dot{\omega}_{PV_{NO\rightarrow NO2}}$) were also computed and tabulated for the mixture compositions without any CH_4 ($Y_{TCH_4,Q}$=0). To predict each ($Y_{NO_2,A}$), one scalar was defined with the source term retrieved from the respective look-up table. It can be seen that the NO_2 mass fraction in the absence of CH_4, ($Y_{NO_2,A}$) rises during the NO formation. The Rasmussen mechanism predicts slightly lower values than the Sivaramakrishnan and the Gri 3.0 kinetic mechanisms. The ratios of NO_2 to NO mass fraction at 499 °CA predicted by the look-up tables generated with the Rasmussen, Sivaramakrishnan and Gri 3.0 kinetic mechanisms are 3.3%, 3.5% and 3.4%, respectively. The NO evolutions, also depicted in Figure 5.5, include NO production as well as its conversion to NO_2 in

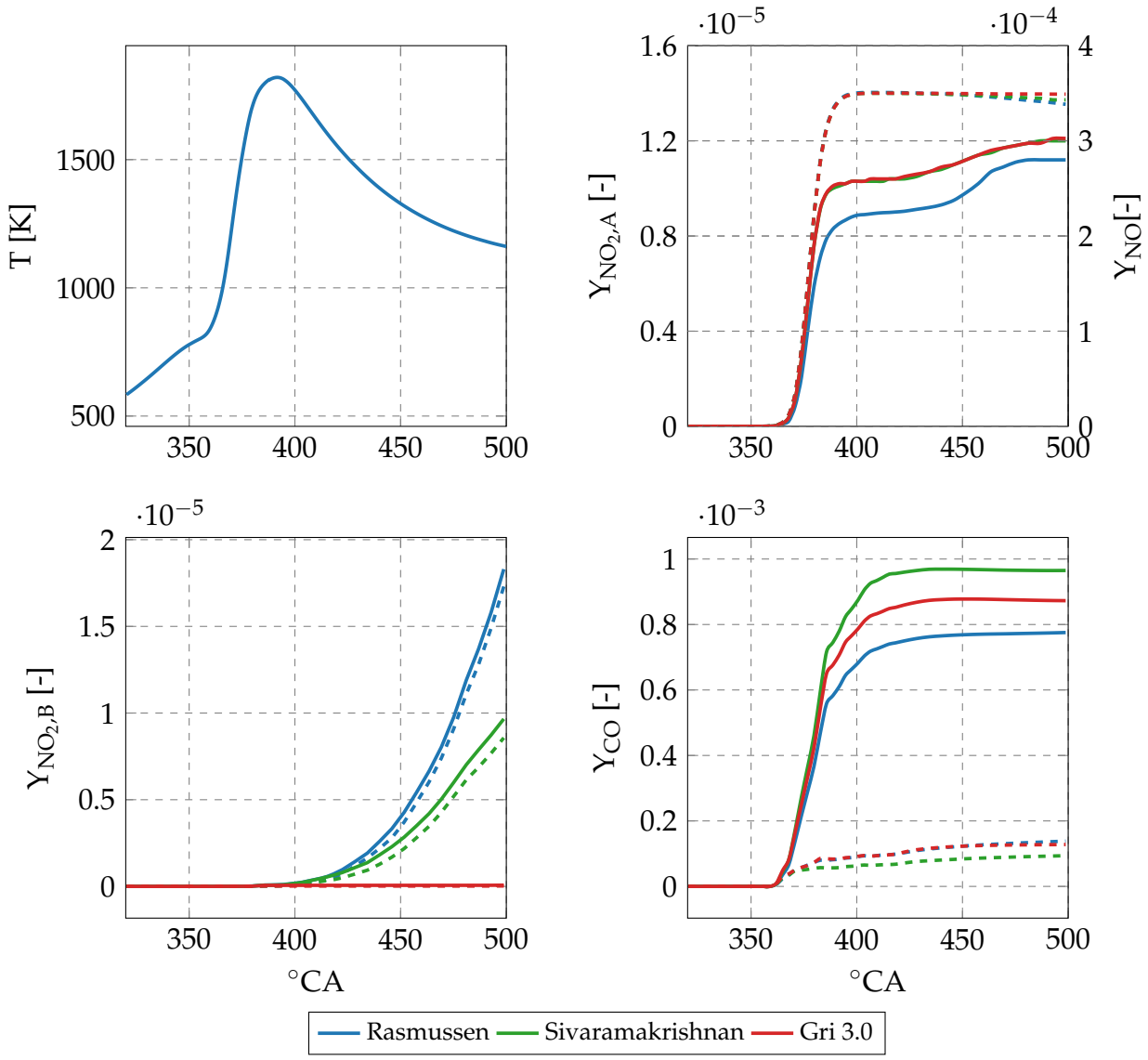

Figure 5.5: Temperature (upper left) and species evolution for case FL, calculated by using the look-up tables generated with the kinetic mechanisms of Rasmussen, Sivaramakrishnan, and Gri 3.0; Upper right: Y_{NO_2} (——) produced under the absence of CH_4; Y_{NO} (- - - - -) considering NO production and conversion to NO_2 under absence and presence of CH_4. Lower left: Y_{NO_2} under the presence of CH_4 without consideration of conversion of NO_2 back to NO (——) and with considering NO_2 conversion back to NO (- - - - -); Lower right: Y_{CO} without considering CO oxidation (——) and under consideration of CO oxidation (- - - - -)

the presence and absence of CH_4. It is to be noted that equation 4.5, described in Section 4.1 for predicting the NO production, was multiplied

with a correction factor to reproduce the experimental results shown later on. $Y_{NO_2,B}$ mass fractions refer to the NO_2 mass fractions predicted under the presence of CH_4 and NO. For predicting each $Y_{NO_2,B}$, two scalars were transported with the source terms retrieved from the respective look-up table. Their mean evolutions over the crank angles are depicted in the lower left part of the Figure 5.5. One scalar corresponds to the NO to NO_2 conversion (full line) and one scalar represents the NO to NO_2 conversion as well as the NO_2 conversion back to NO (dashed line). The latter scalar represents the final NO_2 mass fraction, which can be compared with the measurements. It can be seen that the NO_2 formation in the presence of CH_4 starts as the unburned CH_4 and NO formed in different zones are mixed. The kinetic mechanisms of Rasmussen and Sivaramakrishnan predict an augmentation of the NO_2 mass fraction, which is predicted to be faster by the Rasmussen kinetic. Surprisingly, the Gri 3.0 kinetic mechanism does not predict any NO_2 formation in the presence of CH_4. It can also be seen that the extent of conversion of produced NO_2 to NO predicted by the Rasmussen and the Sivaramakrishnan kinetic mechanisms remains very low due to the low temperature at which NO_2 was formed. In the lower right part of Figure 5.5 the mean evolutions of the CO mass fractions are shown. Like $Y_{NO_2,B}$, to predict each Y_{CO}, two different scalars were defined and transported with the source terms retrieved from the respective look-up table. One scalar represents the CO production (full line) and one scalar represents the CO production and its consumption (dashed line). The latter scalar illustrates the final CO mass fraction, that can be compared with the measurements. It can be seen that the Sivaramakrishnan kinetic mechanism predicts a higher production rate of CO from the unburned CH_4 tracer ($Y_{TCH_4,Q}$), followed by a higher oxidation rate. The Rasmussen and Gri 3.0 kinetic mechanisms predict similar levels of CO after its oxidation. In the following, the presented NO_2 mass fraction ($Y_{NO_2,B}$), driven by the available CH_4, as well as CO mass fraction (Y_{CO}), refer to those with considering the possible NO_2 conversion back to NO and CO oxidation, respectively. These are the values that should be compared with the experiment.

Figure 5.6 illustrates the spatial distribution of different scalars for case FL at 499 °CA. The specie evolutions were calculated by using the look-up table generated with the Rasmussen kinetic mechanism.

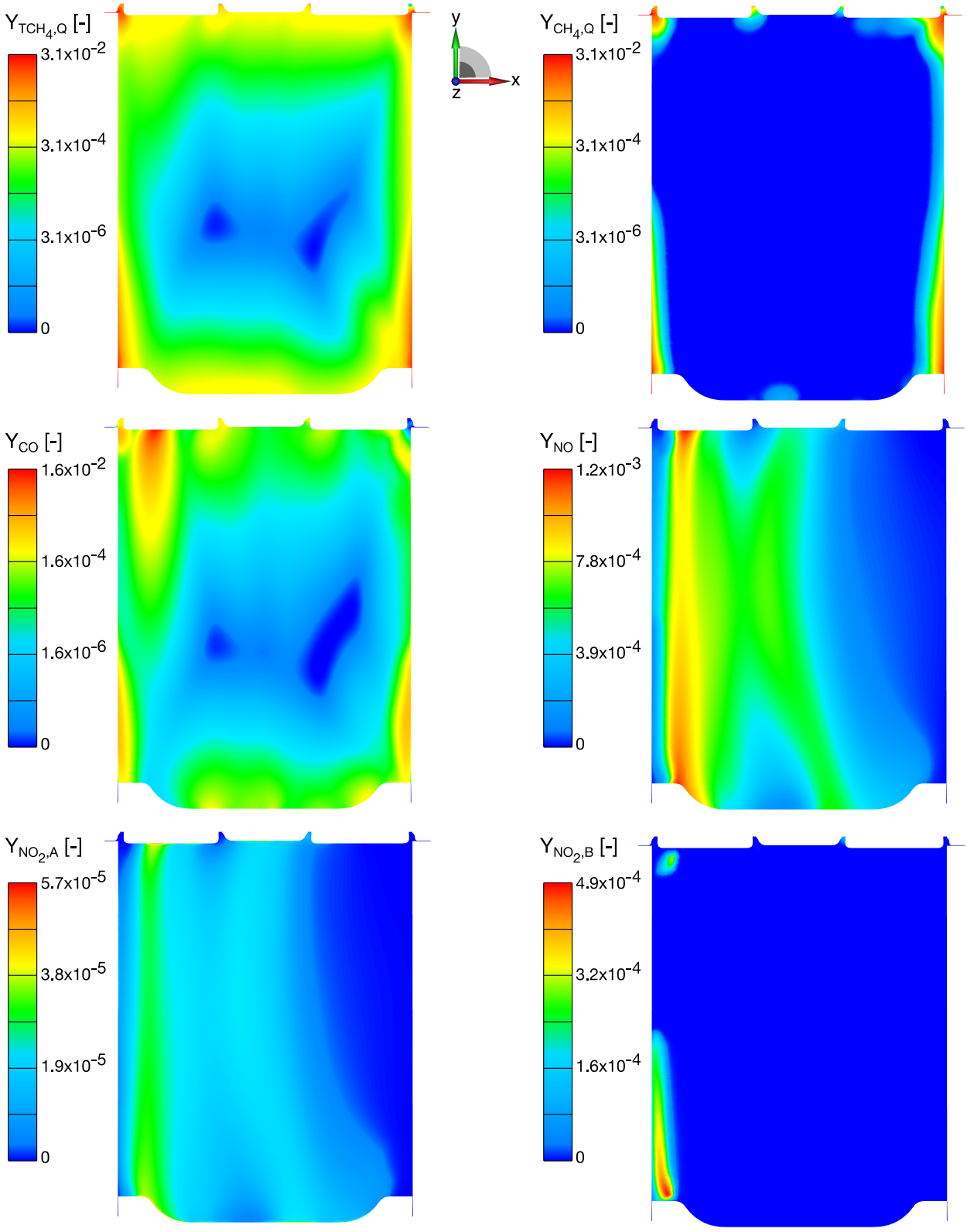

Figure 5.6: Spatial distribution of the species at 499 °CA shortly before the exhaust valves opening for case FL on the cut surface perpendicular to the z axis through the center point (0, 0, 0) according to the upper part of figure 3.5; species evolutions calculated using the look-up table generated with the kinetic mechanism of Rasmussen

The Y_{NO} distribution includes both the NO production with the correction factor as well as the NO conversion to NO_2. It can be seen that $Y_{CH_4,Q}$, meaning the remaining CH_4 after post-oxidation is mainly due to CH_4 from crevices.

As mentioned previously, NO_2 is split into two parts. For the portion of NO_2 formed in the presence of NO and O_2 (absence of CH_4), namely $Y_{NO_2,A}$, the spatial distribution is the same as that of NO. Its level is lower than NO by a factor of 20. For the portion of NO_2 formed under the presence of CH_4-NO-O_2 ($Y_{NO_2,B}$), NO_2 formation is limited to a small region located at the left side of the domain, where CH_4 and NO both exist. During the exhaust valves opening and thus the charge exchange, NO is distributed over a wider width, such that NO_2 formation also rises on the opposite side of the domain as shown for 680 °CA in Figure 5.7. It is obvious from the distribution of unburned CH_4 and NO, that a portion of unburned CH_4 exits the engine before mixing with NO. This leads to a time-dependent CH_4-NO mixture composition in the exhaust duct, which must be taken into account for calculating the species evolution in the exhaust duct described in the next section. The other case PL (not plotted), also shows the same spatial distribution of the investigated species but with different absolute values.

In the following, the time-averaged and area-averaged species mass fractions at the CFD evaluation point close to the engine, shown in figure 5.1, for cases FL and PL are investigated. The mean values are evaluated using

$$Y_{i,averaged} = \frac{\int Y_i(t)\,dt}{\int dt} \quad \text{with} \quad Y_i(t) = \frac{\int \dot{m}_i(t)\,dA}{\int \dot{m}(t)\,dA} \tag{5.1}$$

where $\dot{m}_i(t)$ is the mass flow of species i for each cell on the integration surface at the CFD evaluation position shown in Figure 5.1.

Figure 5.8 shows the NO mole fraction without considering its conversion to NO_2 at the CFD evaluation point for cases FL and PL, computed from the equation 4.5 and compared with X_{NO_x} (as the summation of X_{NO} and X_{NO_2}) measured at FTIR-HP. Since it was not possible to reproduce the experimental results by using the equation 4.5, this equation was modified by introducing the correction factor A_{corr} leading to:

$$\overline{\dot{\omega}}_{NO} = A_{corr} \int \dot{\omega}_{NO}(T) P(T) dT \tag{5.2}$$

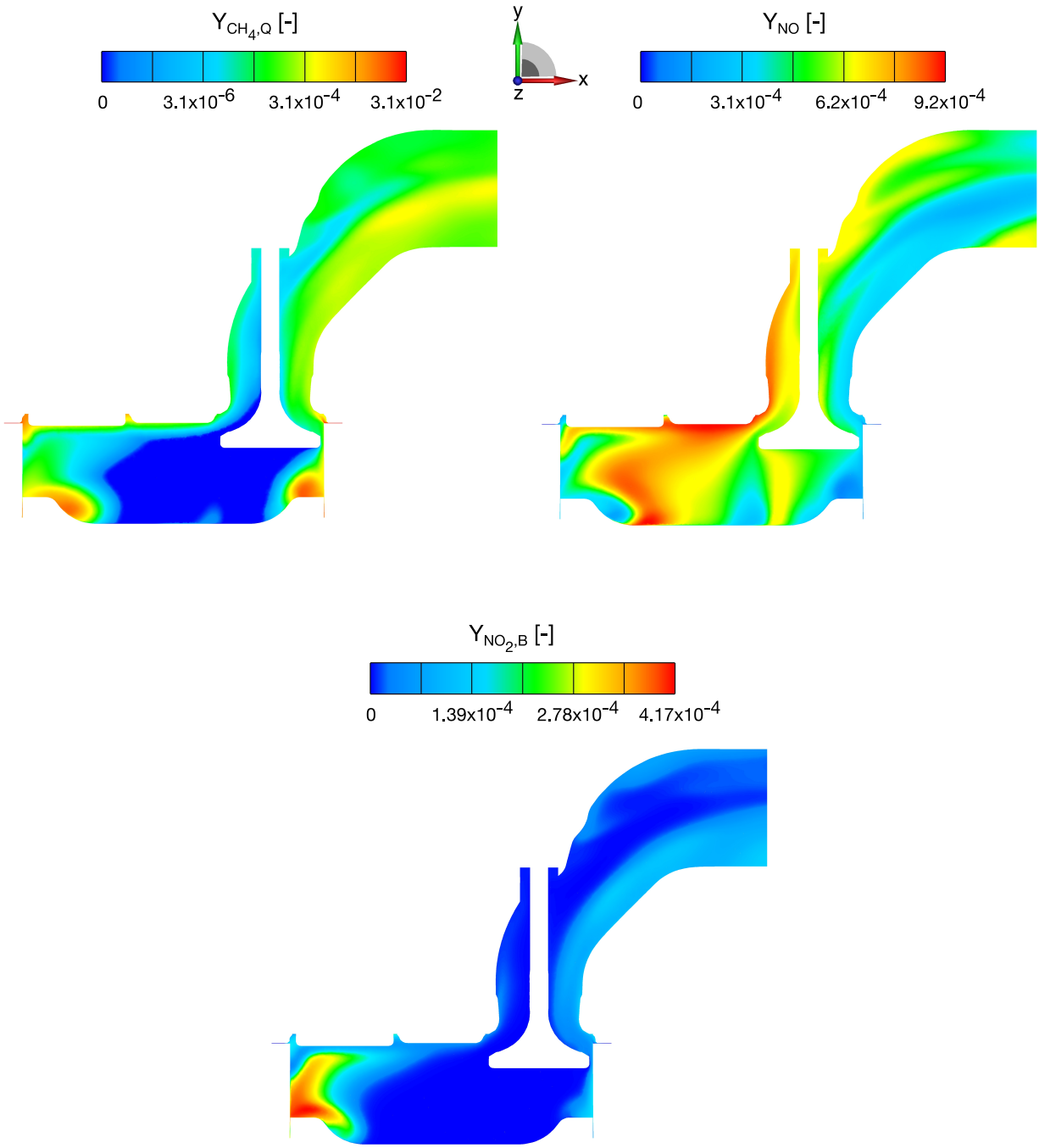

Figure 5.7: Spatial distribution of scalars at 680°CA for case FL on the cut surface perpendicular to the z axis through the center point (0, 0, 0) according to the lower part of figure 3.5; species evolutions calculated using the look-up table generated with the kinetic mechanism of Rasmussen

In the present work, the correction factor A_{corr} was set to 0.5 for both simulated cases FL and PL. Through the correction factor, it was possible to reproduce the experimental results, as shown in the Figure 5.8.

The correct estimation of NO amounts in the CFD calculations is essential, since its concentration affects the NO_2 formation, as mentioned previously. The conversion rates from the look-up tables during the CFD simulations were retrieved with respect to the corrected NO mass fractions.

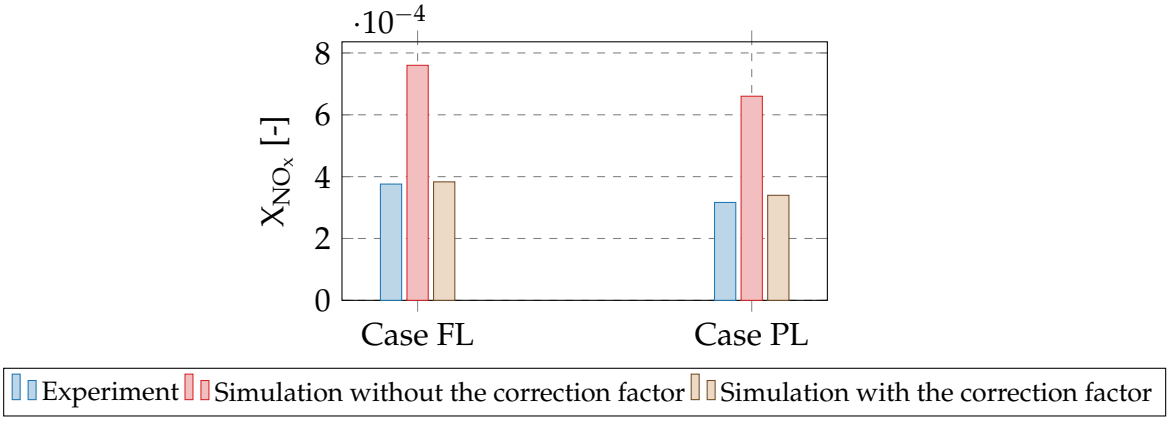

Figure 5.8: X_{NO} at the CFD evaluation point without considering NO to NO_2 conversion compared with the summation of X_{NO} and X_{NO_2} measured at FTIR-HP

In the next step, the time- and area-averaged species mass fractions of CH_4, CO, NO_2 and NO at the CFD evaluation point close to the engine (figure 5.1) for cases FL and PL are shown in Figure 5.9. The illustrated NO mass fractions include the NO production with the above-mentioned correction factor as well as the NO conversion to NO_2. For case FL, the modeled $Y_{TCH_4,Q}$ and $Y_{CH_4,Q}$ are slightly higher than those in case PL. The results from each of the three kinetic mechanisms in predicting CH_4 post-oxidation are almost the same. Like CH_4 mass fractions, the CO mass fractions predicted by each kinetic mechanism exhibit a slightly higher level in case FL. The Sivaramakrishnan kinetic mechanism predicts a lower level of CO compared with the CO mass fractions predicted by the Rasmussen and Gri 3.0 kinetic mechanisms. The predicted NO_2 mass fractions in the absence of CH_4 ($Y_{NO_2,A}$) and those in the presence of CH_4 ($Y_{NO_2,B}$) predicted by the three kinetic mechanisms are higher in case FL. Thus $Y_{NO_2,total}$ as the summation of $Y_{NO_2,A}$ and $Y_{NO_2,B}$ is higher for case FL. The higher NO_2 predicted for case FL was to be expected according to previous investigations, because of the higher NO mass fraction in case FL. Now considering each contribution separately, the deviations between $Y_{NO_2,A}$ predicted by each of the three mechanisms remain low. However

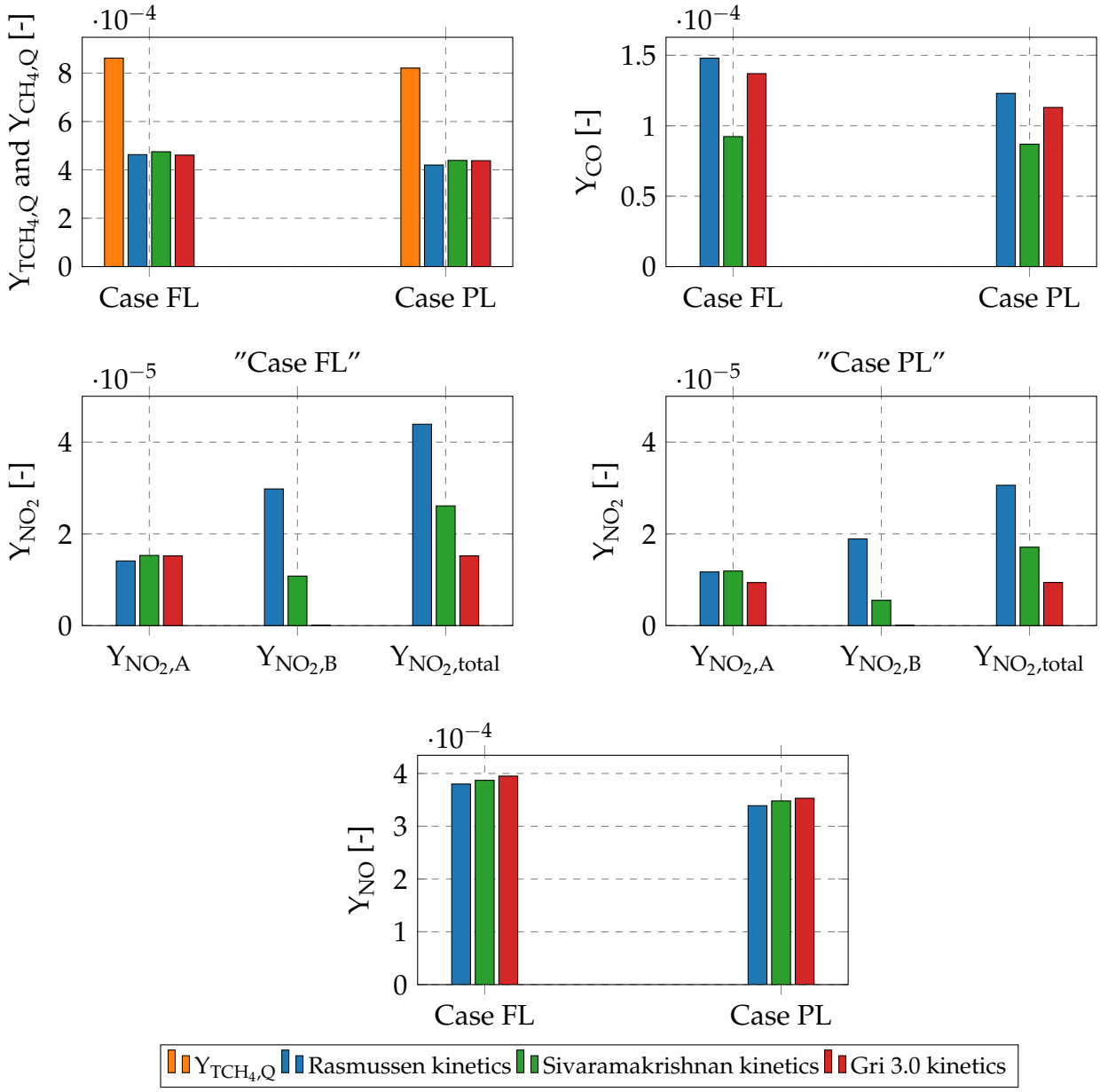

Figure 5.9: Predicted mean unbunred CH_4 tracer $Y_{TCH_4,Q}$ and other species mass fractions at the CFD evaluation point for cases FL and PL, calculated by using the look-up tables generated with the kinetic mechanisms of Rasmussen, Sivaramakrishnan, and Gri 3.0

the predicted $Y_{NO_2,B}$ by different mechanisms show considerable deviations. The kinetic mechanism of Rasmussen predicts the highest level of NO_2, whereas the Sivaramakrishnan kinetic mechanism exhibits a lower level of NO_2 formation under the presence of CH_4. Surprisingly, the Gri

3.0 mechanism does not predict any NO_2 formation under the presence of CH_4 for the investigated conditions.

In the following section, the evolutions of species in the exhaust duct up to the FTIR-HP measuring point for cases FL and PL are calculated are compared with experimental results.

5.2 Pollutant Formation and Conversion in the Exhaust Duct at the FTIR-HP Measuring Point

The closest measuring point, FTIR-HP, shown in Figure 5.1 is located further downstream relative to the location of CFD evaluations. For this reason, homogeneous reactor calculations employing different kinetic mechanisms are conducted in Cantera between the CFD evaluation point and the FTIR-HP measuring point.

From the spatial distribution of $Y_{CH_4,Q}$ and Y_{NO} in the engine presented in the previous section, it was to be expected that a portion of unburned CH_4 would not be mixed with NO prior to the measuring point. Thus, the mixture composition regarding CH_4, NO, and NO_2 exiting the engine differed in time. Taking the time averaged species mass fractions of unburned CH_4, NO and NO_2 evaluated at the engine exit as the initial mixture composition for a single batch reactor calculation, would not be a correct approach for modeling the species evolution in the exhaust duct.

In order to overcome this problem, a series of batch reactors were calculated independently: 1120 separate reactor calculations were conducted, according to the number of time steps, for which the CFD results were evaluated. For each reactor calculation the time-dependent and area-averaged mass fraction of unburned CH_4, NO, NO_2 and CO from CFD results at the evaluation position close to engine exit have been taken as the initial mixture composition. Thus, each time-dependent area-averaged mixture composition was treated separately, undergoing a reaction during the residence time between the CFD evaluation point and FTIR-HP. The averaged species mass fractions resulting from 1120 separate reactor calculations were then calculated. The other species mass fractions for initializing the reactors mixture compositions, including the mass fractions of the main combustion products O_2, N_2,CO_2, H_2O as well as OH are given in Table 5.1. The mean temperatures and pressures for the re-

actor calculations as well as the gas residence times are listed in the table as well. The residence time was calculated using the averaged mass flow

Table 5.1: Other species mass fractions for initializing the reactors mixture compositions

	Y_{O_2}	Y_{N_2}	Y_{CO_2}	Y_{H_2O}	Y_{OH}	T [K]	p [bar]	t_{res} [s]
Case FL	0.119	0.727	0.091	0.065	1.67E-05	850	1.98	0.08
Case PL	0.123	0.724	0.087	0.062	1.7E-05	790	1.41	0.096

rate, averaged density and the volume of the exhaust duct up to the FTIR-HP measurement point. The mean temperature and pressure were taken from experimental measurements in the exhaust duct. The reactor calculations were carried out by employing the detailed kinetic mechanisms of Rasmussen, Sivaramakrishnan and Gri 3.0. Figure 5.10 shows the averaged species mass fractions for the operation points FL and PL, which are compared with the experiments. Hereinafter, the unburned CH_4 mass fraction $Y_{CH_4,Q}$ is termed Y_{CH_4}.

The results revealed species conversions during the residence time in the exhaust duct for all the species. The CH_4 mass fractions predicted by all the three kinetic mechanisms for both cases remained below the experimental results. In particular, the deviation for case PL was the highest. The reason for the deviation between the simulation and experimental results, particularly for case PL, could be traced back to the underestimation of $Y_{TCH_4,Q}$ at the engine exit plotted in Figure 5.9. For case PL, $Y_{TCH_4,Q}$ had almost the same level as the measured CH_4 mass fraction at FTIR-HP. Assuming no post-oxidation of CH_4, the experimental results would be achieved for case PL, but it was obvious that a portion of $Y_{TCH_4,Q}$ had to undergo an oxidation. In the present work, the wall-flame quenching and the crevices were considered as the potential sources for the unburned CH_4 mass fractions. Particularly for the low load operation point (PL), it might be concluded that a portion of the measured unburned CH_4 should originate from other sources than flame-wall quenching and crevices.

Like CH_4, CO mass fraction also changed in the exhaust duct. This increased slightly due to the CH_4 post-oxidation. The deviations seen between simulated and measured CO for two cases might be partly related

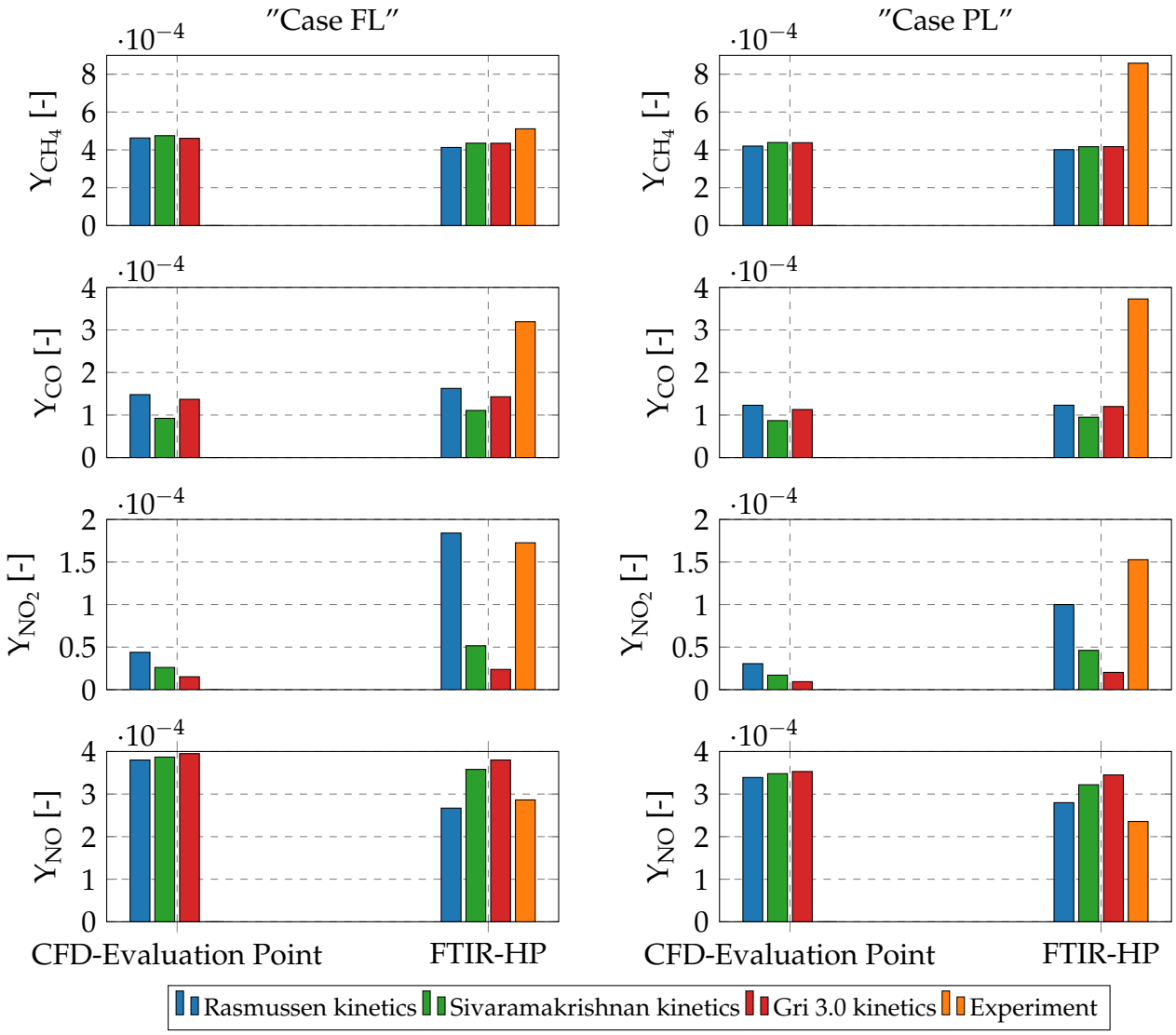

Figure 5.10: Evolution of the species mass fractions from CFD-Evaluation point up to FTIR-HP point calculated by averaging the results of 1120 reactors employing different kinetic and their comparison with experiment. Left: Case FL; Right: Case PL

to possible underestimated $Y_{TCH_4,Q}$ at the engine exit, since the CO conversion rate was tabulated depending on, among other things, $Y_{TCH_4,Q}$.

Like the CH_4 and CO mass fractions, Y_{NO_2} and Y_{NO} underwent changes in the exhaust duct as well. Thereby, Y_{NO_2} refers to the total NO_2 mass fraction. The NO_2 formation and as a result the NO reduction in the exhaust duct could be seen.

For case FL, Y_{NO_2} was measured to be higher than that in case PL, which was in accordance with the simulated values predicted by each kinetic mechanism. It was observed that the Rasmussen kinetic mechanism could reproduce the measured NO_2 the best, whereas the Sivaramakrishnan kinetic mechanism predicted a lower extent of NO_2 formation, followed by Gri 3.0. Particularly for case FL, the Rasmussen kinetic mechanism reproduced the measured Y_{NO_2} and Y_{NO} very well, whereas for case PL the deviation was higher but still satisfactory. As for underestimated CO, a higher deviation between simulated NO_2 predicted by the Rasmussen kinetic mechanism and measured NO_2 for case PL might be traced to the possible underestimation of $Y_{TCH_4,Q}$.

It can be concluded that significant NO_2 production and as a result NO reduction occurred in the exhaust duct, where the mixture underwent a reaction during high residence times at low temperatures, which were still high enough for partial oxidation of CH_4.

The NO_2 formation in the exhaust duct was not only the result of CH_4-NO-O_2 mixing and high residence times but also due to the OH radicals in the engine exhaust gas. The amount of OH radicals was calculated in the framework of ECFM3Z combustion as described in Section 4.1. The effect of ignoring the OH mass fraction in predicting the NO_2 formation in the exhaust duct is illustrated in Figure 5.11 for case FL. The previous reactor calculation was repeated for case FL, but Y_{OH} was set to zero. It was observed that without considering the OH radical, the simulated CH_4 mass fraction at FTIR-HP was higher than the previously calculated CH_4 mass fraction under consideration of the OH radical. This implies that the CH_4 conversion rate without the consideration of OH was lower. Consequently, there was hardly any conversion of NO to NO_2 without considering OH during the available residence time. Even the Rasmussen kinetic mechanism did not reproduce the experimental NO_2 mass fraction, if the OH radical was neglected. Thus, considering the OH mass fractions for the correct prediction of NO_2 is essential.

The mixture exiting the engine can include, besides the OH species, other radicals such as CH_2O resulting from the partial oxidation of the unburned CH_4 in the engine. The CH_2O mass fractions were measured at FTIR-HP and their influence on increasing NO_2 formation will be shown in the next section for high gas residence times in the exhaust duct from the FTIR-HP to the FTIR-LP measuring point. The CH_2O mass fraction

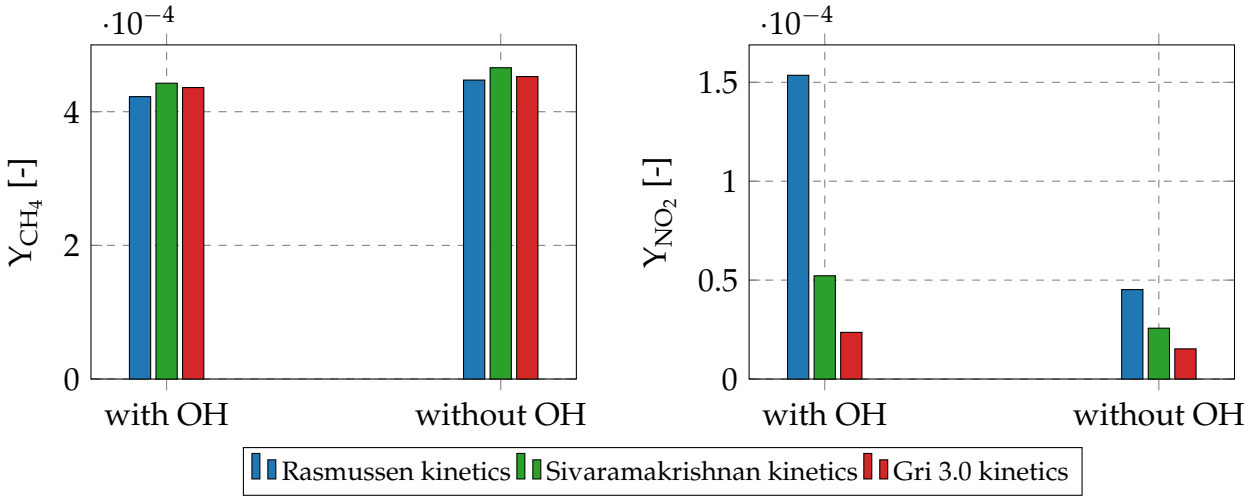

Figure 5.11: Comparison of the CH_4 and NO_2 mean species mass fractions at FTIR-HP from the reactor calculation for case FL under consideration of OH from Table 5.1 (shown in figure 5.10) and without considering OH

was not modeled in CFD. However, it was possible to evaluate CH_2O amounts produced in the exhaust duct from the previous reactor simulations between the engine exit and FTIR-HP. The measured and simulated CH_2O mass fractions at FTIR-HP as well as their differences are shown in Table 5.2. The results imply that CH_2O was mainly produced in the

Table 5.2: Comparison of CH_2O mass fractions resulting from reactor calculations with the measured ones at FTIR-HP

	Simulated Y_{CH_2O}	Measured Y_{CH_2O}	Difference
Case FL	3.1E-5	4.53E-5	1.43E-5
Case PL	4.3E-5	5.94E-5	1.64E-5

exhaust duct, but there was still some amount of CH_2O that should originate from the engine. As a first approximation, it could be assumed that the differences between the measured and simulated CH_2O mass fractions at FTIR-HP should correspond to the mass fractions of CH_2O that originated from the engine. Thus, CH_2O mass fractions from the engine, were equal to 1.43E-5 and 1.64E-5 for cases FL and PL, respectively. The previous reactor calculations were repeated employing the Rasmussen kinetic mechanism, but the initial mixture compositions were supplemented with Y_{CH2O}=1.43E-5 and 1.64Ee-5 for cases FL and PL, respec-

tively. The deviations between NO_2 mass fractions under the consideration of the above-mentioned CH_2O mass fractions and those without considering CH_2O are shown in Table 5.3. It can be concluded that CH_2O,

Table 5.3: Simulated NO_2 mass fractions under consideration of CH_2O and those without considering CH_2O employing the Rasmussen kinetic mechanism

	With Y_{CH_2O}	Without Y_{CH_2O}	Deviation
Case FL	1.9E-4	1.8E-4	1.E-5
Case PL	1.1E-4	1.0E-4	1.E-5

originated from the engine, affected the NO_2 formation. However, this effect was small for the investigated cases due to low residence times as well as low estimated CH_2O mass fractions.

The achieved results can be summarized as follows: among the three kinetic mechanisms, the Rasmussen mechanism reproduced the measured NO_2 at FTIR-HP fairly well. NO_2 was produced mostly in the exhaust duct, where the mixture of CH_4-NO-NO_2-O_2-OH underwent a reaction during residence times of 0.08 s and 0.096 s at low temperatures of 850 K and 790 K, respectively. The Sivaramakrishnan kinetic mechanism predicted the increase of NO_2 mass fractions to a lesser extent followed by Gri 3.0. NO_2 formation was accompanied by NO reduction. It was demonstrated that a portion of NO_2 was still formed in the engine. All three kinetic mechanisms predicted almost the same levels of in-cylinder NO_2 formation in the absence of CH_4. The in-cylinder NO_2 formation due to CH_4 was predicted by the Rasmussen kinetic mechanism and to a lesser extent by the Sivaramakrishnan kinetic mechanism, whereas Gri 3.0 did not predict any NO_2 formation from CH_4 at the engine exit. For case FL, it was possible to reproduce the measured NO_2 mass fraction using the Rasmussen kinetic mechanism fairly well, whereas the deviation between simulated and measured NO_2 for case PL was higher but still satisfactory. This deviation could be associated with the underestimation of $Y_{TCH_4,Q}$, leading also to high discrepancy between the simulated and measured CH_4 for case PL. The discrepancy between measured and simulated CO mass fractions could also be partly because of the possibly underestimated $Y_{TCH_4,Q}$.

5.3 Pollutant Formation and Conversion in the Exhaust Duct at the FTIR-LP Measuring Point

In this section, the mixture composition evolution between the FTIR-HP and FTIR-LP measuring points is evaluated. The mixture residence time was much higher than between the CFD evaluation point at the engine exit and FTIR-HP. For modeling the species evolution, a single homogeneous reactor was employed in Cantera. Due to high residence times as well as the larger dimensions of the exhaust reservoir, the homogeneous reactor was assumed to be a good approximation. Table 5.4 shows the initial conditions for the reactor calculations for cases FL and PL. The initial mixture compositions correspond to the measured mean values at the FTIR-HP measuring point. The residence time of the mixtures were calculated using the mean mass flow, mean density and volume of the exhaust reservoir of 1 m^3.

Table 5.4: Initial conditions for homogeneous reactor calculations corresponding to the measured state of gas at the FTIR-HP measuring point

-	T [K]	p [bar]	t_{res} [s]	Y_{CH_4}	Y_{NO}	Y_{NO_2}	Y_{CH_2O}	λ
FL	850	1.98	1.21	5.11E-4	2.86E-4	1.73E-4	4.53E-5	1.90
PL	790	1.41	1.42	8.58E-4	2.36E-4	1.53E-4	5.94E-5	1.97

The results are illustrated in Figure 5.12. From the experimental results further CH_4 conversion accompanied by CO production as well as NO to NO_2 conversion was observed during the residence time between FTIR-HP and FTIR-LP. The kinetic mechanisms of Rasmussen and Sivaramakrishnan reproduced the experimental results very well, whereas Gri 3.0 predicted hardly any CH_4 reactivity and thus a very low extent of NO_2 formation. For case FL, the Rasmussen kinetic mechanism reproduced the measured CH_4 and CO better than the Sivaramakrishnan mechanism. In this case, NO_2 predicted by the Sivaramakrishnan kinetic mechanism was slightly higher than that predicted by the Rasmussen kinetic mechanism, whereas Sivaramakrishnan mechanism predicted a slightly lower NO_2 level for case PL. Compared with the predicted NO_2 formation at FTIR-HP in the previous section, it was observed that the proportionally higher

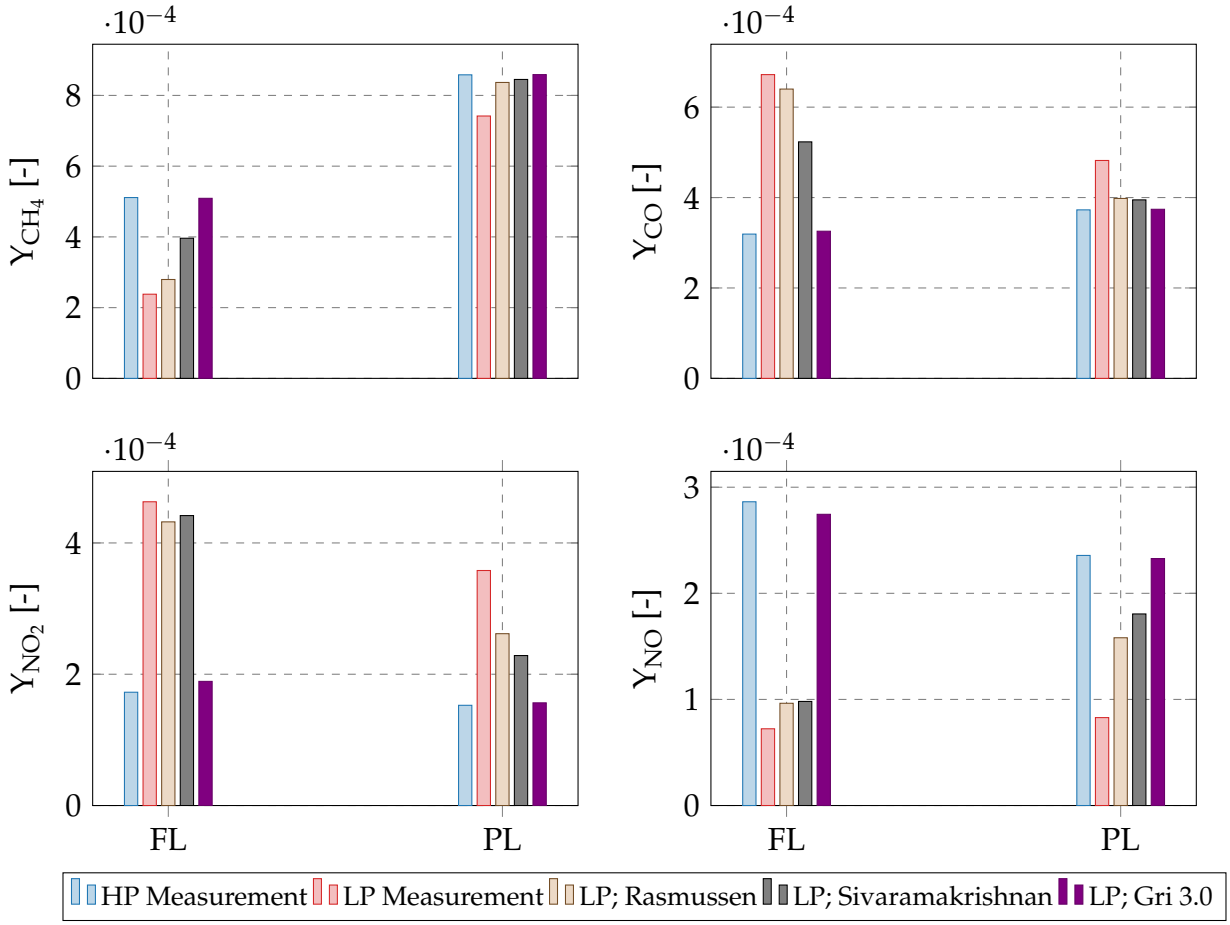

Figure 5.12: Further evolution of species mass fractions in the exhaust duct from the FTIR-HP to FTIR-LP measuring point for cases FL and PL

deviations between NO_2 predicted by each of the two mechanisms during a low residence time upto FTIR-HP vanished for higher residence times at FTIR-LP. This implies that for higher mixture residence times, both the Rasmussen and Sivaramakrishnan kinetic mechanisms performed similarly in predicting NO_2. The lesser extent of measured and simulated CH_4 oxidation accompanied by a lesser extent of NO_2 formation in case PL compared with case FL, was not only because of the lower temperature but also lower the NO mass fraction in case PL.

Summarizing the results presented in the present and preceding sections (5.1 and 5.2) for cases FL and PL regarding NO_2 formation, it can be concluded that the Gri 3.0 mechanism is not suitable in predicting NO_2 formation, neither in the engine (low mixture residence times) nor the exhaust duct (low to high mixture residence times). The Rasmussen mech-

anism was able to predict the NO_2 formation in the engine and in the exhaust duct, spanning different mixture residence times. Finally the Sivaramakrishnan kinetic mechanism was found to perform better for high residence times than for low residence times.

In the following, the results from the kinetic mechanisms for mixtures under high residence times between the FTIR-HP and FTIR-LP measuring points are presented for a few other operation points. The modeling of the exhaust duct for each case was conducted using a single homogeneous reactor in Cantera by employing the Rasmussen, Sivaramakrishnan and Gri 3.0 kinetic mechanisms. The initial conditions for reactor calculations are listed in Table 5.5 for mixtures at temperatures 829 K$<$T$<$ 877 K. The results of calculations are illustrated in Figure 5.13. The measurements

Table 5.5: Initial conditions for homogeneous reactor calculations corresponding to the measured state of gas at the FTIR-HP measuring point for mixture temperatures 829 K$<$T$<$877 K

	T [K]	p [bar]	t_{res} [s]	Y_{CH_4}	Y_{NO}	Y_{NO_2}	Y_{CH_2O}	λ
A	877	2.49	1.202	9.55E-4	2.1E-4	2.13E-4	6.59E-05	1.90
B	838	2.99	1.396	7.19E-4	9.94E-05	1.26E-4	3.83E-05	2.15
C	847	2.04	1.261	5.4E-4	2.48E-4	1.55E-4	4.14E-05	1.91
D	841	2.08	1.276	5.48E-4	3.28E-4	1.5E-4	3.82E-05	1.95
E	838	2.15	1.298	5.56E-4	3.2E-4	1.5E-4	3.82E-05	2
F	829	2.19	1.324	5.52E-4	4.07E-4	1.45E-4	3.605E-05	2.03

revealed oxidation of CH_4 accompanied by CO production for all investigated cases (A-F). The observed CH_4 oxidation led to NO_2 formation and thus to NO reduction. The Gri 3.0 mechanism predicted hardly any CH_4 oxidation and thus hardly any CO production during the residence time in the exhaust reservoir. As a result, NO_2 formation, and consequently NO reduction, occurred to a very low extent. It was observed that the Gri 3.0 mechanism was unable to reproduce the experimental results although the residence times were high. In contrast to the Gri 3.0 kinetic mechanism, the Rasmussen and Sivaramakrishnan mechanisms reproduced the experimental results very well. They both predicted higher CH_4 conver-

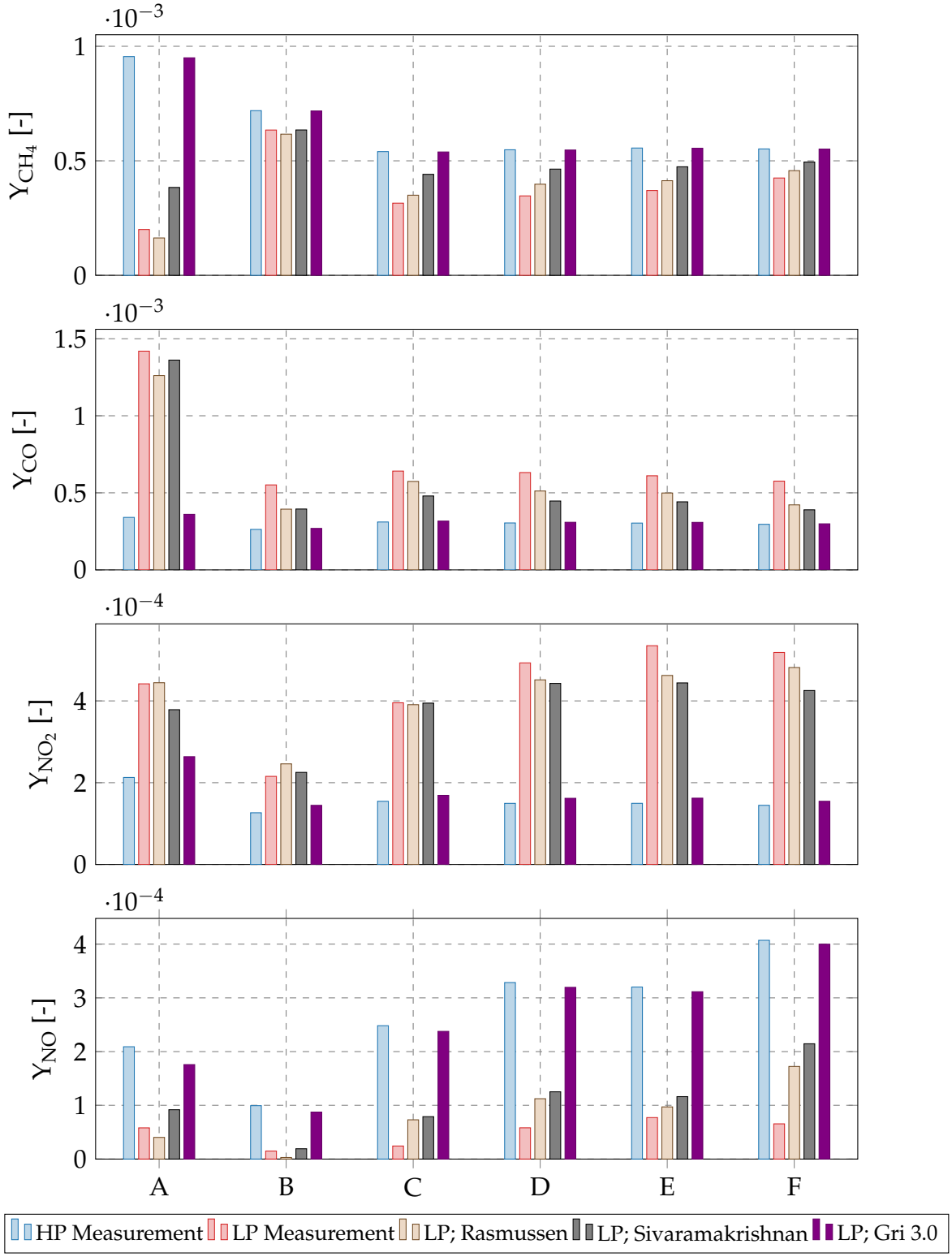

Figure 5.13: Comparison of the measured and the simulated species mass fractions at the FTIR-LP measuring point with the initial conditions from Table 5.5

sion and thus higher CO formation than Gri 3.0. In addition, the simulated NO_2 formation and the resulting NO reduction reproduced the measurements much better using both kinetic mechanisms. The overall performance of the Rasmussen mechanism was slightly better than the performance of the Sivaramakrishnan mechanism for the investigated mixture residence times. The CH_4 conversion predicted by the Rasmussen kinetic mechanism was constantly higher than that predicted by the Sivaramakrishnan mechanism. The CH_4 conversion from the experiments was higher than the predicted CH_4 conversion by the Rasmussen kinetic mechanisms except for cases A and B. In particular, for case A with the highest temperature, the Rasmussen kinetic mechanism predicted higher oxidation than that found in the experiment. This might imply that the mechanism overestimates the CH_4 oxidation at high temperatures. The lowest measured and simulated reactivity of CH_4 for case B was due to the lower amount of NO, which also led to the lowest NO_2 formation in this case.

Like the simulated CH_4 mass fractions, CO mass fractions predicted by both the Rasmussen and Sivaramakrishnan kinetic mechanisms reproduced the experimental results fairly well, which were predicted to be slightly lower than the measured ones.

The tendency of the measured NO_2 formation for different cases could be reproduced by the simulative results of the Rasmussen and Sivaramakrishnan kinetic mechanisms, with the exception of case F, where the NO_2 predicted by Rasmussen mechanism rose slightly despite the slight decrease of NO_2 in the experiment. Except for cases A and B, NO_2 predicted by Rasmussen lay below the experimental values. The higher NO_2 for cases A and B might be linked to the overestimation of CH_4 oxidation for these cases. The lowest levels of NO_2 formation were found for case B with the lowest NO mass fraction, which caused the lowest CH_4 reactivity. The Sivaramakrishnan mechanism could also reproduce the experiment well, where the final value of NO_2 lay mostly below those predicted by the Rasmussen mechanism, except for case C. The highest deviations between simulated NO_2 mass fractions by the two mechanisms of Rasmussen and Sivaramakrishnan were 15 % for cases A and F.

From the experiment and the kinetics calculations, it was observed that NO_2 production was accompanied by NO reduction. The NO mass fractions simulated by using the Rasmussen and Sivaramakrishnan kinetic mechanisms reproduced the tendency seen in the experimental results of

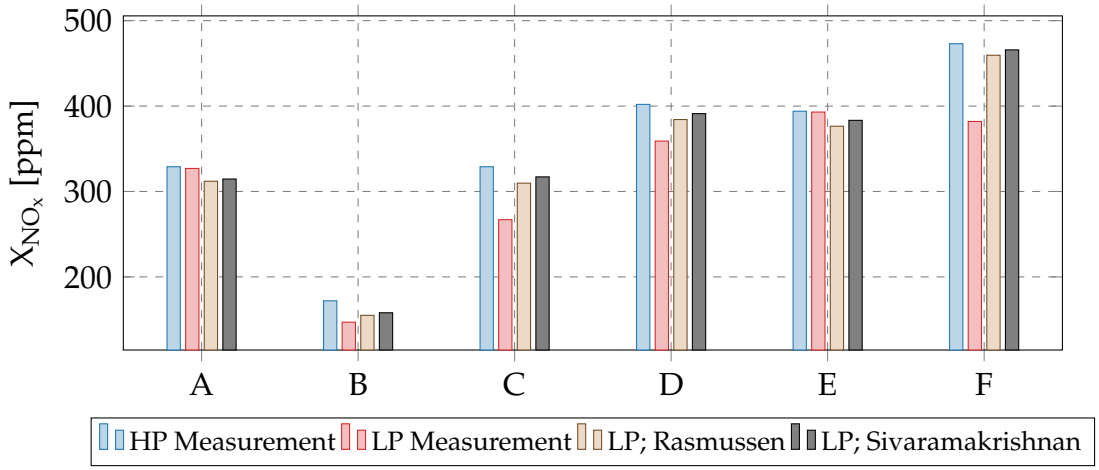

Figure 5.14: Comparison of the measured and the simulated NO_x mole fractions at the FTIR-LP measuring point with the initial conditions from Table 5.5

NO. In Figure 5.14, the mole fractions of NO_x as the sum of NO and NO_2 mole fractions measured at FTIR-LP are compared with those predicted by the Rasmussen and Sivaramakrishnan kinetic mechanisms. Except for case A and case E, the experimental results indicate NO_x reduction. The NO_x predicted by the Rasmussen and Sivaramakrishnan kinetic mechanisms also exhibited an almost constant reduction of 12-19 ppm and 5-14 ppm, respectively, during the investigated residence times. The higher measured NO_x reduction from the experiment for cases C, D, and F (with reductions of 62, 43 and 91 ppm, respectively) might be due to erroneous measurements of NO/NO_2 or rather other physical phenomena not considered in the reactor modeling. The possible reason for NO_x reduction predicted by the Rasmussen and Sivaramakrishnan mechanisms is explained using the reaction path diagram presented later in this section.

In the cases discussed so far, the temperature was still high enough for NO_2 production. In the following, the effect of lower temperatures on NO_2 formation is investigated. Figure 5.15 shows the measured and simulated evolution of NO_2 during gas residence time in the exhaust duct between HP-FTIR and LP-FTIR for lower temperatures (622 K<T<773 K). The corresponding initial conditions for the reactor calculations taken from the measurements at FTIR-HP are listed in Table 5.6. The temperatures were lower than those in the previous cases (A-F). The tendency of NO_2 measured at FTIR-LP could be reproduced by the reactor calculations employing the Rasmussen and Sivaramakrishnan kinetic mecha-

Table 5.6: Initial conditions for homogeneous reactor calculations corresponding to the FTIR-HP measuring point for mixture temperatures 622 K<T<773 K

-	T [K]	p [bar]	t_{res} [s]	Y_{CH_4}	Y_{NO}	Y_{NO_2}	Y_{CH_2O}	λ
G	773	1.65	1.58	1.21E-3	2.11E-4	1.28E-4	5.65E-05	2.14
H	742	1.45	1.64	5.72e-4	2.16E-3	1.33E-4	2.74E-05	2
I	739	2.25	1.81	3.46E-3	1.57E-4	1.6E-4	1.06E-4	2.4
J	713	1.62	1.61	7.38E-4	1.32E-3	1.23E-4	3.53E-05	2.3
K	683	1.89	1.73	1.98E-3	8.12E-4	1.4E-4	8.06E-05	2.5
L	655	2.79	1.96	5.16E-3	1.93E-4	1.02E-4	1.05E-4	2.8
M	652	2.23	1.89	3.13e-3	5.21E-4	1.3E-4	9.64E-05	2.7
N	622	2.89	2.1	4.37E-3	2.7E-4	1.14E-4	1.1E-4	3

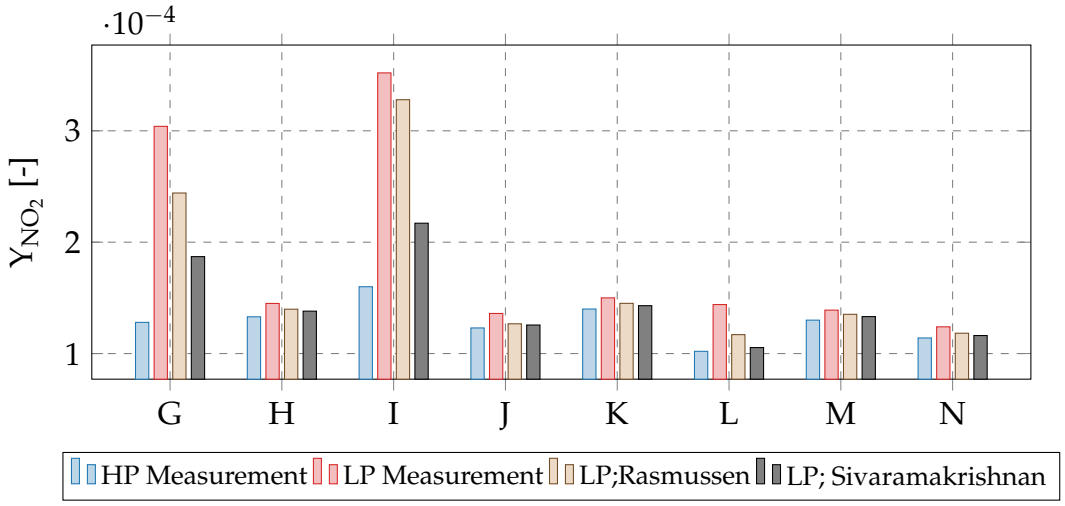

Figure 5.15: Comparison of the measured and the simulated NO_2 mass fractions at the FTIR-LP measuring point with the initial conditions from Table 5.6

nisms. The simulated NO_2 mass fractions at FTIR-LP were below the experimental values like the previous simulations. Like the previous cases, the overall prediction with the Rasmussen kinetic mechanism was better than that with the Sivaramakrishnan kinetic mechanism. The Gri 3.0 kinetic mechanism (not plotted) did not predict any NO to NO_2 conversion under the temperatures present in cases G-N, which were lower than the temperatures in preceding simulations.

It was observed that by decreasing temperature, the measured and simulated NO_2 formation dropped due to decreasing reactivity of the mixture. Cases J, K, M and N showed the lowest NO_2 formation due to the low temperatures. Case L with a temperature even lower than in cases J and K exhibited higher NO_2 formation that could be associated with the highest CH_4 concentration in this case. The effect of CH_4 on NO_2 formation was also observed for case I. The increased NO_2 formation for this case despite the same temperature with case H was caused by a higher CH_4 concentration for case I. For both cases I and L, the high concentration of CH_4 was associated with high concentrations of formaldehyde (CH_2O) species. CH_2O is an intermediate product of CH_4 conversion, produced through the partial oxidation of CH_4 upstream of the FTIR-HP measuring point, and its presence enhanced the reactivity of the mixture as well as augmented NO_2 formation. In Table 5.7, the deviations between the simulated NO_2 mass fractions at FTIR-LP under consideration of CH_2O and those without consideration of CH_2O are listed. The Rasmussen kinetic mechanism was employed for these comparisons. The

Table 5.7: Deviations between simulated NO_2 mass fraction at FTIR-LP with and without considering CH_2O

	A	B	FL	C	D	E	F
ΔY_{NO2}	1.45E-05	6.2E-06	1.5e-5	3.4E-05	7.9E-05	8.71E-05	17E-5

	PL	G	I
ΔY_{NO2}	8.7E-05	9.05E-05	12.E-5

effect of abundant CH_2O on NO_2 augmentation was seen. Without considering it, the final level of NO_2 was lower. In particular, the effect of CH_2O on increasing NO_2 mass fractions gets stronger with decreasing temperatures. The high amount of CH_2O, associated with high amounts

of CH_4, led to the NO_2 augmentation despite low temperatures, until the temperature was so low, that no reaction occurred during the available residence time as seen for cases N and M.

From the investigations in this section, the following conclusions could be drawn: The interaction of CH_4 and NO was observed in the measurements and reactor calculations by employing the Rasmussen and Sivaramakrishnan kinetic mechanisms. The CH_4 conversion was accelerated in the presence of NO and the NO conversion to NO_2 was enhanced in the presence of CH_4, provided that the temperature was high enough. There was a lower temperature limit, for which CH_4 oxidation and consequently NO to NO_2 conversion were almost frozen, which depended on CH_4 concentration. The Gri 3.0 mechanism predicted hardly any CH_4 conversion and very low NO_2 formation at the investigated temperatures and was unable to reproduce the experimental results. The Rasmussen and Sivaramakrishnan kinetic mechanisms predicted much higher conversion rates and reproduced the experimental results fairly well. It was also observed that the results of the Rasmussen and Sivaramakrishnan mechanisms for higher residence times became highly similar. However, the overall performance of the Rasmussen kinetic mechanism agreed with the measurements the best. It was also shown that the CH_2O radical produced through the partial oxidation of CH_4 affected the NO_2 formation, particularly at low temperatures and high residence times.

In the following, the dominant reaction paths in the reactive mixture of CH_4-O_2-NO, predicted by the Rasmussen and Gri 3.0 kinetic mechanisms are discussed. Figure 5.16 shows CH_4 and NO_2 evolution over time calculated in homogeneous reactors in Cantera. The initial conditions refer to those of case A from Table 5.5, with the exception of NO_2 mass fraction, which is set to zero. The Rasmussen kinetic mechanism predicted an earlier initiation of CH_4 oxidation and thus an earlier start of NO_2 formation than the Sivaramakrishnan mechanism. This led to higher deviations between the species mass fractions predicted by both mechanisms at lower residence times, while for higher residence times the predicted species mass fractions became closer. The dominant reaction paths predicted by Sivaramakrishnan are very similar to those predicted by the Rasmussen mechanism. The different performances of the Rasmussen and Sivaramakrishnan kinetic mechanisms might mainly originate from the different reaction rate coefficients or different thermodynamics properties of

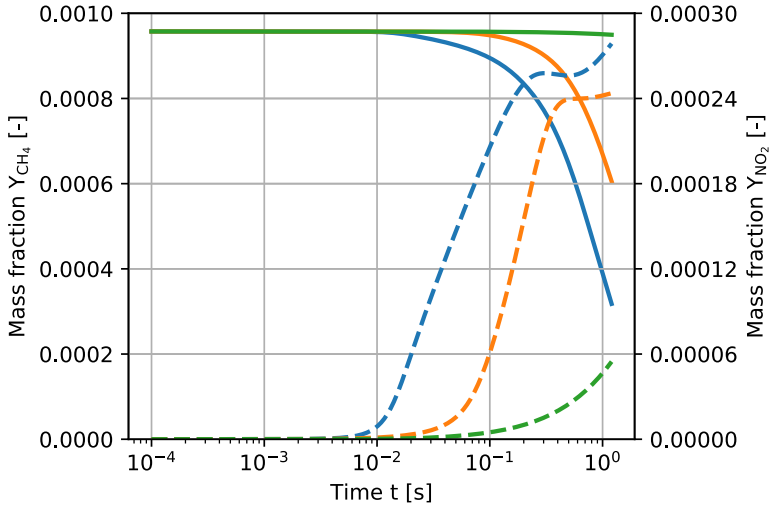

Figure 5.16: Time evolution of CH_4 (——) and NO_2 (- - - - -) mass fraction predicted by the Rasmussen (——), Sivaramakrishnan (——) and Gri 3.0 (——) kinetic mechanisms with initial conditions as for case A in Table 5.5 with initial Y_{NO_2}=0

the species. Thus, a detailed investigation is required to analyze the differences between the two kinetic mechanisms, which goes beyond the scope of this work. In the following, the main differences between the Gri 3.0 and the Rasmussen mechanisms are discussed by using the reaction path diagram. Figure 5.17 depicts the main paths of species conversions following C and N atoms predicted by the Rasmussen and Gri 3.0 kinetic mechanisms evaluated at t=0.1 s according to Figure 5.16. The conversion rates predicted by the Rasmussen mechanism were almost by two orders of magnitude higher than those predicted by Gri 3.0. The elementary reaction $CH_4 + OH = CH_3 + H_2O$ was the fastest fuel consuming step, as predicted by both mechanisms, which occurred via H radical abstraction by the OH radical. The chain reaction path $CH_3 \rightarrow CH_3O \rightarrow CH_2O \rightarrow HCO \rightarrow CO$, predicted by both kinetic mechanisms but with different rates, provided the system with the radicals pools that sustained the methane decay and determined its change rate. In addition the parallel path $CH_3 \rightarrow C_2H_6 \rightarrow C_2H_5 \rightarrow C_2H_4 \rightarrow C_2H_3 \rightarrow CH_2O \rightarrow HCO$ was responsible for CH_4 decay but to a lesser extent. The different results from the Rasmussen and the Gri 3.0 mechanisms can be traced back to different predicted CH_3

decay rates. The CH_3 conversion to CH_2O at the investigated temperature predicted by Gri 3.0 followed the path of

$$CH_3 + O_2 = CH_2O + OH \tag{5.3}$$

and to a lesser extent the path of

$$\begin{aligned} CH_3 + O_2 &= CH_3O + O \\ CH_3O(+M) &= CH_2O + H(+M) \end{aligned} \tag{5.4}$$

CH_3 to CH_2O conversion predicted by the Rasmussen mechanism followed the path of

$$CH_3 + O_2 = CH_2O + OH \tag{5.5}$$

and to a much higher extent the path of

$$\begin{aligned} CH_3 + NO_2 &= CH_3O + NO \\ CH_3O(+M) &= CH_2O + H(+M) \end{aligned} \tag{5.6}$$

followed by the path of

$$\begin{aligned} CH_3 + O_2 &= CH_3O_2 \\ CH_3O_2 + NO &= CH_3O + NO_2 \\ CH_3O(+M) &= CH_2O + H(+M) \end{aligned} \tag{5.7}$$

The reaction step $CH_3 + O_2$=$CH_2O + OH$ predicted by both kinetic mechanisms was not the dominant one in the Rasmussen reaction system. The parallel reaction steps 5.6 and 5.7 were the dominant steps when using the Rasmussen kinetic mechanism. These steps considered the interaction between NO and NO_2 with intermediate products and accelerated CH_3 consumption and thus CH_4 decay in the presence of NO_2 and NO. In the case of Gri 3.0, there was no direct interaction between NO/NO_2 and CH_3. This is the reason for the lower methane reactivity predicted by Gri 3.0 under the given conditions.

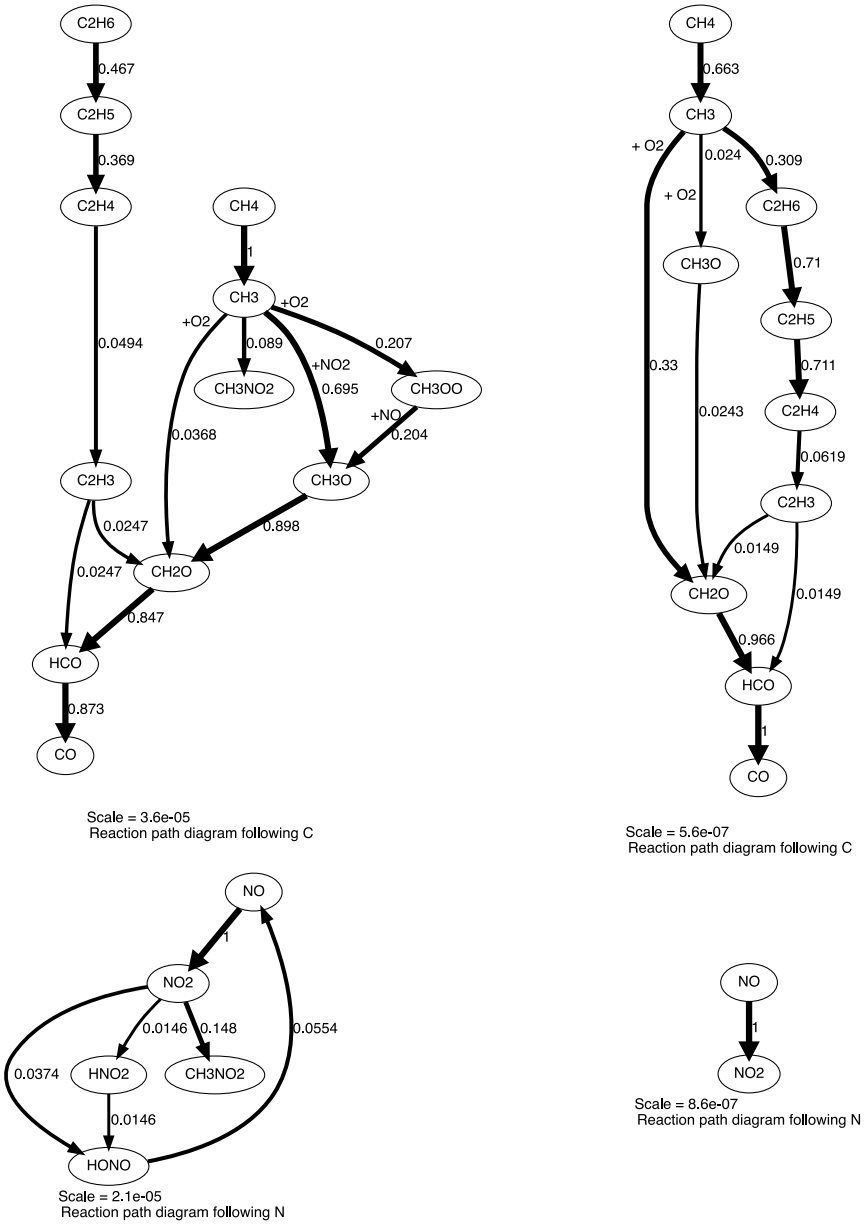

Figure 5.17: Fastest reaction paths following C and N atoms predicted by the Rasmussen (links) and Gri 3.0 (right) kinetic mechanisms

The main steps from formaldehyde CH_2O to CO were similar for both kinetic mechanisms but with different reaction rates:

$$\begin{aligned} CH_2O + OH &= H_2O + HCO \\ HCO + O_2 &= CO + HO_2 \end{aligned} \tag{5.8}$$

The key reaction step for NO_2 formation predicted by both kinetic mechanisms remained

$$HO_2 + NO = NO_2 + OH \tag{5.9}$$

with HO_2 radicals formed during the fuel decay described above but, also from the H_2/O_2 subsystems of each kinetic mechanism, mainly through:

$$H + O_2(+M) = HO_2(+M) \tag{5.10}$$

Faster HO_2 formation predicted by the Rasmussen kinetic mechanism due to the faster fuel decay than by Gri 3.0 leads to the faster NO_2 formation. Parallel to reaction 5.9 responsible for the NO_2 formation, the following steps predicted by both kinetic mechanisms, affected the NO_2 conversion back to NO:

$$\begin{aligned} H + NO_2 &= NO + OH \\ O + NO_2 &= NO + O_2 \\ NO_2 + M &= NO + O + M \end{aligned} \tag{5.11}$$

For the investigated low temperature (T=877 K), the NO_2 conversion back to NO through the reaction steps given in 5.11 was much slower than the NO conversion to NO_2 through path 5.9, leading to the increase of the NO_2 mass fraction. At high temperatures, the reaction steps in 5.11 become faster than reaction step 5.9, leading to the decreasing NO_2 mass fraction. While the Gri 3.0 mechanism predicts direct conversion of NO to NO_2 and vice versa according to the reaction steps 5.9 and 5.11, the Rasmussen kinetic mechanism includes more complex reaction paths in the subsystem of NO/NO_2, which can be found in detail in [16]. The reduction of NO_x (as the sum of NO and NO_2) predicted by the Rasmussen kinetic mechanism, as mentioned previously, can be traced back to the production of CH_3NO_2 species through the reaction step $CH_3 + NO_2$=CH_3NO_2, depicted in figure 5.17.

It can be concluded that the Rasmussen (and Sivaramakrishnan) kinetic mechanism includes elementary reaction steps, which model the direct interaction of CH_4 with NO and NO_2. This leads to faster radicals formation, which support a faster CH_4 decay and NO_2 formation compared with the results of the Gri 3.0 kinetic mechanism.

6 Summary and Conclusions

In this work the mechanism of NO_2 formation in a dual fuel (DF) engine with lean premixed methane-air ignited by diesel pilot fuel was investigated. A low order model based on a priori look-up tables was proposed for predicting in-cylinder NO_2 formation in CFD calculations. This approach was also applied to model unburned CH_4 post-oxidation and CO formation. Three different kinetic mechanisms, namely those of Rasmussen, Sivaramakrishnanm and Gri 3.0, were employed, and the results from these mechanisms were compared with each other.

Through fundamental studies with homogeneous reactors in Cantera, the conditions under which NO_2 is formed were determined. It was shown that high NO_2 formation is not a problem that originates from the hot gases in the combustion zone. NO_2 formation mainly occurs in the low/middle temperature range through the mixing of NO with small amounts of CH_4 in the presence of O_2 as an oxidizer. Based on the prestudy, the parameters that mainly affect the rate of NO_2 formation were determined, namely temperature, pressure, unburned CH_4, and NO and OH mass fractions. Due to the investigated lean combustion with $\phi \approx 0.5$ the mass fraction of O_2 was set to a constant value of 0.1127, corresponding to typical O_2 mass fractions in the flue gas following combustion when computing in-cylinder NO_2 formation with CFD. Slightly lower or higher values of O_2 mass fractions do not affect NO_2 formation that much, due to the different orders of magnitude of the investigated CH_4 and O_2 mass fractions.

The challenges of predicting in-cylinder NO_2 formation in CFD included the correct modeling of heat release, predicting NO production as well as modeling the CH_4 that survives combustion. Following these steps an appropriate method was required to model the conversion to NO_2.

The first prerequisite for modeling NO_2 was validating the combustion model. Combustion modeling was conducted in the software package AVL-Fire by using the ECFM3Z model, which allows efficient modeling

of auto-ignition, diffusion and premixed combustion in DF combustion. Since the ECFM3Z model was originally developed for diesel combustion, it was necessary to modify and extend the auto-ignition model as well as the computation of the laminar flame speeds. The latter adaption with respect to the modeling of laminar flame speeds was implemented in the present work. The former adaption regarding the auto-ignition modeling had already been implemented in AVL-Fire in previous work conducted at the Thermodynamics Institute and was used in the present work.

Auto-ignition was predicted in CFD by retrieving the ignition delay times from an a priori generated look-up table depending on the computational cell conditions. In the look-up table, the cold flame and main flame ignition delay times as well as the corresponding heat releases were stored, which were evaluated by using the temperature evolution computed with the constant volume homogeneous reactor model in Cantera employing the Chalmers kinetic mechanism. The reactor calculations were initialized with different temperatures, pressures, equivalence ratios and fuel fractions as ratios of n-heptane to total fuel mass (n-heptane and methane). The evaluated ignition delay times and heat releases were tabulated with respect to the above-mentioned parameters leading to a 4D look-up table for use in CFD.

For modeling flame propagation according to the flame surface density concept in the ECFM3Z model, an appropriate modeling of laminar flame speeds, particularly in the zones containing n-heptane and methane, was required. In the present work, the unstrained laminar flame speeds for methane-air and n-heptane-air mixtures were computed in Cantera by employing the Gri 3.0 and the Chalmers mechanism, respectively. The calculations were carried out for different temperatures, pressures and equivalence ratios. The computed laminar flame speeds were tabulated with respect to the above-mentioned parameters leading to two 3D tables for using in CFD. The influence of fuel mixture ratios on the laminar flame speed in CFD calculations was taken into account using linear interpolation of the tabulated flame speeds of both species.

Two engine operation points were simulated in CFD. The onset of ignition was adjusted with different factors for each case to match the experiments, whereas the turbulent flame propagation was adjusted with a unique parameter for both cases. The simulated evolution of the mean

temperatures and the heat release rates reproduced the experiment fairly well. This verified the functionality of the method of tabulation for predicting ignition and laminar flame speeds in the mixture of n-heptane-methane-air employing the ECFM3Z model.

Following combustion validation, the next prerequisite for predicting the NO_2 formation was predicting the NO formation. The turbulent NO formation rates were computed by employing the extended Zeldovich model under the consideration of turbulence effects through the PDF technique. The employed model, however, could not reproduce the measured NO_x, so that a correction factor was applied to the model. Correct estimation of NO production from combustion was essential for predicting the NO_2 formation.

For predicting the CH_4 amounts that would survive the combustion, a wall-flame quenching model based on a quench distance was implemented in AVL-Fire. In addition, crevices were taken into account as another source of unburned CH_4 flowing back into the cylinder during expansion.

In order to predict the unburned CH_4 post-oxidation as well as CO and NO_2 formation and conversion with low computational costs, an approach based on a priori constructed look-up tables was proposed in the present work. This approach was based on computing the conversion rates of the so-called progress variables corresponding to the above-mentioned species. The homogeneous reactor model was used in Cantera for computing the conversion rates. The reactor calculations were conducted for different temperatures, pressures, and CH_4, NO, and OH mass fractions employing the kinetic mechanisms of Rasmussen, Sivaramakrishnan and Gri 3.0. The conversion rates, computed with each aforementioned kinetic mechanisms, were tabulated with respect to temperature, pressure, and CH_4, NO and OH mass fractions and the corresponding progress variables, leading to three 6D look-up tables for use in CFD. In addition, the cut-off values, at which the produced NO_2 and CO species started converting to NO and CO_2, respectively, were evaluated and stored with respect to the temperature, pressure, and CH_4, NO and OH mass fractions leading to three 5D look-up tables for use in CFD. The O_2 mass fraction for generating the look-up tables was set to 0.1127, which corresponds to the O_2 mass fraction following CH_4-air combustion with ϕ=0.5.

For two cases, the in-cylinder pollutant formation and conversion, were calculated with transport equations with source terms retrieved from the look-up tables. The calculation distinguished between NO_2 produced in the presence of CH_4 and that formed in the absence of CH_4. For the latter portion of NO_2, the three kinetic mechanisms predicted very similar levels of NO_2, whereas the prediction of NO_2 formation driven by CH_4 differed for each mechanism. It was shown that the Rasmussen kinetic mechanism predicted the highest level of CH_4 driven NO_2 production, whereas the Sivaramakrishnan kinetic mechanism predicted a lower level. The Gri 3.0 kinetic mechanism could not predict any NO_2 formation driven by CH_4 during the available residence times in the engine.

Since the first measuring point was located further downstream of the engine exit, reactor calculations were conducted from the engine exit to the measuring point. This revealed that the Rasmussen kinetic mechanism could reproduce the experimental results much better than the of Sivaramakrishnan and Gri 3.0 kinetic mechanisms. The major part of NO_2 was produced in the exhaust duct, where the mixture of CH_4-O_2-NO-NO_2-OH experienced a mean temperature of 850 K and 790 K for a duration of approximately 0.1 s. The effect of OH radicals in the flue gas on NO_2 formation turned out to be essential. It was shown that the deviation between the simulated and measured NO_2 for the investigated part load operation point was higher than that for the full load operation point. This was in accordance with the higher deviation between the simulated and the measured CH_4 for the investigated part load operation point. Particularly for the part load operation point, it might be concluded that a portion of the measured unburned CH_4 should originate from other sources than flame-wall quenching and crevices considered in the present study. The CO mass fractions were also predicted to be below the experimental values, which could also be partly traced back to the underestimated CH_4 mass fraction.

For higher mixture residence times in the exhaust system, the Gri 3.0 mechanism still predicted hardly any CH_4 conversion and thus no NO_2 formation. The Rasmussen kinetic mechanism could reproduce the experimental results at the best. It could be seen that the results from the Sivaramakrishnan kinetic mechanism became very similar to those predicted from the Rasmussen kinetic mechanism for higher residence times. It was also shown that considering the CH_2O radical is important for pre-

dicting NO_2 evolution for mixtures with high residence times and low temperatures in the exhaust system.

The major elementary reaction paths for NO_2 formation predicted by all the kinetic mechanism is the step $NO + HO_2 = NO_2 + OH$. The Rasmussen and Sivaramakrishnan kinetic mechanisms model direct interactions between CH_4 and NO/NO_2 molecules, which enhance the radicals formation and accelerate the CH_4 oxidation and as a result augments NO to NO_2 conversion. Gri 3.0 does not include any paths for direct interaction between CH_4 and NO/NO_2. This led to much lower reactivity of CH_4 and NO_2formation predicted by Gri 3.0 under the investigated conditions.

Bibliography

[1] https://www.imo.org/en/OurWork/Environment/Pages/Air-Pollution.aspx.

[2] Cheng, W. K., Hamrin, D., Heywood, J. B., Hochgreb, S., Min, K., and Norris, M., 1993. "An Overview of Hydrocarbon Emissions Mechanisms in Spark-Ignition Engines". SAE Technical Paper 932708.

[3] Alkidas, A. C., Drews, R. J., and Miller, W. F., 1995. "Effects of Piston Crevice Geometry on the Steady-State Engine-Out Hydrocarbons Emissions of a S.I. Engine". SAE Technical Paper 952537.

[4] Bromly, J. H., Barnes, F. J., muris, S., You, X., and Haynes, B. S., 1996. "Kinetic and Thermodynamic Sensitivity Analysis of the NO-Sensitized Oxidation of Methane". *Combustion Science and Technology,* ***115***(4-6), pp. 259–296.

[5] Hori, M., Matsunaga, N., Marinov, N., William, P., and Charles, W., 1998. "An Experimental and Kinetic Calculation of the Promotion Effect of Hydrocarbons on the NO-NO2 Conversion in a Flow Reactor". *Symposium (International) on Combustion,* ***27***(1), pp. 389–396.

[6] Mckee, D. J., and Rodriguez, R. M., 1993. "Health Effects Associated with Ozone and Nitrogen Dioxide Exposure". *Water, Air, & Soil Pollution,* ***67***(1-2), pp. 11–35.

[7] Rutishauser, M., Ackermann, U., Braun, C., Gnehm, H. P., and Wanner, H. U., 1990. "Significant Association between Outdoor NO2 and Respiratory Syptoms in Preschool Children". *Lung,* ***168***(S1), pp. 347–352.

[8] Kerr, H., Kulle, T., McIlhany, M., and Swidersky, P., 1979. "Effects of Nitrogen Dioxide on Pulmonary Function in Human Subjects:

An Environmental Chamber Study". *Environmental Research,* ***19***(2), pp. 392–404.

[9] Rößler, M., Koch, T., Janzer, C., and Olzmann, M., 2017. "Mechanisms of the NO2 Formation in Diesel Engines". *MTZ worldwide,* ***78***(7-8), pp. 70–75.

[10] Rößler, M., Velji, A., Janzer, C., Koch, T., and Olzmann, M., 2017. "Formation of Engine Internal NO2: Measures to Control the NO2/NOx Ratio for Enhanced Exhaust After Treatment". *SAE International Journal of Engines,* ***10***(4), pp. 1880–1893.

[11] Hilliard, J. C., and Wheeler, R. W., 1979. "Nitrogen Dioxide in Engine Exhaust". SAE Technical Paper 790691.

[12] Olsen, D. B., Kohls, M., and Arney, G., 2010. "Impact of Oxidation Catalysts on Exhaust NO2 to NOx Ratio From Lean-Burn Natural Gas Engines". *Journal of the Air & Waste Management Association,* ***60***(7), pp. 867–874.

[13] Liu, S., Li, H., Liew, C., Gatts, T., Wayne, S., Shade, B., and Clark, N., 2011. "An Experimental Investigation of NO2 Emission Characteristics of a Heavy-Duty H2-Diesel Dual Fuel Engine". *International Journal of Hydrogen Energy,* ***36***(18), pp. 12015–12024.

[14] Li, Y., Li, H., Guo, H., Li, Y., and Yao, M., 2018. "A Numerical Investigation on NO2 Formation in a Natural Gas-Diesel Dual Fuel Engine". *Journal of Engineering for Gas Turbines and Power,* ***140***(9). GTP-17-1661.

[15] Goodwin, D. G., Speth, R. L., Moffat, H. K., and Weber, B. W., 2021. Cantera: An Object-oriented Software Toolkit for Chemical Kinetics, Thermodynamics, and Transport Processes. `https://www.cantera.org`. Version 2.5.1.

[16] Rasmussen, C. L., Rasmussen, A. E., and Glarborg, P., 2008. "Sensitizing Effects of NOx on CH4 Oxidation at High Pressure". *Combustion and Flame,* ***154***(3), pp. 529–545.

[17] Rasmussen, C. L., Hansen, J., Marshall, P., and Glarborg, P., 2008. "Experimental Measurements and Kinetic Modeling of

CO/H2/O2/NOx conversion at high pressure". *International Journal of Chemical Kinetics,* ***40***(8), pp. 454–480.

[18] Bendtsen, A. B., Glarborg, P., and Dam-Johansen, K., 2000. "Low Temperature Oxidation of Methane: The Influence of Nitrogen Oxides". *Combustion Science and Technology,* ***151***(1), pp. 31–71.

[19] Glarborg, P., Alzueta, M. U., Dam-Johansen, K., and Miller, J. A., 1998. "Kinetic Modeling of Hydrocarbon/Nitric Oxide Interactions in a Flow Reactor". *Combustion and Flame,* ***115***(1-2), pp. 1–27.

[20] Sivaramakrishnan, R., Brezinsky, K., Dayma, G., and Dagaut, P., 2007. "High Pressure Effects on the Mutual Sensitization of the Oxidation of NO and CH4–C2H6 blends". *Physical Chemistry Chemical Physics,* ***9***(31), p. 4230.

[21] Smith, G. P., Golden, D. M., Frenklach, M., Moriarty, N. W., Eiteneer, B., Goldenberg, M., Bowman, C. T., Hanson, R. K., Song, S., Gardiner, W. C., Lissianski, J. V. V., and Qin, Z., 1994. GRI-Mech 3.0. `http://combustion.berkeley.edu/gri-mech/version30/text30.html`.

[22] Zeldovich, Y. B., Sadovnikov, P. Y., and Frank-Kamenetskii, D. A., 1947. "Oxidation of Nitrogen in Combustion". *Academy of Sciences of USSR, Institute of Chemical Physics, Moscow-Leningrad*.

[23] Lavoie, G. A., Heywood, J. B., and Keck, J. C., 1970. "Experimental and Theoretical Study of Nitric Oxide Formation in Internal Combustion Engines". *Combustion Science and Technology,* ***1***(4), pp. 313–326.

[24] Mooser, D., 2007. *Handbuch Dieselmotoren*, 3rd ed. Springer, Berlin/Heildelberg, Germany, chapter: Brenngase und Gasmotoren.

[25] Merker, G. P., Schwarz, C., and Teichmann, R., 2009. *Grundlagen Verbrennungsmotoren: Simulation der Gemischbildung, Verbrennung, Schadstoffbildung und Aufladung*, 4th ed. Vieweg Teubner, Wiesbaden, Germany.

[26] Mastorakos, E., 2009. "Ignition of Turbulent Non-Premixed Flames". *Progress in Energy and Combustion Science,* ***35***(1), pp. 57–97.

[27] Kuo, K., and Acharya, R., 2012. *Fundamentals of Turbulent Multi-Phase Combustion*. John Wiley and Sons: New York, NY, USA.

[28] Aggarwal, S. K., Awomolo, O., and Akber, K., 2011. "Ignition Characteristics of Heptane-Hydrogen and Heptane-Methane Fuel Blends at Elevated Pressures". *International Journal of Hydrogen Energy,* ***36***(23), pp. 15392–15402.

[29] Schlatter, S., Schneider, B., Wright, Y., and Boulouchos, K., 2012. "Experimental Study of Ignition and Combustion Characteristics of a Diesel Pilot Spray in a Lean Premixed Methane/Air Charge Using a Rapid Compression Expansion Machine". SAE Technical Paper 2012-01-0825.

[30] Schlatter, S., Schneider, B., Wright, Y., and Boulouchos, K., 2016. "N-heptane Micro Pilot Assisted Methane Combustion in a Rapid Compression Expansion Machine". *Fuel,* ***179***, pp. 339–352.

[31] Poinsot, T., and Veynante, D., 2005. *Theoretical and Numerical Combustion*, 2nd ed. Edwards, Philadelphia.

[32] Favre, A., 1969. "Statistical Equations of Turbulent Gases". In Problems of Hydrodynamics and Continuum Mechanics, SIAM, Philadelphia, pp. 231–266.

[33] Williams, F. A., 1985. *Combustion Theory*. Benjamin Cummings, Menlo Park, CA.

[34] Kuo, K. K., 1986. *Principles of Combustion*. John Wiley, New York.

[35] Hinze, J. O., 1975. *Turbulenz*. McGraw-Hill, New-York.

[36] Tennekes, H., and Lumley, J. L., 1972. *A First Course in Turbulence*. M.I.T. Press, Cambridge.

[37] Jones, W. P., and Launder, B. E., 1972. "The Prediction of Laminarization with a 2-Equation Model of Turbulence". *International Journal of Heat and Mass Transfer,* ***15***(2), pp. 301–314.

[38] Hanjalic, K., Popovac, M., and Hadziabdic, M., 2004. "A Robust Near-Wall Elliptic-Relaxation Eddy-Viscosity Turbulence Model for CFD". *International Journal of Heat and Fluid Flow,* ***25***(6), pp. 1047–1051.

[39] Popovac, M., and Hanjalic, K., 2007. "Compound Wall Treatment for RANS Computation of Complex Turbulent Flows and Heat Transfer". *Flow, Turbulence, and Combustion,* ***78***(2), pp. 177–202.

[40] Kendoush, A. A., Karbon, M., and Sleiti, A. K., 2020. "Turbulence Modeling Using Z-F Model and RSM for Flow Analysis in Z-SHAPE Ducts". *Journal of Engineering,* ***2020***, pp. 1–10.

[41] Medic, G., and Durbin, P. A., 2002. "Toward Improved Prediction of Heat Transfer on Turbine Blades". *Journal of Turbomachinery,* ***124***(2), pp. 187–192.

[42] Ramadami, K., Kelterer, M. E., Pecnik, R., and Sanz, W., 2009. "Application of the zeta-f Turbulence Model to Steady Transitional Flow". In Proceedings of Eighth European Conference on Turbomachinery Fluid Dynamics and Thermodynamics, pp. 119–130.

[43] Borghi, R., 1988. "Turbulent Combustion Modelling". *Progress in Energy and Combustion Science,* ***14***(4), pp. 245–292.

[44] Peters, N., 2000. *Turbulent Combustion*. Cambridge: Cambridge University Press.

[45] Spalding, D. B., 1971. "Mixing and Chemical Reaction in Steady Confined Turbulent Flames". *Symposium (International) on Combustion,* ***13***(1), pp. 649–657.

[46] Spalding, D. B., 1977. "Development of the Eddy-Break-Up model of turbulent combustion". *Symposium (International) on Combustion,* ***16***(1), pp. 1657 – 1663.

[47] Gerlinger, P., 2005. *Numerische Verbrenungssimulation: Effiziente Numersiche Simulation turbulenter Verbrennung*. Springer-Verlag Berlin Heidelberg.

[48] Warnatz, J., Maas, U., and Dibble, R., 2001. *Combustion*. Springer-Verlag Berlin Heidelberg.

[49] Nilsson, P., 2001. "A level-set flame library model for pemixed turbulent combustion". PhD thesis, Division of Fluid Mechanics, Department of Energy Sciences, Lund Institute of Technology.

[50] Peters, N., 1999. "The Turbulent Burning Velocity for Large-Scale and Small- scale Turbulence". *Journal of Fluid Mechanics,* ***384***, pp. 107 – 132.

[51] Van Oijen, J., and De Goey, L., 2002. "Modelling of Premixed Counterflow Flames using the Flamelet-Generated Manifold Method". *Combustion Theory and Modelling,* ***6***, pp. 463–478.

[52] Van Oijen, J., , and De Goey, L., 2007. "Modelling of Premixed Laminar Flames using Flamelet-Generated Manifolds". *Combustion Science and Technology,* ***161***, pp. 113–137.

[53] Cheng, W. K., and Diringer, J. A., 1991. "Numerical Modelling of SI Engine Combustion with a Flame Sheet Model". SAE Technical Paper 910268.

[54] Boudier, P., Henriot, S., Poinsot, T., and Baritaud, T., 1992. "A Model for Turbulent Flame Ignition and Propagation in Piston Engines". *24th Symp. (International) on Combustion, The Combustion Institute, Pittsburgh*, pp. 503–510.

[55] Duclos, J. M., Bruneaux, G., and Baritaud, T., 1996. "3D Modelling of Combustion and Pollutants in a 4 Valve SI Engine; Effect of Fuel and Residuals Distribution and Spark Location". SAE Technical Paper 961964.

[56] Choi, C. R., and Huh, K. Y., 1998. "Development of a Coherent Flamelet Model for a Spark Ignited Turbulent Premixed Flame in a Closed Vessel". *Combustion and Flame,* ***114***(3-4), pp. 336–348.

[57] Kuppa, K., 2018. "Prediction of Combustion and Emissions in Gas Engines". PhD thesis, Institute of Technical Combustion, Leibniz Universität Hannover.

[58] Pope, S., 1988. "The Evolution of Surfaces in Turbulence". *International Journal of Engineering Science,* ***26***(5), pp. 445–469.

[59] Bray, K. N. C., and Libby, P., 1986. "Passage Times and Flamelet Crossing Frequencies in Premixed Turbulent Combustion". *Combustion Science and Technology,* ***47***(5-6), pp. 253–274.

[60] Haworth, D. C., and Poinsot, T. J., 1990. "Numerical Simulations of Lewis Number Effects in Turbulent Premixed Flames". *Journal of Fluid Mechanics,* ***244***, pp. 405–436.

[61] Duclos, J. M., Veynante, D., and Poinsot, T., 1993. "A Comparison of Flamelet Models for Premixed Turbulent Combustion". *Combustion and Flame,* ***95***, pp. 101–117.

[62] Veynante, D., Piana, J., Duclos, J., and Martel, C., 1996. "Experimental Analysis of Flame Surface Density Models for Premixed Turbulent Combustion". *Symposium (International) on Combustion,* ***26***(1), pp. 413–420.

[63] Meneveau, C., and Poinsot, T., 1991. "Stretching and Quenching of Flamelets in Premixed Turbulent Combustion". *Combustion and Flame,* ***86***(4), pp. 311–332.

[64] Meneveau, C., and Sreenivasan, K. R., 1989. "Measurement of f(α) from Scaling of Histograms and Applications to Dynamical Systems and Fully Developed Turbulence". *Physics Letters A,* ***A137***(3), pp. 103–112.

[65] Meneveau, C., and Sreenivasan, K. R., 1991. "The Multifractal Nature of the Turbulent Energy Dissipation". *Journal of Fluid Mechanics,* ***24***, pp. 429–484.

[66] Poinsot, T., Veynante, D., and Candel, S., 1991. "Quenching Processes and Premixed Turbulent Combustion Diagrams". *Journal of Fluid Mechanics,* ***228***, pp. 561–606.

[67] Colin, O., and Benkenida, A., 2004. "The 3-Zones Extended Coherent Flame Model (ECFM3z) for Computing Premixed/Diffusion Combustion". *Oil & Gas Science and Technology,* ***59***(6), pp. 593–609.

[68] Maghbouli, A., Saray, R. K., Shafee, S., and Ghafouri, J., 2013. "Numerical Study of Combustion and Emission Characteristics of Dual-Fuel Engines using 3D-CFD Models Coupled with Chemical Kinetics". *Fuel,* ***106***, pp. 98–105.

[69] Li, Y., Guo, H., and Li, H., 2017. "Evaluation of Kinetics Process in CFD Model and its Application in Ignition Process Analysis of a

Natural Gas-Diesel Dual Fuel Engine". SAE Technical Paper 2017-01-0554.

[70] Hockett, A., Hampson, G., and Marchese, A. J., 2016. "Development and Validation of a Reduced Chemical Kinetic Mechanism for Computational Fluid Dynamics Simulations of Natural Gas/Diesel Dual-Fuel Engines". *Energy & Fuels,* ***30***(3), pp. 2414–2427.

[71] Colin, O., Benkenida, A., and Angelberger, C., 2003. "3D Modeling of Mixing, Ignition and Combustion Phenomena in Highly Stratified Gasoline Engines". *Oil & Gas Science and Technology,* ***58***(1), pp. 47–62.

[72] Henriot, S., Bouyssounnouse, D., and Baritaud, T., 2003. "Port Fuel Injection and Combustion Simulation of a Racing Engine". SAE Technical Paper 2003-01-1845.

[73] Kleemann, A. P., Menegazzi, P., Henriot, S., and Marchal, A., 2003. "Numerical Study on Knock for an SI Engine by Thermally Coupling Combustion Chamber and Cooling Circuit Simulations". SAE Technical Paper 2003-01-0563.

[74] Colin, O., da Cruz, A. P., and Jay, S., 2005. "Detailed Chemistry-Based Auto-Ignition Model Including Low Temperature Phenomena Applied to 3-D Engine Calculations". *Proceedings of the Combustion Institute,* ***30***(2), pp. 2649–2656.

[75] Belaid-Saleh, H., Jay, S., Kashdan, J., Ternel, C., and Mounaïm-Rousselle, C., 2013. "Numerical and Experimental Investigation of Combustion Regimes in a Dual Fuel Engine". SAE Technical Paper 2013-24-0015.

[76] Halstead, M., Kirsch, L., and Quinn, C., 1977. "The Autoignition of Hydrocarbon Fuels at High Temperatures and Pressures Fitting of a Mathematical Mode". *Combustion Flame,* ***30***, pp. 45–60.

[77] Pinchon, P., 1989. "Three Dimensional Modelling of Combustion in a Prechamber Diesel Engine". SAE Technical Paper 890666.

[78] da Cruz, A. P., 2004. "Three Dimensional Modeling of Self-Ignition in HCCI and Conventional Diesel Engines". *Combustion Science and Technology,* ***176***(5-6), pp. 867–887.

[79] Chemkin-Pro 15131 Reaction Design: San Diego, 2013.

[80] Mehl, M., Pitz, W. J., Westbrook, C. K., and Curran, H. J., 2011. "Kinetic Modeling of Gasoline Surrogate Components and Mixtures under Engine Conditions". *Proceedings of the Combustion Institute,* ***33***(1), pp. 193–200.

[81] Jud, M., 2019. "Numerische Simulation der Zündung und und Verbrennung von mit Diesel pilotierten Erdgasstrahlen". PhD thesis, Chair of Thermodynamics, Technische Universität München.

[82] Tao, F., Reitz, R. D., and Foster, D. E., 2007. "Revisit of Diesel Reference Fuel (n-Heptane) Mechanism Applied to Multidimensional Diesel Ignition and Combustion Simulations". 17th International Multidimensional Engine Modeling User's Group Meeting at the SAE Congress.

[83] Rahimi, A., Fatehifar, E., and Saray, R. K., 2010. "Development of an Optimized Chemical Kinetic Mechanism for Homogeneous Charge Compression Ignition Combustion of a Fuel Blend of n-Heptane and Natural Gas using a Genetic Algorithm". *Proceedings of the Institution of Mechanical Engineers, Part D: Journal of Automobile Engineering,* ***224***(9), pp. 1141–1159.

[84] Schiffner, M., Grochowina, M., and Sattelmayer, T., 2017. "Development of a Numerical Model for Ignition Phenomena in a Micro Pilot Ignited Dual Fuel Engine With External Mixture Formation". In Proceedings of the ASME Internal Combustion Fall Technical Conference, American Society of Mechanical Engineers, pp. 1–11.

[85] Schiffner, M., Jud, M., and Sattelmayer, T., 2017. "Reaction Kinetics Analysis of Dual Fuel Internal Combustion Engines Based on Ignition Delay Times Using n- Heptane Methane Fuel Blends". In Proceedings of 8th European Combustion Meeting, European Combustion Institute, pp. 1005–1010.

[86] Li, G., Liang, J., Zhang, Z., Tian, L., Cai, Y., and Tian, L., 2015. "Experimental Investigation on Laminar Burning Velocities and Markstein Lengths of Premixed Methane–n-Heptane–Air Mixtures". *Energy & Fuels,* ***29***(7), pp. 4549–4556.

[87] Eder, L., 2018. "Development and Validation of 3D-CFD Injection and Combustion Models for Dual Fuel Combustion in Diesel Ignited Large Gas Engines". *Energies,* ***11***(3), p. 643.

[88] Dukowicz, J. K., 1980. "A Particle-Fluid Numerical Model for Liquid Sprays". *Journal of Computational Physics,* ***35***(2), pp. 229–253.

[89] Crowe, C. T., 1982. "Review-Numerical Models for Dilute Gas-Particle Flows". *Journal of Fluids Engineering,* ***104***(3), pp. 297–303.

[90] Reitz, R. D., 1987. "Modeling Atomization Processes in High-Pressure Vaporizing Sprays". *Atomisation and Spray Technology,* ***3***(4), pp. 309–337.

[91] AVL FIRE Spray Module-Version Manual 2018.2. AVL List: Graz, Austria.

[92] Dukowicz, J. K., 1979. Quasi-Steady Droplet Change in the Presence of Convection. Tech. rep., Informal Report Los Alamos Scientific Laboratory, Los Alamos Report, LA7997-MS.

[93] Bowman, C. T., 1991. *Fossil Fuel Combustion: A Source Book*. John Wiley & Sons, chapter: Chemistry of Gaseous Pollutant Formation and Destruction, pp. 215–260.

[94] Hanson, R. K., and Salimian, S., 1984. *Combustion Chemistry*. Springer Verlag, chapter: Survey of Rate Constants in the N/H/O System, pp. 361–421.

[95] Fenimore, C., 1971. "Formation of Nitric Oxide in Premixed Hydrocarbon Flames". *Symposium (International) on Combustion,* ***13***(1), pp. 373–380.

[96] Görner, K., 1991. *Technische Verbrennungssysteme, Grundlagen, Modellbildung, Simulation*. Springer Verlag Berlin Heidelberg.

[97] Meintjes, K., and Morgan, A., 1987. Element Variables and the Solution of Complex Chemical Equilibrium Problems. Tech. rep., GMR-5827, General Motors Research Laboratories.

[98] Landenfeld, T., Sadiki, A., and Janicka, J., 2002. "A turbulence-chemistry interaction model based on a multivariate presumed

beta-pdf method for turbulent flames". *Flow, Turbulence and Combustion volume,* ***68***, pp. 111–135.

[99] Liu, F., Guo, H., Smallwood, G. J., Gülder, Ö. L., and Matovic, M. "A Robust and Accurate Algorithm of the β-PDF Integration and its Application to Turbulent Methane-Air Diffusion Combustion in a Gas Turbine Combustor Simulator". *International Journal of Thermal Sciences,* ***41***(8), pp. 763–772.

[100] Boust, B., Sotton, J., Labuda, S., and Bellenoue, M., 2007. "A Thermal Formulation for Single-Wall Quenching of Transient Laminar Flames". *Combustion and Flame,* ***149***(3), pp. 286–294.

[101] Labuda, S., Karrer, M., Sotton, J., and Bellenoue, M., 2011. "Experimental Study of Single-Wall Flame Quenching at High Pressures". *Combustion Science and Technology,* ***183***(5), pp. 409–426.

[102] Sotton, J., Boust, B., Labuda, S. A., and Bellenoue, M., 2005. "Head-On Quenching of Transient Laminar Flame: Heat Flux and Quenching Distance Measurements". *Combustion Science and Technology,* ***177***(7), pp. 1305–1322.

[103] Vosen, S., Greif, R., and Westbrook, C., 1985. "Unsteady Heat Transfer during Laminar Flame Quenching". *Symposium (International) on Combustion,* ***20***(1), pp. 75–83.

[104] Lu, J., Ezekoye, O., Greif, R., and Sawyer, R., 1991. "Unsteady Heat Transfer During Side Wall Quenching of a Laminar Flame". *Symposium (International) on Combustion,* ***23***(1), pp. 441–446.

[105] Min, K., Cheng, W. K., and Heywood, J. B., 1994. "The Effects of Crevices on the Engine-Out Hydrocarbon Emissions in SI Engines". SAE Technical Paper 940306.

[106] Maas, U., and Pope, S., 1992. "Implementation of Simplified Chemical Kinetics Based on Low-Dimensional Manifolds". *Proceedings of the Combustion Institute,* ***24***(1), pp. 103–112.

[107] Gicquel, O., Darabiha, N., and Thévenin, D., 2000. "Liminar Premixed Hydrogen/Air Counterflow Flame Simulations using Flame Prolongation of ILDM with Differential Diffusion". *Proceedings of the Combustion Institute,* ***28***(2), pp. 1901–1908.

[108] Dulbecco, A., 2010. "Modeling of Diesel HCCI Combustion and its Impact on Pollutant Emissions Applied to Global Engine System Simulation". PhD thesis, Institut National Polytechnique de Toulouse.